TABLE OF CONTENTS

LIST OF FIGURES

Chapter 1

Chapter 2

Chapter 3

Chapter 4

LIST OF TABLES

Chapter 1

Chapter 2

Chapter 3

Chapter 4

CHAPTER 1 DEFINITION OF THE PROBLEM

1.1 INTRODUCTION

Nowadays, approximate 40% of Aluminium products are flat rolled products, in which about 90% are produced by the direct chill (DC) casting. The 1xxx and 5xxx-series aluminium alloys are two major non-heat-treatable (NHT) alloy groups used in 50% of all the flat rolled Al products[1]. When these products are used in the fabrication of products that demand high quality surface finishing such as lithographic sheets and plates, architectural panels, wine cans and so on, the Al sheets require high quality surface and the DC cast ingots require microstructure homogeneous[1, 2].

In the industry DC (direct-chill) casting of 1xxx and 5xxx-series aluminium ingots(Table 1.1), there often exist a macro defect in the ingots called Fir-tree Zones (FTZs), which can cause serious surface defect on the rolling sheets.

Table 1.1 Chemical composition of 1xxx and 5xxx Al alloys[1]

Alloy	**Element (wt %)**							
	Fe max	**Si max**	**Cu max**	**Mn max**	**Mg**	**Cr max**	**Zn max**	**Al min**
AA1050	0.4	0.25	0.05	0.05	< 0.05	-	0.05	99.50
AA1100	*	*	0.2	0.05	-	-	0.1	99.00
AA5005	0.7	0.3	0.2	0.2	0.5-1.1	0.1	0.25	rem

* 0.95 (Si+Fe)

In the past decades, although a lot of effort has been put in the aluminium industry to eliminate the FTZ defect, success is only limited.

1.1.1 DC casting AA5657 alloy

According to the wrought aluminium alloys designation system, the alloy of series that containing magnesium as the major alloy element are designate as 5xxx. As it is known, the addition of magnesium can markedly increase the strength of aluminum without decreasing the ductility, the corrosion resistance and weld ability are also good[3]. AA5657 alloy is one of the important members of 5xxx series. This alloy has application in many fields, such as packing, electricity, architectural, printing, and so on. Such application of AA5657 alloy requires high surface qualities Al sheets[8].

In AA5657 alloy ingots, the elements Si and Fe are the most common impurities appear. When compared Si with Fe, Si has higher solubility in molten aluminum and during solidification, which can reach 1.6%. Lower levels of Si are therefore easily dissolved at all molten stages of production and would be rejected into the liquid between dendrite arms during solidification process[4]. But the solubility of iron in the solid state is very low (~0.05 wt %) and therefore, most of the iron present in aluminum over this amount appears as an intermetallic second phase in combination with aluminum and often other elements[5,6].

A sketch of the DC semi-continuous casting process is shown in Figure 1.1. At beginning, the starting block is positioned inside the mold and the liquid metal is poured into the open mold from the top. A solidified shell is formed above the starting block and along the mold wall (primary cooling). As soon as the solidified shell (about 10 mm in thickness) is strong enough to hold the molten metal inside, the starting block is lowered. As the ingot emerges from the bottom of the mold, the cooling water impinges directly on the casting surface (Secondary cooling). The maximum heat extraction and main part of the solidification of the ingot occurs due to the secondary cooling, and this is why it is called DC casting. After some distance, e.g., 1 m for a commercial-size sheet ingot, a nearly steady-state regime (the stationary period) is established for the thermal field.

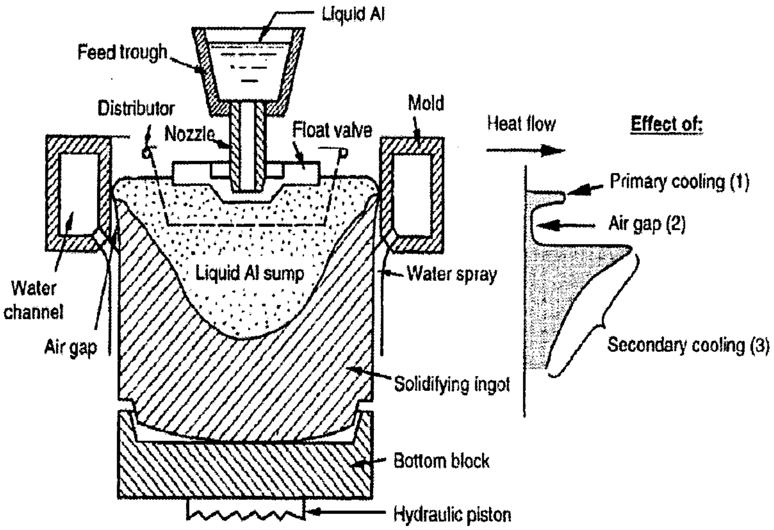

Figure 1.1: schematic illustration of a vertical DC caster and heat extraction mode[7].

During DC-casting of aluminium alloy ingots, the Al liquid is first cooled and solidified by the heat conduction between the walls of water-cooled mold, due to a high heat transfer coefficient[7]. It forms the shell, which takes the shape of the mold and acquires sufficient strength to hold Al liquid sump in the center.

In the air gap region, the heat extraction caused by the ingot surface radiation is reduced due to lower heat transfer coefficient of air, which leads to shell reheating, or even re-melting of the shell from inside.

The out skin formed during rapid primary cooling and the inner layer formed in the air gap region together is often called shell zone[8]. Following the shell zone is a zone subjected to secondary cooling due to the directly impingement of water spray[9]. The cooling rate becomes very high, because of the very high heat transfer coefficients. Thus, most of the heat extracted during this process by convection[7]. The cooling rates decreases gradually towards the ingot center due to longer diffusion paths.

Table 1.2 Local heat transfer coefficients and cooling rates in DC-casting[7]

Region	Cooling Stage	h(W/m^{2}K)	Cooling rate
Water cooled Al mold	Primary cooling	2,000-5,500	High
Air-gap	Shell reheating	200-500	Low
Direct chill(water spray)	Secondary cooling	8,000-70,000	High

During the solidification process of DC casting Al ingots, the first phase solidified is the primary α-Al, while Fe is eject into the remaining interdendritic Al liquid due to the low solubility, when Fe reaches the eutectic composition at 1.8wt% and 655℃, an equilibrium intermetallic phase Al_3Fe forms under equilibrium cooling rates between the dendrite arms of α-Al matrix[5]. Under higher cooling rates, several nonequilibrium phases form, such as Al_mFe, Al_6Fe, α-AlFeSi and so on. In a DC casting Al ingot from the casting surface to the ingot center, the cooling rates varies from 20℃ to ≤0.5℃[5]. Because of the existence of the cooling rates difference in varies location of the DC casting ingot, different eutectic Fe intermetallic phases form preferentially in different position of the ingot, and causes microstructure inhomogeneities, which can be easily observed by naked eyes after etching and/or anodizing. The FTZs caused in DC casting process can be highlight by the chemical etching and anodizing treatment, and can cause streaks and bands on the final rolling products. For the alloy ingots as AA5657 that are sold especial for their ability to develop and exhibit a pleasing surface, often undergo processes as etching and anodizing treatment, should be free from the defect of FTZs.

Nowadays, DC casting ingots with big size like 600mm X 2000mm in cross-section and more than 7000mm in length are commonly produced in Al industry. Such a shape makes the FTZs easier to appear. In industry practice, in order to eliminate the effect of FTZs, scalp the out skin of a ingot is carried out, the scalping depth normally is between 10mm and 20mm, but sometimes this depth is not enough to totally remove the FTZs, the remaining zones can be elongated into light and dark longitudinal streaks and bands in the rolling process, which greatly decrease the quality of the products[10, 11]. The appearance of the zones and the streaks is shown in Figure 1.2 and Figure 1.3.

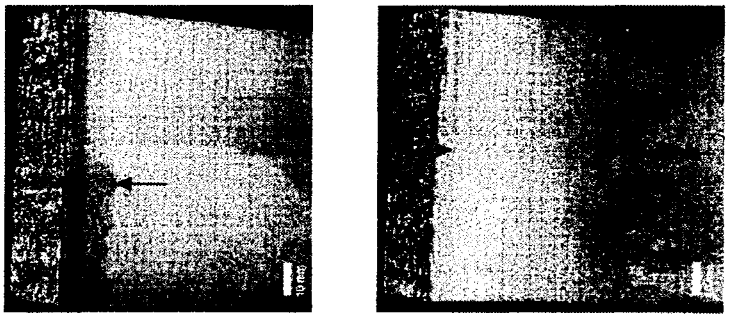

(a) (b)

Figure 1.2: Longitudinal section of 2 ingots showing the fir-tree zones of different sizes in 1xxx series Al alloy. (a) Small FTZ, Fe/Si=3.4; (b) Large FTZ, Fe/Si=1. The FTZ locations are shown between 2 arrows. Alloy was etched in 10% NaOH at 70℃ for 20mins[11].

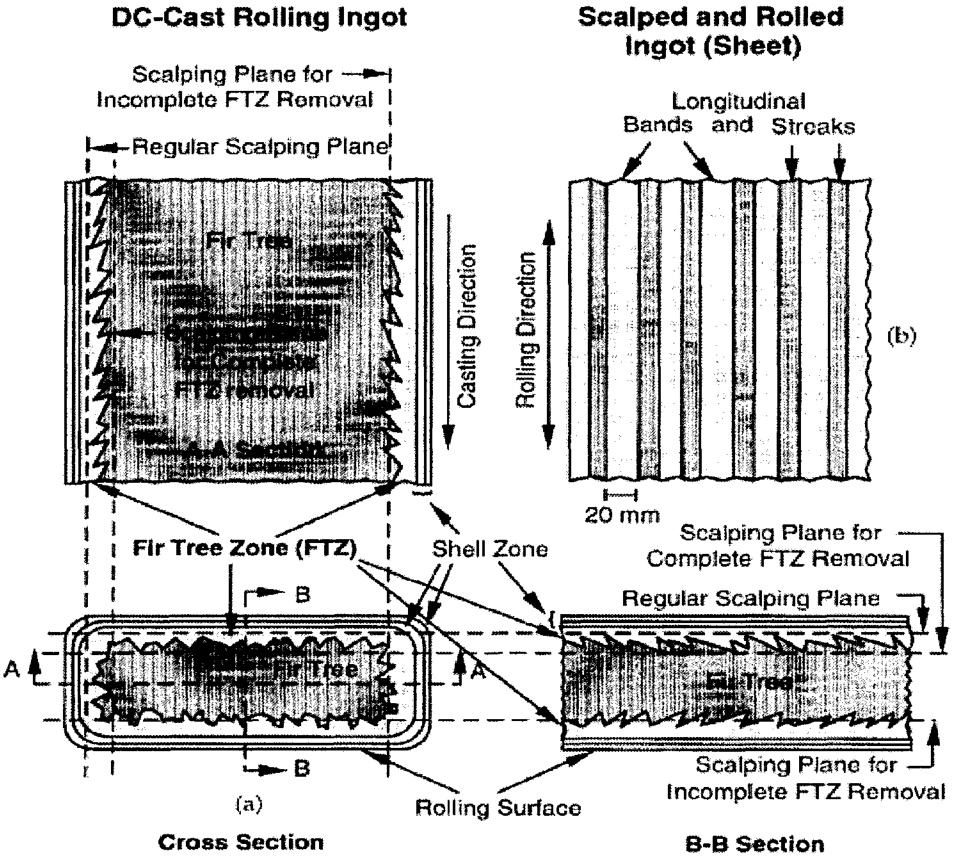

Figure 1.3: Schematic of different zones forming in DC-cast rolling ingots and the zebra structure (bands and steaks) forming in scalped and rolled ingot[10].

1.2 Objective and methodology of present work

For the past several decades, a lot of research has been carried out to study the effect of DC casting ingot structure. Until now, it is widely accepted that the solidification process and resultant cast microstructure plays an important role in the product quality. It is quite clear that the formation of Fir-tree zone is a function of the cooling rates, Fe/Si ratio, grain refiner, and small quantities of trace elements[12,13,14]. But it is still not clear about the effect of trace elements V and Ni on Fe intermetallic phases and Fir-tree zones. Moreover, nowadays, with decreasing quality of aluminium smelting raw material supply (coke, alumina ...) and alloying elements, the levels of trace elements present in the primary metal will increase[15]. The impact of this increase on the aluminium transformation processes and the final products is uncertain. Thus, there is a need to better understand these impacts, which will allow identifying ways to mitigate the negative impacts, to use the positive impacts for product/process improvement.

The methods used in this research are as follows:

1. DC casting simulator: A DC casting simulator apparatus is used in the laboratory to cast Al alloy ingots, which provides similar solidification conditions in the sub-surface regions as industry DC ingots.

2. Metallographic Studies: The ingot microstructure and Fe intermetallic phase morphologies were studied using Optical microscope, deep-etching and SEM techniques. SEM-EDS technique was also used to give an analysis of the elements containing in the Fe intermetallic phases.

3. Electron Backscattered Diffraction (EBSD): HKL Nordlys EBSD detector and Channel 5 system software are used for identification of intermetallic particles.

4. CLEMEX Image Analyzer: By using this technique, a quantitative analysis of the Fe intermetallic particles was performed.

CHAPTER 2 REVIEW OF THE LITERATURE

Until now, most of the researches on Fir-tree Zones and Fe intermetallic phases were carried out in 1xxx-series. It is widely accepted that the formation of FTZs is caused by the Fe intermetallic phases formation in the Al ingots. In this chapter, a summary of previous finding is given firstly, after that a detailed review of existing literatures is presented.

2.1 Findings found in previous researches

It is well-known that the elimination of fir-tree zones in aluminium ingots can automatically eliminate the streaks and bands on aluminium sheets. Hence, in order to eliminate the fir tree-zones, a lot of studies were carried out by investigating the effect of DC cast process parameters, Si and Fe/Si ratio, the use of grain refiners and existence of trace elements. The following are the findings[11, 12, 13, 14, 16]:

1) High cooling rates (e.g. $dT/dt > 10℃/s$) during secondary cooling in DC-casting promote AlmFe and FTZ formation.

2) High casting speeds promote Al_mFe and FTZs formation.

3) Si promotes AlmFe and FTZs formation and Fe/Si has an effect on the thickness of FTZs. The largest FTZs width occurs at a Fe/Si ratio of about 2, it was reported that higher Fe/Si ratio caused smaller FTZs.

4) Grain refiner addition and a higher B/Ti ratio promote AlmFe and FTZ formation.

5) Some trace elements were reported to have effects on the fir-tree zone, but this

is still controversial and uncertain.

2.2 FTZs and Fe intermetallic phases in DC cast Al alloys

As mentioned in chapter 1, in industrial DC casting of Aluminium, a wide range of solidification conditions exists. Thus, there form a number of Fe intermetallic phases in the ingot and cause the formation of FTZs. In DC casting of AA1xxx and AA5xxx sheet alloys, elements Fe and some Si usually present in the ingots. Depending on the chemistry composition and solidification conditions, the presence of elements Fe and Si can form a number of binary Al-Fe and ternary Al-Fe-Si intermetallic phases while casting 1xxx alloys[4]. When the solidification is in equilibrium conditions (dT/dt < 0.015℃/s), the part of iron that excess its solubility limit will form a eutectic α-AlFeSi and an intermetallic phase Al_3Fe (often designated as $Al_{13}Fe_4$). But in the industry practice of Direct-Chill casting aluminium alloys, the ingot surface usually has higher cooling rate due to its direct contact with the mould of cooling water, so we should consider the difference between cooling rates variation in the casting ingot (dT/dt). Celil A. Aliravci[5] found at cooling rates decreasing from ~20℃ near the surface to ≤ 1℃ in the ingot center can cause the formation of metastable intermetallic phases besides the stable phase Al_3Fe, such as Al_6Fe, Al_mFe and so on. These phases form preferentially under varies cooling rates in different location of DC cast ingots.

On sectioning and surface treatment of an ingot, the areas of different phase content have different responses to a given etchant, the surface appears alternate dark and light etching zones, which is often referred to as “fir-tree” zones. The fir-tree zones are mainly caused by the Fe intermetallic phases transition microscopically, it is a macro-defect in the sub-surface regions in DC cast ingots. In the past, the fir-tree zone was often described as transitional process from metastable phase Al_6Fe to stable phase Al_3Fe. But more recently, people have found that the fir-tree zones is a phenomena which involves transitions of different intermetallic phases at the same time, such as α-AlFeSi to Al_3Fe, α-AlFeSi toAl_6Fe, Al_mFe to Al_6Fe. Thus, in DC casting Al ingots, a mixture of iron intermetallic phases can be observed on both sides of the fir-tree zones and the phases vary across the zones.

H. Wenstengen observed five distinct regions across the thickness of a DC casting Al ingot using caustic soda etching method[8] (Figure 2.1).

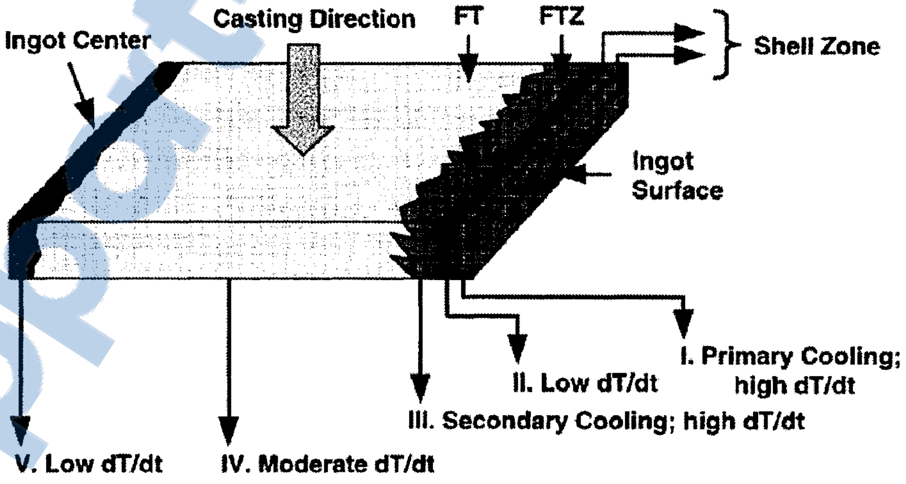

Figure 2.1: Schematic illustration of various zones across the ingot thickness. The slice is from a 1xxx-series Al ingot, and etched in 10% NaOH at 70℃ for 5~20 mins[8].

H. Wenstengen identified five different Fe intermetallic phases (Table 2.1) in the regions. The phases form due to different local cooling rates in each region[18].

According to Figure 2.1, the following observations were made:

Table 2.1 Fe-containing phases identified in different regions in a 1xxx-series Al ingot[8]

Phase proportion	Phases Forming in regions I to V				
	V	IV	III	II	I
Major	Al_3Fe	Al_6Fe	Al_mFe	Al_3Fe	Al_mFe
Intermedia	Al_6Fe	Al_xFe			
Minor		Al_3Fe			
Trace	α_c-AlFeSi*	α_c-AlFeSi*	α_c-AlFeSi*	α_c-AlFeSi*	α_c-AlFeSi*

* Metastable cubic *α* forms instead of stable hexagonal *α*.

1. Primary cooling region (I): This region is always called the shell zone. AlmFe phase forms at the boundaries of the dendrite *α*-Al primary phase due to the high cooling rates (dT/dt > 20 ℃/s). The thickness of this region varies between 1 mm to 3 mm.

2. Air-gap region (II): A stable Al_3Fe phase forms in this region due to the low cooling rates caused by the reheating and partially remelting of the ingot shell from inside. The thickness of this region varies between 5 mm and 7 mm.

3. Second cooling region (III): Mainly the metastable Al_mFe forms in this region due to high cooling rates (dT/dt ~10℃/s) caused by direct water impingement.

4. Region IV: The cooling rates are moderate and slowly decrease to the ingot center. The metastable phases Al_6Fe, Al_xFe and stable phase Al_3Fe form.

5. Region V : Mainly Al_3Fe and small amount of Al_6Fe form in this region due to low cooling rates (dT/dt < 1 ℃/s).

The so called FT-FTZ which is shown in Figure 2.1 forms mostly after the Shell Zone. After casting an ingot, common practice is to scalp the ingot so that the fir-tree zones can be removed, which is time consuming and uneconomic. Also, it is desirable to cast as quickly as possible. Thus, it is of great importance to control the formation of Al-Fe and Al-Fe-Si phases in the cast ingots in order to eliminate the fir-tree zone defects.

Iron-containing phases in aluminium alloys can be separated into either eutectic or peritectic reaction, the identification of the phases in metallographic section has many ways. In modern studies, the structure of phases is frequently carried out under scanning electron microscope (SEM) in backscattered electrons or secondary electrons mode. The backscattered electrons mode permits one to obtain the maximum phase contrast and to distinguish most of the phases present by their brightness. This facilitates the identification of the iron-containing phases, which are bright by contrast the aluminium matrix because the atom number of iron is bigger than that of aluminum[17].

As the cooling rate decrease from the out region to the ingot interior, that is from outer (>8 k/s) to inner (2-6 k/s), different iron-containing phases are formed. The transition is from phases α-AlFeSi + Al_mFe to α + Al_xFe + Al_6Fe, and then to the equilibrium α-AlFeSi + Al_3Fe[17].

Until now, it is commonly accepted that the occurrence of the metastable intermetallic phase Al_mFe is the main cause of fir-tree zone in DC cast 1xxx-series ingots, and it has been determined that the fir-tree zone was caused by the following two reason[18]:

1) Because the existence of different local cooling rates, different metastable phases form in the two adjoining zones separated by the jagged FTZ-FT interface.

2) Different phases exhibits different etching characteristics upon etching or/and anodizing. It is the etching/anodizing responses difference between the phases that makes fir-tree zone visible in ingots and structural streaks visible in sheets.

2.2.1 Iron intermetallic phases in the Al-Fe-Si system

Figure 2.2 shows the Al rich corner of the equilibrium Al-Fe phases diagram.

Figure 2.3 shows Liquidus projection near the Al-corner in the Al-Fe-Si phase diagram.

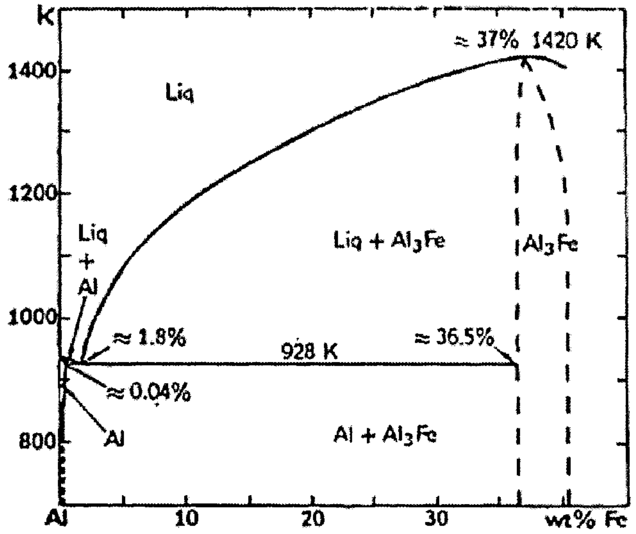

Figure 2.2: The Al rich corner of the equilibrium Al-Fe phases diagram.

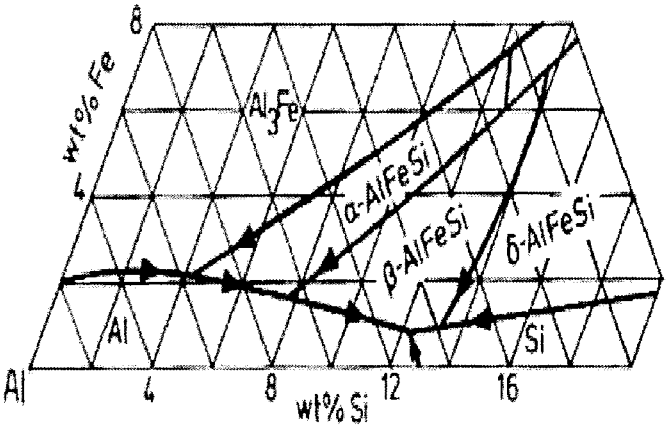

Figure 2.3: Liquidus projection near the Al-corner in the Al-Fe-Si phase diagram.

As shown in the figures above, during the solidification of Al-Fe-Si alloys, the primary α-Al is the first phase solidified. Because of low solubility of Fe in solid Al, most of Fe enriched continuously in the remaining interdendritic liquid, as it reaches the eutectic composition at 1.8wt% and 655℃, the stable eutectic intermetallic phase Al_3Fe forms between α-Al phase at equilibrium cooling rates.

It is known that the existing phase diagram can be used to estimate the iron-containing phases formed in equilibrium conditions. However, in real industrial production there exists conditions nonequilibrium, so some other metastable phases such as Al_xFe, Al_6Fe, Al_mFe, α-AlFeSi, β-phase may form respectively. Thus, the phase diagrams are not useful to predict the metastable phases formation.

Table 2.2: Solidification reactions in the Al-Fe-Si system[5, 19, 20]

Reaction	Re. Temp. (℃)	Wt% Fe	Wt% Si
Binary equilibrium Liquid → Al + Al_3Fe	655	1.8	---
Binary nonquilibrium			
Liquid → Al + Al_xFe	---	---	---
Liquid →Al + Al_6Fe	---	---	---
Liquid →Al + Al_mFe	---	---	---
Ternary equilibrium			
liquid+Al_3Fe→Al + Al_8Fe_2Si(α-AlFeSi)	620-638	---	---
liquid+ Al_8Fe_2Si→Al + Al_5FeSi(β- AlFeSi)	611-615	---	---
Liquid →Al+Si+ Al_5FeSi(β- AlFeSi)	576-577	---	---

*α-AlFeSi and β-AlFeSi were also reported as results of peritectic reactions[21].

For the identification of different types of Fe intermetallic phases, early work was focused on the phase morphology via optical microscopy, two important Fe phases chinese script α-AlFeSi and plate-shaped β- AlFeSi were identified[22,23]. When mention the phase morphology of Al_6Fe, Al_mFe, α-AlFeSi, Al_3Fe and β-AlFeSi, two types of phases can be identified by their morphologies[24], Al_3Fe and β-AlFeSi can be grouped in the first group for their plate-shaped and their crystals exhibit a faced growth. Al_6Fe, Al_mFe, α-AlFeSi can be grouped in the second group for their shape of interdendritic channels and their complex-shaped crystals growth. The morphology of the Fe intermetallic particles cannot be established by conventional morphology in 2-D. In addition, the Fe phases can adopt morphology of great difference in different series of Al alloys[25]. In such a situation, identification of Fe phases based on morphology can be misleading.

In the recent years, in addition to identify Fe intermetallic phases based on their morphologies, Energy Dispersive Spectra (EDS) and Electron Backscattered Diffraction (EBSD) has been employed to study the chemical component and crystallography of the Fe phases[26]. As mentioned, phase identification based on the morphology is inaccurate. Also, EDS is not sufficient to determine the stoichiometry of a certain phase, because the intermetallic particles are sometimes adopt relatively small size, which may cause the EDS signal obtained from the matrix. Thus, the main purpose of getting EDS spectra is to reveal which elements are present rather than to give a quantitative analysis of the particle composition. In M.V. Kral et al's work[26], EDS and EBSD technique were used as the principal methods to identify the Fe intermetallic particles accurately.

Known in the low Si content Al alloys, the β-phase cannot form under DC-casting conditions, so only binary phases Al_3Fe, Al_xFe, Al_6Fe, Al_mFe and ternary phase α-AlFeSi (Al_8Fe_2Si) forms (Figure 2.4)[27].

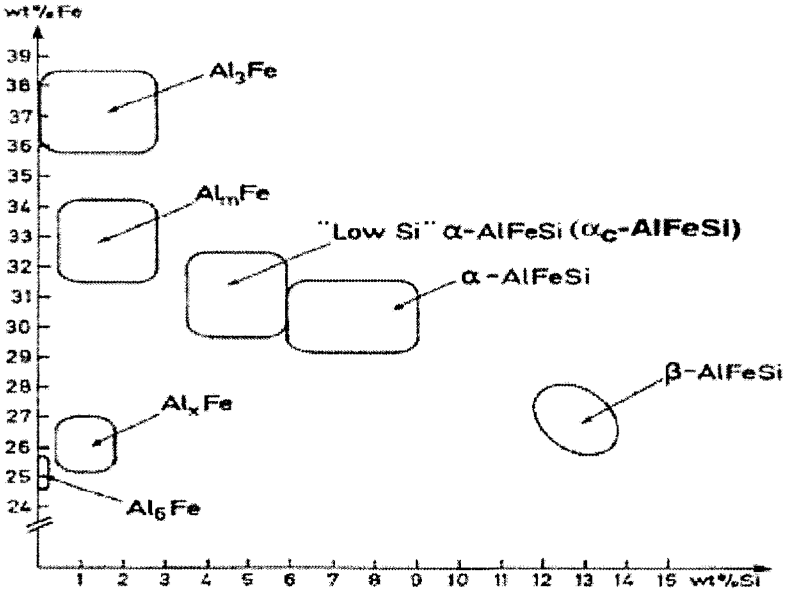

Figure 2.4: Composition of the intermetallic particles observed in DC-cast alloys[27].

A review of the studies that have been carried out on the most commonly occurring Fe intermetallic phases morphology and their crystallography are present in the following section.

2.2.1.1 Al_3Fe phase

The Al_3Fe phase, which is often denoted as $Al_{13}Fe_4$, it is revealed by X.-Grant Chen and other researchers that the typical morphology of Al_3Fe is plate like[4]. It is C-centered monoclinic in space group C2/m. The lattice parameters are: a=1.5489 nm, b=0.808 nm, c=1.2476 nm and β= 107°43′[28].

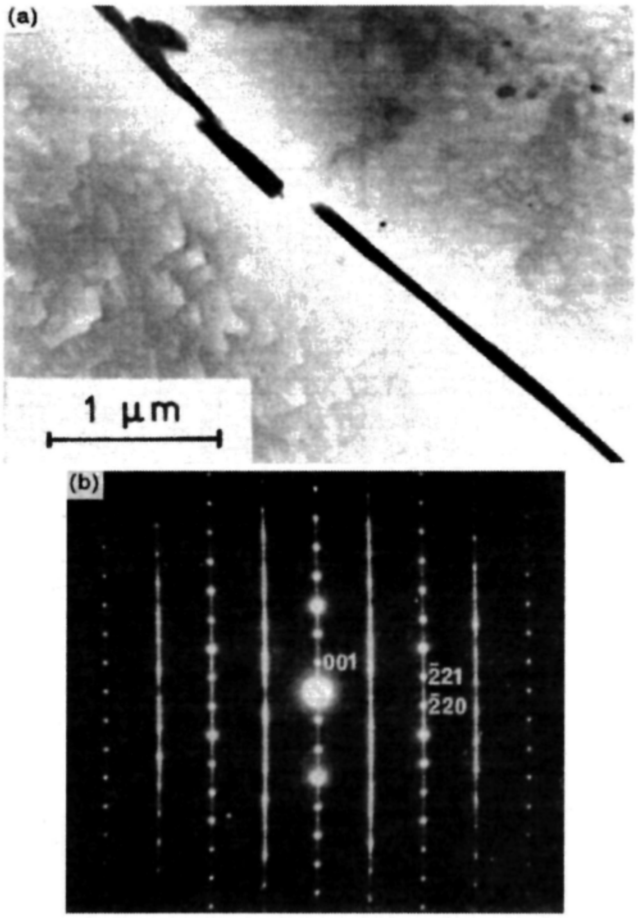

Figure 2.5: (a) Fe_4Al_{13} at grain boundaries in cast ingot 29; (b) Typical [110] diffraction pattern of a faulted Fe_4Al_{13} crystal [30].

2.2.1.2 Al_6Fe phase

Al_6Fe is often found in relative rapidly solidified region in Al alloys, it has morphology of flake with several short wings. For three-dimensional morphology after deep-etching, it shows a curved plate with a number of rod-like branches[4]. Al_6Fe is a common intermetallic phase in DC cast Al ingots. It is isomorphous with Al_6Mn, thus the Fe can be substituted freely by Mn in the Al_6Fe lattice and lower its free energy. This can raise the thermodynamic stability of the Al_6Fe in the Mn containing alloys[13,44].

The crystal has a C-centered orthorhombic structure, space group $Cmc2_1$. The lattice parameters are a=0.6492 nm, b=0.7437 nm, c=0.8788 nm[28]. Figure 2.6 shows a typical morphology of Al_6Fe in a TEM sample and its select area diffraction pattern:

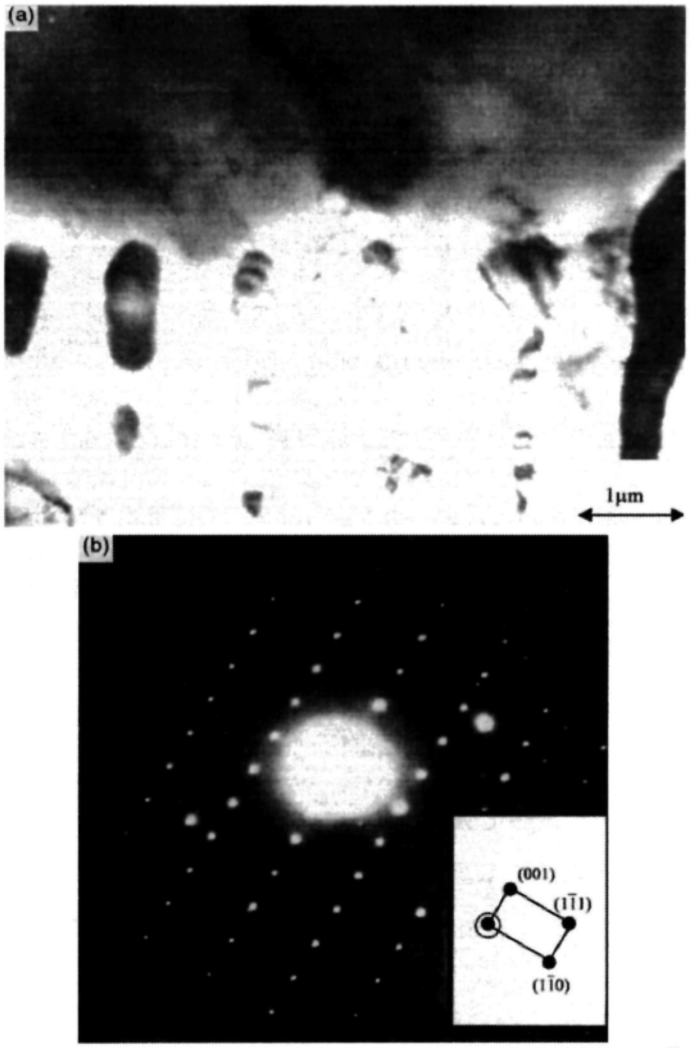

Figure 2.6: (a) Al_6Fe phases in a TEM sample; (b) SAD pattern in the (110) zones[31].

2.2.1.3 Al_mFe phase

Al_mFe phase forms at regions with the highest cooling rates in the DC-casting ingots. The morphology is mostly dendrite-like, while the morphology after deep-etching exhibits a fine feathery characteristic with many fibers growing in different orientations under SEM[4]. Till now, it was commonly accept that the occurrence of the Al_mFe metastable intermetallic phase is the main factor of fir-tree zones in DC cast 1xxx-series ingots[18]. Al_mFe phases have a body-centered tetragonal crystal structure, it has been reported by P. Skjerpe that the lattice parameters are: a=0.884 nm, c= 2.16 nm, space group I4/mmm[32].

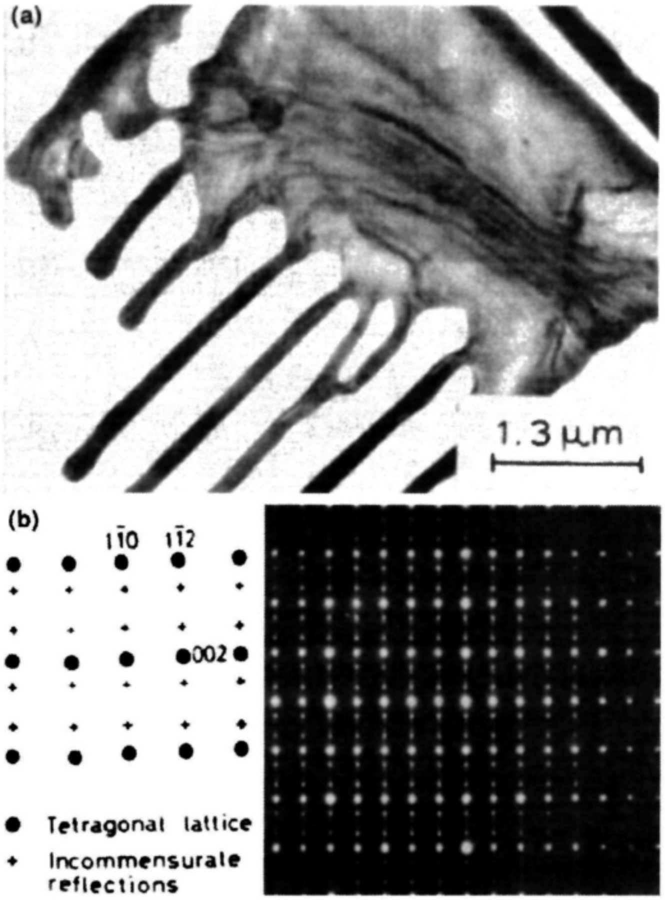

Figure 2.7: Al_mFe and corresponding [110] diffraction pattern[32].

2.2.1.4 Al_xFe phase

It has been reported that Al_xFe forms in rapid solidification Al alloys, but the cooling rate required is less than Al_6Fe[33]. According to Skjerpe, the crystal structure of this phase is similar to Al_6Fe, and he found the unit cell parameters are: a=0.6 nm, b=0.7 nm, c=0.47 nm[34].

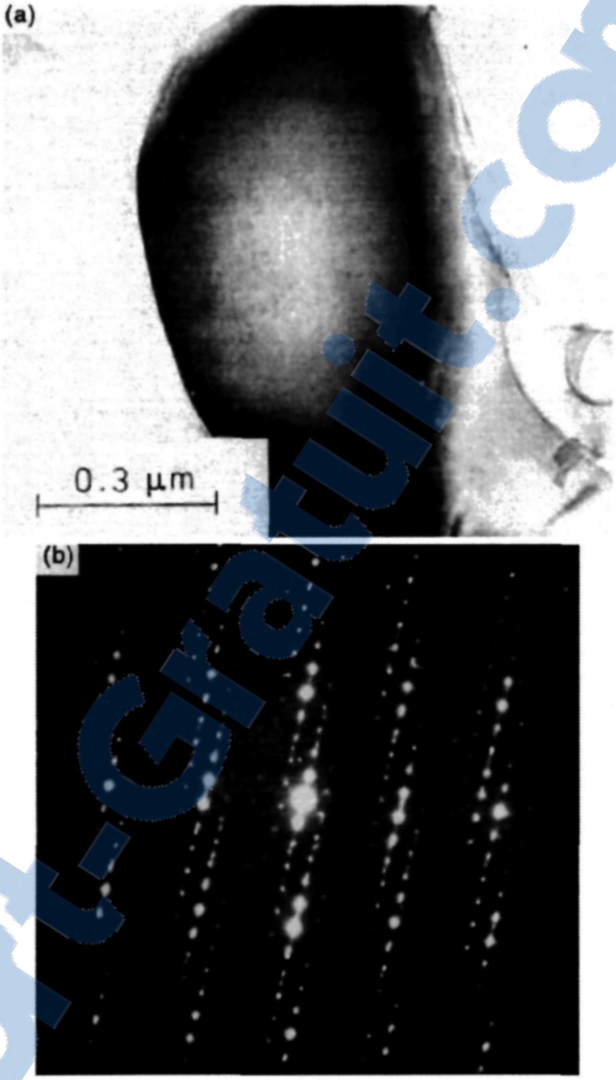

Figure 2.8: (a) Al_xFe and its diffraction pattern[34].

2.2.1.5 α-AlFeSi

The α-AlFeSi (sometimes write as Al_8Fe_2Si, Al_7Fe_2Si or $Al_{12}Fe_3Si$) appears a complicated dendrite form, and often described as Chinese script under optical microscope image. It can be distinguished easily from the binary Al-Fe intermetallics with its triangular edge on the front of each plate[4]. Some research identified α-AlFeSi as cubic and some identified as hexagonal[21, 35]. For the hexagonal structure α-AlFeS:

the space group is p6$_3$/mmc. The unit cell parameters are a = 1.24 nm, c =2.623 nm[28]. It was reported this phase appear at high cooling rates and low Fe and Si levels[33].

It is known in the literatures that relatively high cooling rates and additions of elements of V, Cr, Mn, Cu, Mo and W can promote a body-centered structure for the α_c-AlFeSi [15,33].

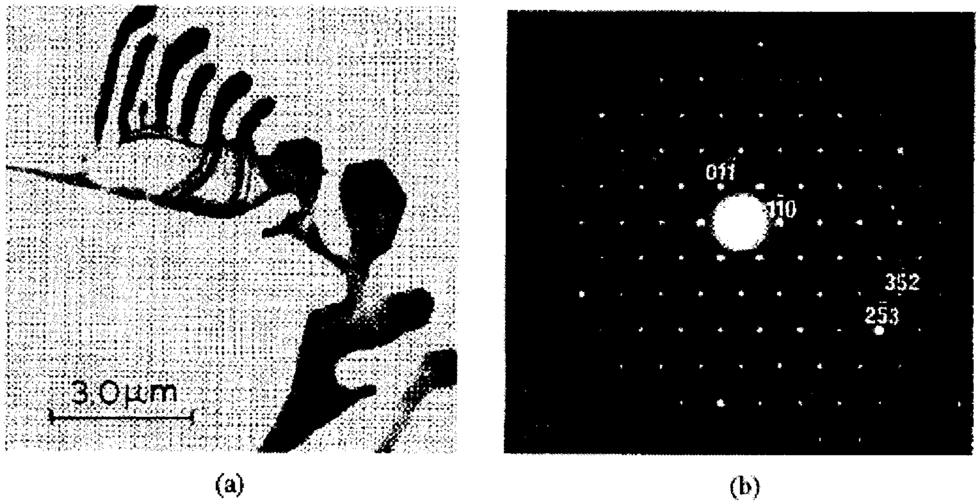

(a) (b)

Figure 2.9: (a) Extracted α_c-AlFeSi (Al8Fe2Si) (b) SAD pattern in the <111> zone [34].

2.2.1.6 β- AlFeSi

The β-AlFeSi (Al_5FeSi or $Al_9Fe_2Si_2$) forms as thin platelets and often observed as long thin needles, sometimes with curves. It has monoclinic structure[21]. The lattice parameters are: a = b = 0.612 nm, c = 4.15 nm, β= 91°.

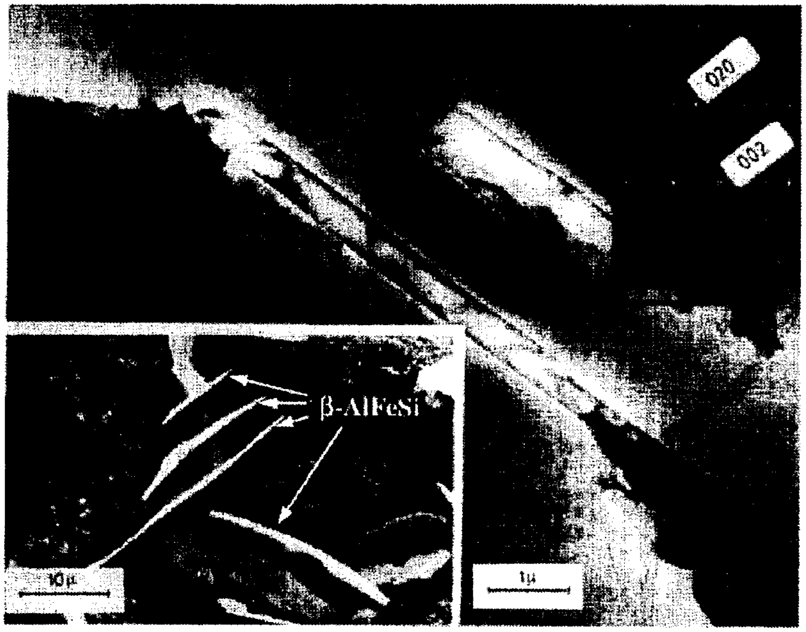

(a) (b)

Figure 2.10: β-AlFeSi intermetallic phase. (a) SEM micrograph of deep-etched sample; (b) TEM image with SAD pattern[36].

2.2.2 Factors that affect Fe phases selection in Al alloys

Different Iron phases in the aluminum alloys have varies effect to the alloy properties, so it is of great importance to have a good understanding of the factors under non-equilibrium solidification conditions that effect phase selection in Al alloys. Investigations into the intermetallic phase selection in dilute Al alloys have been ongoing for many years. Until now, it has been found that the formation of Fir-tree zones and corresponding Fe intermetallic phases is effected by the parameters such as the cooling rates, Fe/Si ratio, grain refiner, and small quantities of trace elements. A brief review of the parameters and its effects are described in the following sections:

2.2.2.1 Cooling rates

The cooling rates are a factor of great importance to the Fe intermetallic phases selection in Al alloy ingots. Till now, a lot of researches have been carried out to study the effect of cooling rates on the formation of Fe intermetallic phases. In B. Dutta and M. Rettenmayr's research[37], it was found that with the cooling rate increase from 0.04 K/s to 3.5 K/s, the fraction of eutectic content in the alloy increased, the phase types and phase morphology are also changed. Similarly, D. Panahi et al[38] found that the very high cooling rates limited the precipitation of binary Al–Fe compounds and favored the formation of the ternary phase.

According to Belov's findings[17], As the cooling rate decrease from the out region to the ingot interior, that is from outer (>8 k/s) to inner (2-6 k/s), different iron-containing phases are formed. The transition of phases is from Al_mFe to α-AlFeSi + Al_xFe + Al_6Fe, and then to the equilibrium α-AlFeSi + Al_3Fe. While PER SKJEPPE's[39] discover that at a cooling rate of 6 to 8 K/s, the dominating phases are α-AlFeSi and Al_mFe, while at a cooling rate of 1 K/s, the dominating phases are Al_3Fe and Al_xFe, Al_6Fe forms at cooling rates 1 to 10 K/s and Al_mFe forms at cooling rates exceeding 10 K/s.

In previous studies, a critical (minimum) cooling rate required for the Al_mFe phase formation was determined in some alloys. In AA1050 alloy (0.25wt% Fe, 0.13wt% Si, 0.03wt% Ti), the cooling rate is 8℃/s, as shown in Figure 2.11. In AA5005 alloy (0.43wt% Fe, 0.13wt% Si, 0.85wt% Mg, 0.03wt% Ti)[40], the cooling rate is 8.5℃/s.

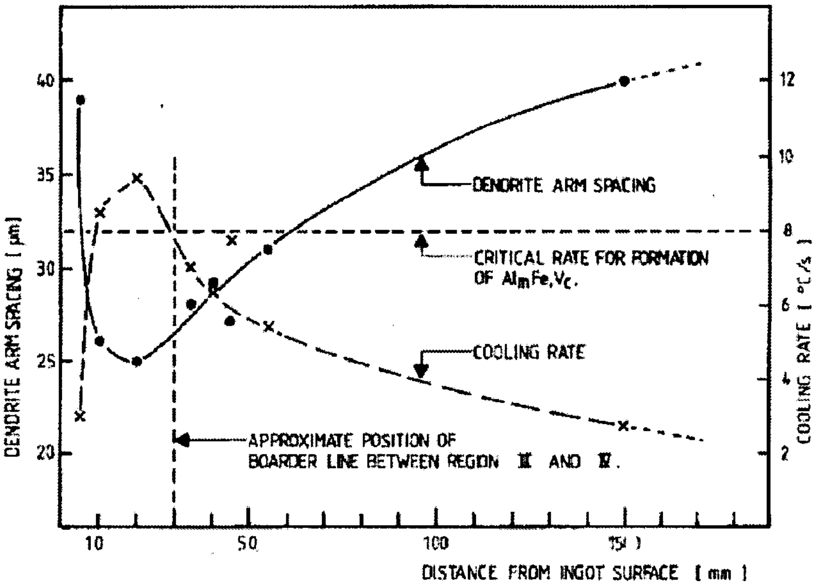

Figure 2.11: Cooing rate and corresponding secondary dendrite arm spacing as a function of distance from ingot surface, critical cooling rate for AlmFe is given[33].

In some literatures, the critical cooling rates for Al_3Fe, Al_6Fe and Al_mFe are also given, see Table 2.3.

Table 2.3: Critical cooling rates for the formation of some Fe intermetallic phases

Researcher	Coposition	Critical cooling rates (℃/s)		
		Al_3Fe	Al_6Fe	Al_mFe
H. Kosuge and I. Mizukami[41]	Al-0.6wt Fe-0.01wt% Si	$dT/dt < 2$	$2 < dT/dt < 20$	$dT/dt > 20$
Young et all[42]	Hypoeutectic Al-Fe alloy	$dT/dt < 0.9$	$3 < dT/dt < 11$	$dT/dt > 11$
Miki et all[43]	1xxx-series	$dT/dt < 1$	$1 < dT/dt < 10$	$dT/dt > 10$
Backerud[44]	Al-1wt% Fe	$dT/dt < 3.2$	$dT/dt \geqslant 3.2$	---

From the findings that has been made, we can find there is a similar point that under the higher cooling rates, form the more metastable phases.

2.2.2.2 Fe/Si ratio

There is no doubt that the impurities Fe and Si play an important role for the formation of Iron intermetallic phases[17, 45]. In addition, Fe/Si ratio also has effect on the Fe intermetallic phases selection. S. Brusethaug et all found that Fir-tree zones appear at Fe/Si of about 2, while the Fir-tree zone can be eliminate at Fe/Si ration of larger than 3 [16]. Furu et al found when the Fe/Si is of 1, the Fir-tree zones is much larger than that of 3.4 and 6.3 [11].

Table 2.4: Effect of Fe/Si ratio on FTZs width in Al-Fe-Si alloy ingots11

Cast No.	Fe (wt%)	Si (wt%)	Fe/Si ratio	FTZ Width (mm)
1	0.15	0.15	1	70
2	0.48	0.14	3.4	9
3	0.82	0.13	6.3	0

2.2.2.3 Grain refinement

The purpose of grain refinement is to produce a refined, equiaxed grain structure with modified second phase particle morphology through the thickness of the DC cast ingot. The most common grain refiner being used are 6%Ti, 3%Ti, 5%Ti-0.1%B, 5%Ti-1%B, and 5%Ti-0.2%B. All these are based on Al, and its compositions are in commercial use for a variety of applications and products.

In addition of grain refinement, experiments have shown that the morphology of the insoluble iron-rich phase can be influenced, not only by the grain refiner composition, but also by the manufacturing route used by different suppliers. This would indicate that the nucleation mechanism of the iron-rich particles is strongly influenced by the grain refinement process[46].

It was found by X.-G. Chen[12] that addition of AlTiB, AlTiC and AlB refiner promotes Al_mFe formation and enlarges the fir-tree zones. Moreover, he had an observation of direct nucleation of Al_mFe on TiB_2 and TiC particles which maybe the cause of promote Al_mFe [12]. In S.J. Magges et al's research[13], the addition of Ti-B grain refiner, which can introduce TiB_2 particles, caused cubic α phase to become the dominant intermetallic phase and eliminated a visible FTZ boundary in certain Fe/Si ratio. He gave the reason why the TiB_2 assisted the nucleation of Al_mFe, which is probably hexagonal TiB_2 promotes the nucleation of phases with higher symmetry, such as cubic α phase and tetragonal Al_mFe rather than those in lower symmetry, such as orthorhombic Al_6Fe and monoclinic Al_3Fe. M. W. Meredith and et al [14] found in their research that the addition of grain refiner to a dilute Al-Fe binary alloy can slightly change the phase balance, increasing the presence of Al_3Fe and decreasing Al_6Fe, while the dominant phase is always Al_6Fe. The addition of refiner radically changes the morphology of these phases as the classical rod-like appearance of Al_6Fe is replaced by the curved, plate-like intermetallic phases.

2.2.2.4 Trace elements effects

Some trace levels of elements, such as Cu, Mn, Zn, Ti, V, Ni and so on, often appear as impurities in the commercial Al alloy ingots. It has been reported by some researchers that such trace levels elements can have a strong effect on the phase selection and fir-tree zones characteristics in dilute Al-Fe-Si alloys[15], but this is still under controversial.

Table 2.5: Effect of trace elements on the formation of Fe intermetallic phases[12, 13, 47]

Element	Phase Promoted	Alloy	Method
Mg	No major effect	Al-0.41%Fe-0.11Si	DC simulator
Ti	No major effect		
Mn	Al_3Fe		
Cr	Al_mFe	AA5005	
V	Al_mFe	AA1050	
Ni	?	?	

Allen et al[48] found in their research that V impurity and Al-Ti-B grain refiner can affect the solidification behavior and play an important role in phase selection during industry DC casting processes, in addition to the effects of solidification rates and bulk Si content. Control of V and grain refiner content in industry Al alloys may therefore provide a means of influencing secondary phase content and ultimately material properties, without having to redesign the alloy composition or change the casting parameters.

S. Maggs et al[13] explained that the addition of trace elements can alter both the nucleation and growth kinetics of a certain phase and make it lose out to another phase. Impurities may be segregated to the growth front and produce solutal undercooling and hence suppress growth velocity. Conversely, impurities may promote twinning which in turn promote the growth of a faceted intermetallic as

Fe_4Al_{13} by providing a higher density of re-entrant edges and corners to which atoms can attach more easily[13].

In general, the effect of trace elements on the phase selection can be the following two reasons[13]:

1. Trace elements that are strongly partitioned to the interdendritic liquid during the final stages of solidification can affect solidification behavior, which cause a constitutional undercooling and makes the phase with higher nucleation temperature in the undercooling liquid easily nucleate and grow.
2. Trace elements may dissolve into the phase by substitute some fraction of the Fe atoms in the crystal structure. By altering the free energies and hence change the thermodynamic characteristics of the phases. For example, Mn and Cu can stabilize Al_6Fe by forming $Al_6(Fe,Cu)$ and $Al_6(Fe,Mn)$.

2.3 DC casting simulator techniques

In the industry practice, large DC cast Al ingots were cast, which is too expensive and impossible to carry out in the laboratory. Thus, in order to reproduce the cooling rate near the casting surface of industry DC cast Al ingot, some lab-scale researches have been carried out in DC casting simulators[12, 13]. In this method, the melt Al liquid is poured into a cylindrical insulating mold with removable chill plate. initially (about 20 seconds) the cooling rate is slow due to poor contact with the mold, later fast when the water impinge directly on the bottom surface of the ingot, and then the cooling rates decrease due to the increasing conduction path. Thus, long cylindrical alloy rod samples directionally solidified by chilling from the bottom.

During the solidification process, the growth occurs parallel and opposite to the heat flow direction, the control of sample solidification conditions can be carried out by monitoring the local cooling rates got from the thermal couples inserted into the insulating mold[12].

In the DC simulator casting Al ingots, although it is difficult to obtain a microstructure exactly the same as industry DC casting ingot, it can still be viewed that a range of cooling conditions are along the height of an ingot, which cause Fe intermetallic phases transition from the chill end to the top of an ingot.

When compare the DC simulator technique that was used in the present research with the Bridgeman furnace, we can clearly found that the DC simulator is easier to build and more economic used in the lab.

2.4 EBSD technique

The Electron Backscatter Diffraction (EBSD) is based on diffraction technology, which is valuable when the chemical inspection is inaccurate, the phase is non-equilibrium or the phase can formed in different crystallographic systems[49]. EBSD can be used to identify the crystal structure of a phase and to evaluate the crystallographic orientation.

EBSD obtains crystallographic information from tilted polished samples in a scanning electron microscope (SEM). The electron beam strikes the sample and the electrons are elastically scatter beneath the surface. Electrons diffracted according to

Bragg's law form a pattern on a fluorescent screen. Each lattice plane is represented in the diffraction pattern by a Kikuchi bands[50] (Figure 2.12). By comparing to theoretical data, the crystallographic system of the phase and orientation can be identified[51].

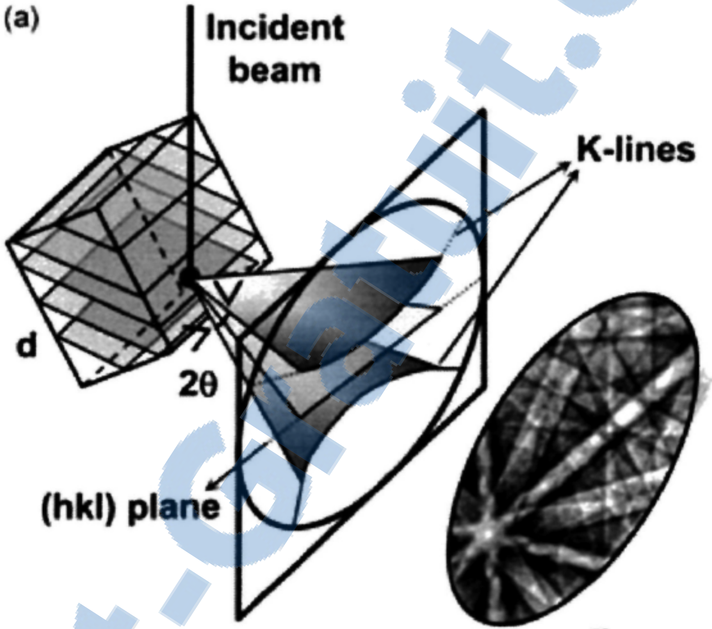

Figure 2.12: Formation of Kikuchi bands by back-scattered Electrons[52].

Chapter 3 EXPERIMENTAL PROCEDURES

3.1 Alloy preparation

In this study, both the commercial and experimental AA5657 alloys will be used, the chemical composition of the as-received commercial DC cast AA5657 ingot is shown in Table 3.1. The material was supplied in slice form that cut from the cross section of a commercial ingot from Alcan Laterriere plant, the dimension of the DC cast ingot is about 635 mm × 2030 mm in cross-section.

Table 3.1: Chemical Composition of the Industrial DC cast AA5657 ingot

Alloy	Element (wt%)											
	Si	Fe	V	Ni	Mg	Cu	Ti	Mn	Cr	Zn	B	**Al**
AA5657	0.04	0.07	0.0175	0.007	0.82	0.05	0.02	0.003	0.001	0.01	0.001	Bal.

The Al-5wt% V and Al-20% Ni master alloy are used to change the V and Ni levels in AA5657 base alloy.

3.2 Melting and Casting

The alloy ingots are melted in a crucible using an electrical resistance furnace. The melting temperature is kept at about 740 ± 5°C. At this temperature, the master alloy of V and Ni are added in the liquid to give different levels of V and Ni content. After V and Ni was total melt, the liquid was kept for 15 minutes for homogenate.

In the industry practice, Al alloy ingots always cast with a dimension as much as 635 mm x 2030 mm in cross-section and 7620 mm in length[9], which is impossible to duplicate in the lab. Thus, a DC casting simulator (Figure 3.1 and Figure 3.2) is build and used in the casting of AA5657 alloy ingots, which consists of mainly five parts: security cover, insulating mold, thermocouples, removable copper plate and water jet. This apparatus can produce a similar solidification condition on the sub-surface region of the ingots.

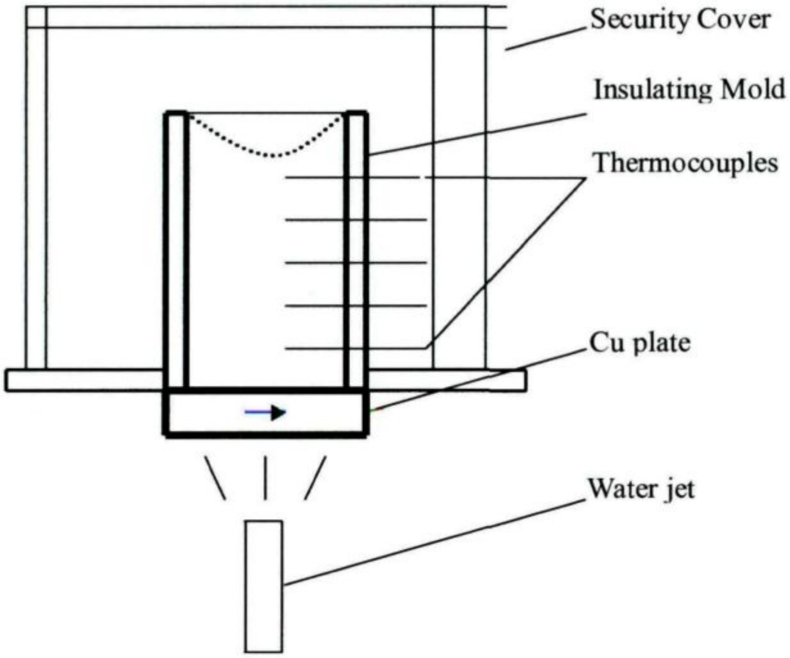

Figure 3.1: Schematic illustration of DC simulator apparatus

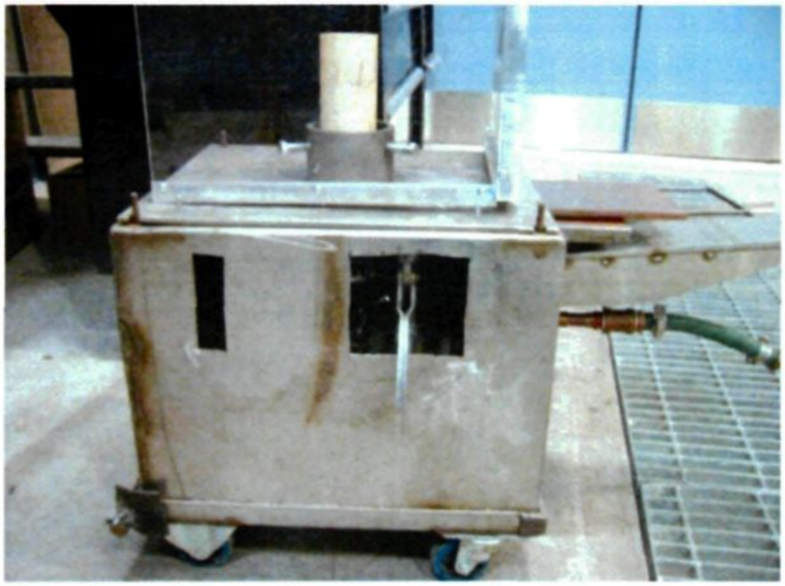

Figure 3.2: DC casting simulator used in present research.

Before casting, the insulating mold was heated to 500°C to remove moisture content. The AA5657 base alloy was melt in an electric furnace (Figure 3.3).

Figure 3.3: The electric furnace used in the lab.

The molten metal was poured into the mold fixed in the DC simulator. After about 20 seconds when the Al skin on the bottom was strong enough to hold the Al liquid, the Cu plate was pulled away to allow water to impinge directly onto the bottom surface of the ingot. During the casting process, the holding time is of great importance to the ingots microstructure, therefore impact on the position of the Fir-tree zone. There is no grain refiner addition during the casting process, the grain refiner remaining is coming from the DC cast ingot that was melted. The ingots cooling conditions during solidification process were measured by using five thermocouples insert into the center of the mold (Figure 3.1).

A Thermal Analysis test was carried out to study the solidification behavior of AA5657 alloy: poured the melting liquid into a thin wall steel crucible, two thermocouples were inserted into the center of the crucible (Figure 3.4), the Al liquid in the crucible was cooled slowly to room temperature. The cooling curved can be obtained from the computer connected to the thermocouples.

Figure 3.4: Cooling curve test apparatus used in the lab.

The ingots cast via DC simulator are with a dimension of 38 mm in diameter and 150 mm in length. In order to reduce the effect of cooling rats from the top and around, analysis samples are only taken from the center of the ingots within 120 mm from the chill end.

3.3 Sample analysis and Characterization

3.3.1 Chemical analysis

Alloy discs for chemical analysis were cast every time just after the sample ingots were cast. The work of chemical analysis was done in the lab of ARDC Rio Tinto Alcan. The alloys chemical composition results are given in Table 3.2:

Table 3.2: Chemical compositions of the DC simulator cast alloys (wt. %).

Alloys	Elements								
	V	Ni	Fe	Si	Mg	Cu	Mn	Ti	Al
*A01	**0.017**	**0.007**	0.071	0.045	0.82	0.047	0.003	0.018	Bal.
A02	**0.024**	**0.007**	0.075	0.049	0.82	0.049	0.003	0.019	Bal.
A03	**0.033**	**0.007**	0.072	0.064	0.81	0.056	0.003	0.02	Bal.
A04	**0.048**	**0.008**	0.078	0.049	0.83	0.049	0.003	0.02	Bal.
A05	**0.017**	**0.015**	0.07	0.045	0.81	0.047	0.003	0.021	Bal.
A06	**0.018**	**0.027**	0.072	0.044	0.79	0.051	0.003	0.021	Bal
A07	**0.018**	**0.039**	0.072	0.044	0.79	0.047	0.003	0.021	Bal.
A08	**0.017**	**0.057**	0.077	0.047	0.84	0.049	0.003	0.024	Bal.
A09	**0.026**	**0.024**	0.072	0.052	0.82	0.053	0.003	0.023	Bal.
A10	**0.038**	**0.025**	0.07	0.044	0.78	0.045	0.003	0.02	Bal.

* **A01** is base DC simulator cast AA5657 alloy.

3. 3.2 Optical Microscopy

After the ingots ware casted, the ingots was cut into two parts longitudinally. One half was used to examine the macrostructure as growth direction and Fir-tree zones. The other half was for microstructure observation.

For metallographic examination, the specimens were taken from different position of the ingots, mounted using epoxy resin and hardener mixture. The grinding was first carried out on silicon carbide papers on a rotating wheel automatically. The grit size is decreasing, (120, 220, 320, and 500). After grinding, diamond abrasive of 6μm and 1μm are used to eliminate the scratches on the sample surface. The final step

$0.05\mu m$ of polishing is done with a colloidal silica suspension.

In the present study, a system of CLEMEX image analysis with Nikon Eclipse Me 600 optical microscope (Figure 3.5) was used.

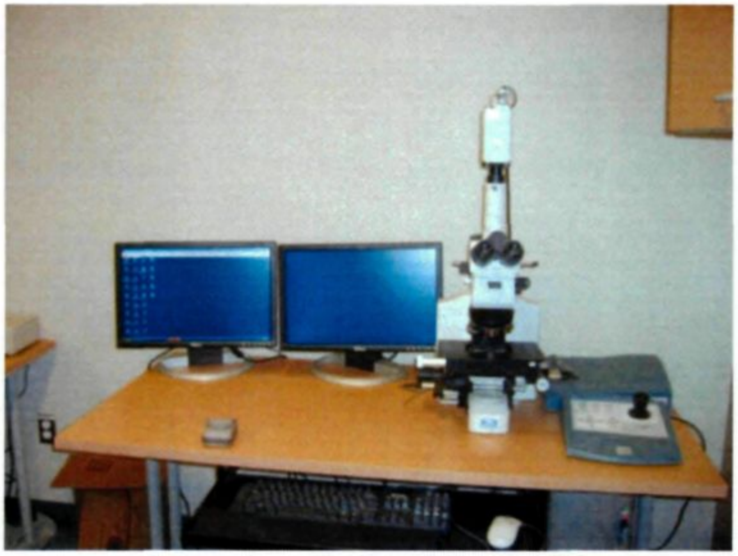

Figure 3.5: Clemex image analysis system with Nikon Eclipse Me 600 optical microscope.

3.3.3 Deep-etching of metallographic sample

In order to reveal the original morphology of Fe intermetallic particles, deep-etching and SEM technique are used. This technique can also be useful for the study of nucleation and growth behaviour of the Fe intermetallic phases. There were two different etchants used in the present study. One is 10% NaOH solution at 60~70℃, the other is 20% HCl at room temperature. The former is mainly used for AA5657 alloy ingots, while the latter was used in the study of 1xxx-series ingot. Put the surface of a finely grounded metallographic specimen in the etchant solution. The etching time varies from 5~10 minutes, after that the aluminum matrix on the surface layer of the specimen was dissolved while leave the intermetallic particles unaffected.

The etched sample is studied by using Scanning Electron Microscope (SEM) system under the secondary electron imaging mode. The SEM system is JEOM JSM-6480LV (Figure 3.6). The energy dispersive spectroscopy is also used to give a chemical composition analysis.

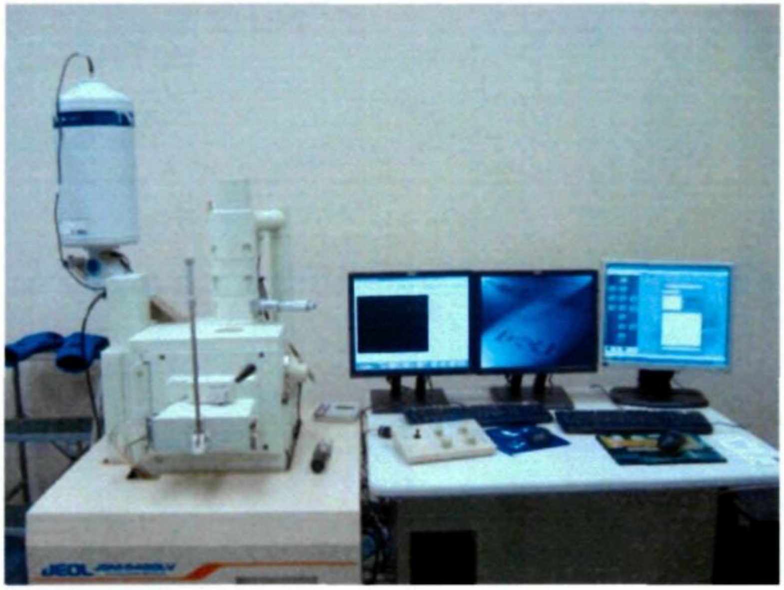

Figure 3.6: JEOM JSM-6480LV SEM system

3. 3.4 Electron Backscatter Diffraction (EBSD)

After the metallurgical study, EBSD technique was used to further the identification study of Fe intermetallic phases. In the present research, EBSD was used as the principal technique for the phase identification.

In order to identify the Fe intermetallic phases, EBSD technique was employed in present study. Using EBSD technique, the four types of Fe intermetallic phases appearing in the cast ingot were identified. It was found that the crystal structure of the intermetallic compound with a feathery like morphology was similar to Al_mFe; The crystal structure of the intermetallic phase with chinese-script morphology was agree well with Al_7Fe_2Si; The crystal structure of the intermetallic phase with curved plates morphology was agree well with Al_6Fe and the crystal structure of the intermetallic phase the needle like morphology can match well with Al_3Fe.

3. 3.4.1 Fe intermetallic phases database creation

The EDS spectra show that every intermetallic particle contain Al and Fe, so all the compound listed in Pearson's Handbook of Crystallographic Data for Intermetallic phases[28] containing Al and Fe were selected as possible phases for identification (See appendices A). The crystallographic data were entered into HKL Channel 5 Twist diffraction database creator.

For the identification of each intermetallic particle, the HKL software automatically suggests solutions for a given EBSD pattern ranked by lowest MAD (Mean Angular Deviation) as an index of 'goodness of fit'. For acceptable identification solutions, the MAD number should be less than 0.7 in the present study.

3. 3.4.2 EBSD sample preparation

The use of EBSD has quite high requirement of the sample quality. In the present study, a procedure for EBSD sample preparation was developed (Table 3.3).

Table 3.3: Four steps procedures for the EBSD sample preparation.

Steps	Load (N)	Speed rmp/Direction	Time (minutes)
120-500 grit SiC, water	slightly hand press	60/Same	Until plane
6-μ diamond abrasive	15	90-120/Same	8
1-μ diamond abrasive	15	90-120/Same	2
0.05 Microcloth with colloidal silica	10	60-90/Same	3.5

As illustrated in Figure 3.7, the dashed line on the EBSD sample is parallel to the casting surface/chill end, which stands for a position to be studied. Six fields with dimensions about 150μm x 150μm were chosen along the line under a magnification of 500X. On the corner of each field, four marks were made using Micro hardness in order to find the field easily under SEM:

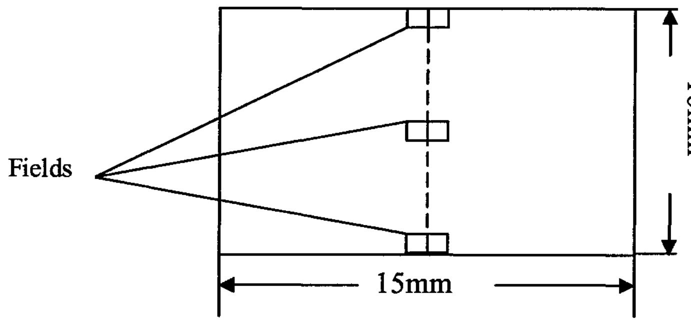

Figure 3.7: Schematic illustrates the 6 fields chosen in a sample.

The particles size smaller than 0.5μm x 0.5μm in dimension cannot be identified due to the poor quality of diffraction patterns, which take up about 5% of the total particles. Generally, there are totally 80 ~ 100 particles analyzed in the six fields of a sample.

3. 3.4.3 Fe intermetallic Phases quantitafication

After all the Fe intermetallic particles were identified, phase quantitafication was done by CLEMEX image analysis. In addition to the volume fraction, some other parameters of the Fe intermetallic particles such as Count, Perimeter, and Density were measured by CLEMEX image analysis.

By using CLEMEX Image Analyzer, there are two steps to calculate the area percentage of each type of Fe intermetallic phases in one field. Firstly, all the Fe intermetallic phases appear on the image are selected automatically according to the brightness difference between Fe intermetallic particles and Al matrix. Secondly, each type of Fe phase is distinguished and selected manually according to the EBSD identification results.

The routine of CLEMEX Image Analyzer used in the present study see appendices B.

Chapter 4 Results and Discussion

4.1 Phase chacterization in an AA5657 DC cast ingot

4.1.1 Ingot microstructure

The microstructure of AA5657 DC cast ingot is shown in Figure 4.1.

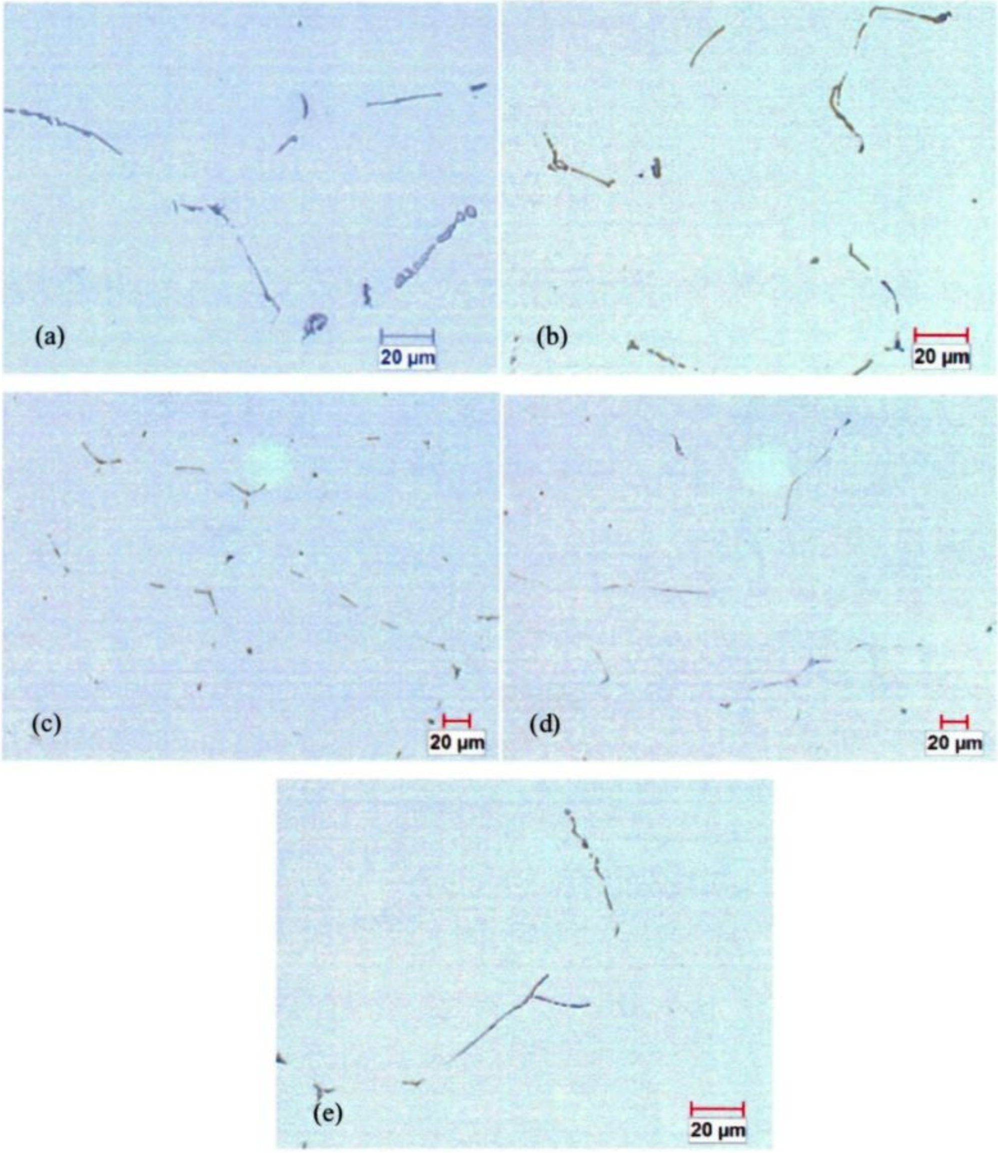

Figure 4.1: Microstructure of AA5657 cast ingot at the position away from casting surface at 10 mm (a), 40 mm (b), 90 mm (c), 140 mm (d) and 300 mm (e).

The microstructure of AA5657 alloy ingot show that the Fe intermetallic phases are grow along the interdendritic regions of aluminum cells, which indicates that the Fe intermetallic phases are form in the last stage of solidification process.

4.1.2 Fe intermetallic phases morphology and EDS results

In the DC cast AA5657 ingots, four kinds of typical morphologies of Fe intermetallic phases were found. The morphologies of the Fe intermetallic particles under Optical Microscope and SEM were shown in Figure 4.2 and Figure 4.3, Figure 4.4 shows the phase morphologies in deep-etching samples:

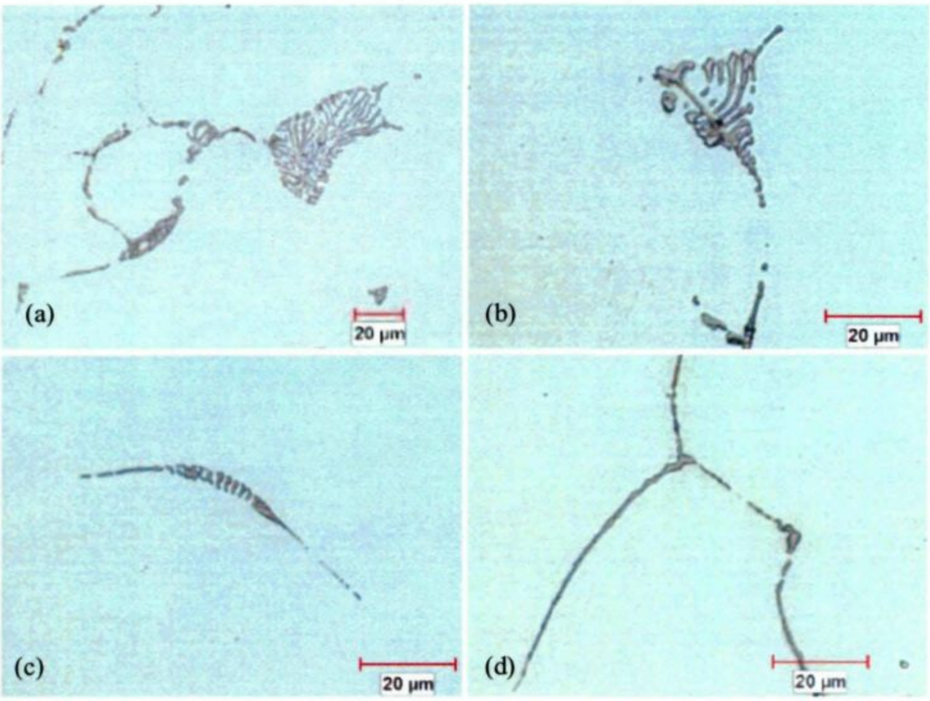

Figure 4.2: Typical Fe phases morphologies in the AA5657 cast ingot: (a) fine feathery like, (b) Chinese script, (c) curved plates with swings, (d) needle like.

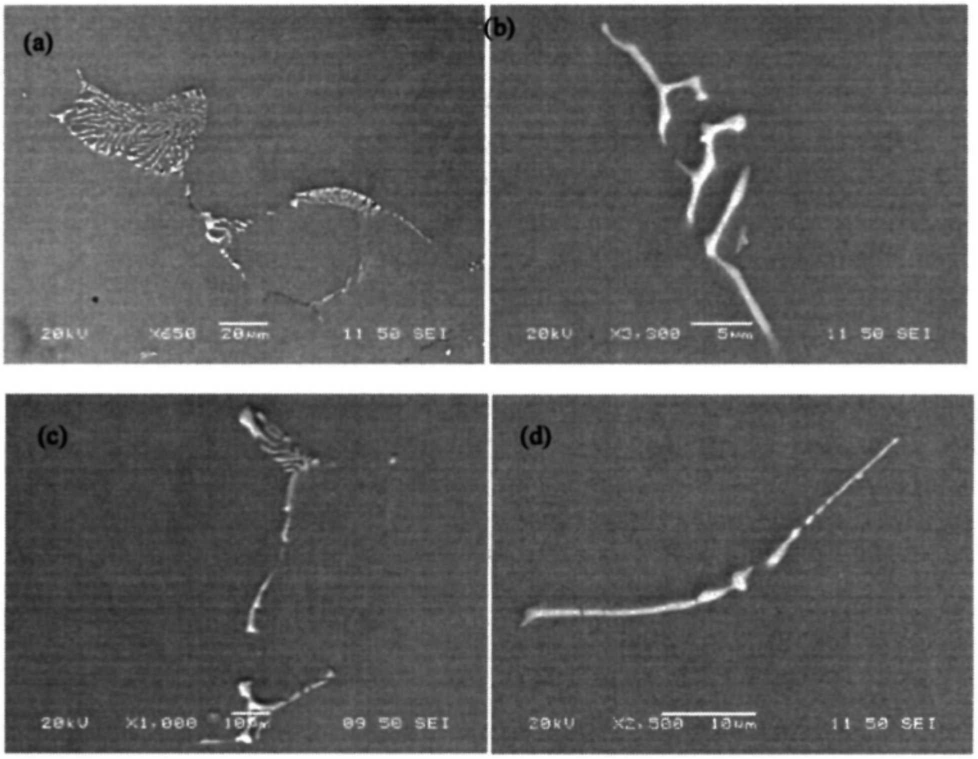

Figure 4.3: Fe intermetallic phases morphology under SEM. (a) fine feathery like, (b) Chinese script, (c) curved plates, (d) needle like.

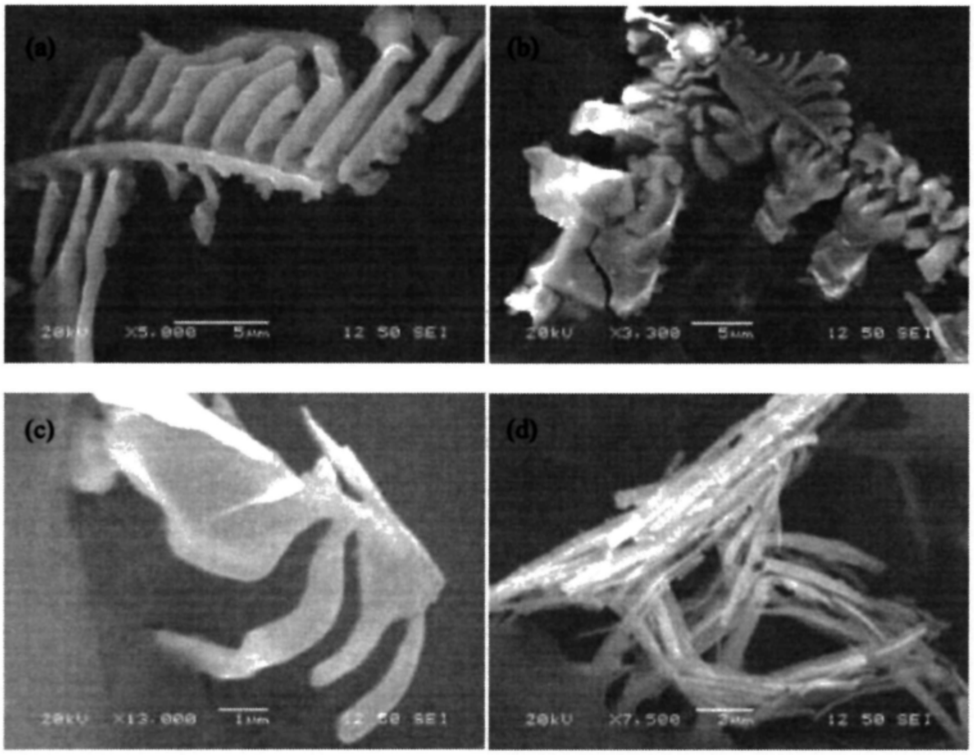

Figure 4.4: Fe intermetallic phases morphology (deep-etching) under SEM. (a) fine feathery like, (b) Chinese script, (c) curved plates, (d) needle like.

The EDS results of different phases are shown in Figure 4.5:

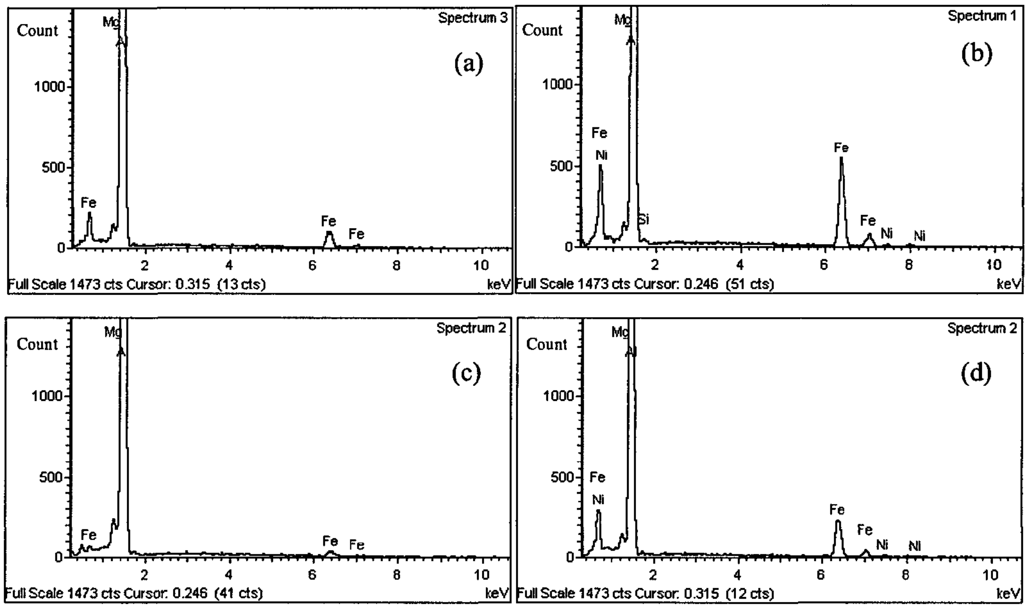

Figure 4.5: Typical EDS results of Fe intermetallic phases. (a) Fine feathery like, (b) Chinese script, (c) curved plates, (d) needle like.

From the EDS results in Figure 4.5, we can know clearly that these particles are Fe containing phases. Moreover, Mg was detected in each particle of Fe intermetallic phases, because AA5657 alloy contains 0.82 wt% Mg. In addition, in some chinese script and needle like Fe intermetallic phases, some amount of Ni content can be frequently found (Figure 4.5 (b) and Figure 4.5 (c)). Especially, in Figure 4.5 (b), we can see that the chinese script particles always contain some Si, which makes it easier to be distinguished from other phase.

Although it is possible to identify some Fe intermetallic phases according to their typical morphology and EDS spectra, it is still not sufficient, sometimes may even cause misidentification due to two reasons:

(1) As found in the present study only a small part (about 20%) of Fe intermetallic particles appears the typical morphology. In addition, according to the

work of M.V. Kral[53, 54] et all and Y.J. Li et L. Arnberg[55,56], a certain Fe intermetallic phase can have different morphologies.

(2) EDS can give a semi-quantitative compositional analysis of the particle, the stoichiometry of Fe phases is still uncertain according to EDS results. Moreover, the Fe intermetallic particles often adopt relatively small size (i.e. 1 ~ 5 μm), which may cause the EDS signal be obtained from the matrix and make the results at least partially incorrect.

4.1.3 Phase identification using EBSD technique

By using EBSD technique, the four types of Fe intermetallic phases appearing in the cast ingot were identified. It was found that the crystal structure of the intermetallic compound with a feathery like morphology was similar to Al_mFe; The crystal structure of the intermetallic phase with chinese-script morphology was agree well with Al_7Fe_2Si; The crystal structure of the intermetallic phase with curved plates morphology was agree well with Al_6Fe and the crystal structure of the intermetallic phase the needle like morphology can match well with Al_3Fe. The following images show the diffraction patterns and its corresponding solutions of different intermetallic phases given by EBSD.

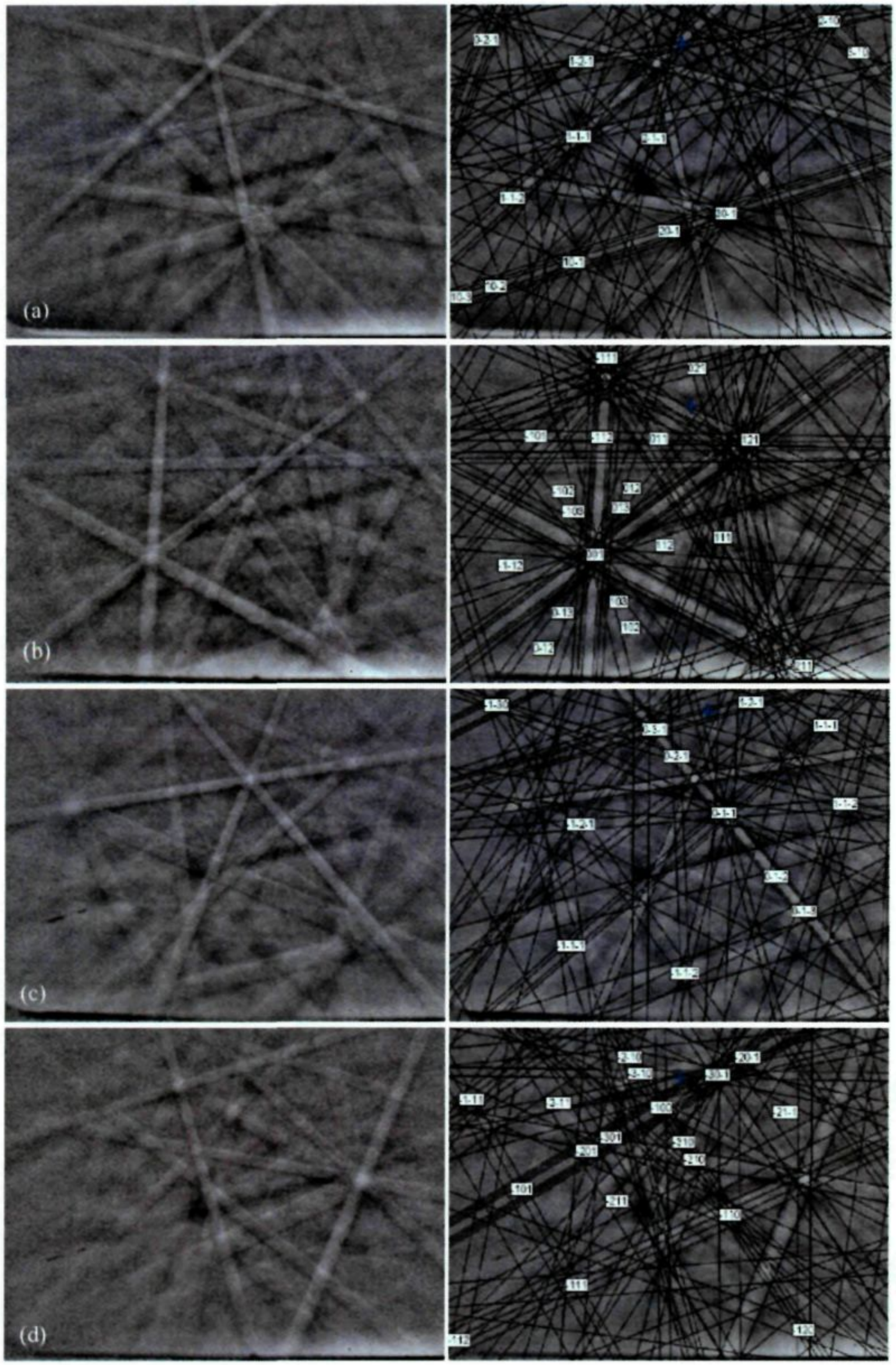

Figure 4.6: Four types of EBSD patterns and corresponding solutions. (a) Al_mFe, (b) Al_7Fe_2Si, (c) Al_6Fe, (d) Al_3Fe.

4.1.4 Phase quantitafication

5 samples with different distance from the casting surface were taken across the thickness of a commercial AA5657 DC cast ingot from Rio Tinto Alcan (as shown in Figure 4.7).

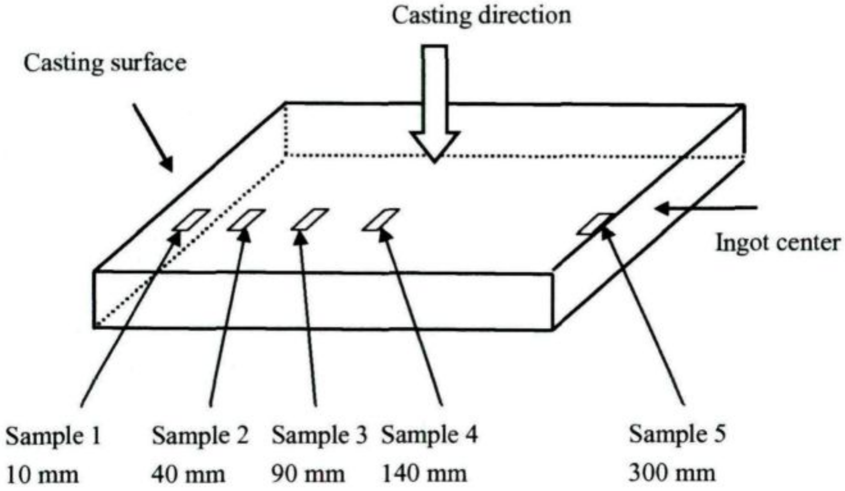

Figure 4.7 Schematic shows the sampling position in an AA5657 DC cast ingot.

The distribution of Fe phases in the ingot is shown in Figure 4.8.

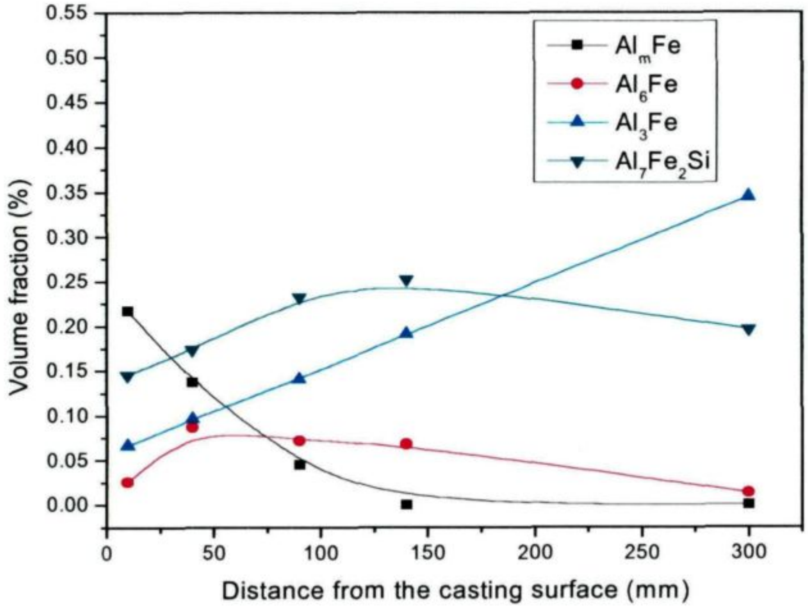

Figure 4.8: Fe intermetallic phases distribution AA5657 cast ingot.

As shown in Figure 4.8, Al_mFe is a dominant phase in the position near the casting surface. It decreases with the increase of the distance away from the casting surface to the ingot center. Al_3Fe increase with the distance increase, approximately linear, and it becomes a dominant phase after the position of 140 mm away from the casting surface in the ingot. The Al_7Fe_2Si can be frequently seen from the casting surface to the ingot center. It increases from the casting surface up to 140 mm and then remains almost constant. A small amount of Al_6Fe was found in the surface and it increase at first and then decreases with the distance away from the casting surface to the center.

The distribution of each phase can be explained by the cooling rates change in the ingot. At the position 10 mm from the casting surface, because the secondary cooling in the DC casting process, it has quite high local cooling rate. Thus, the phase Al_mFe, which has the highest undercooling forms. With the distance increase, the cooling rates gradually decrease due to longer thermal diffusion paths. In the ingot center, the cooling rates can be as low as less than 1 K/s, where forms preferentially the equilibrium phase Al_3Fe. As reported by X.-G. Chen[12], the Al_7Fe_2Si phase becomes a major intermetallic phase at higher level of Si content. It is the first time in the present study to find that the hexagonal Al_7Fe_2Si phase is one of the dominant phase across the AA5657 DC cast ingot, which may be caused by the high amount of Mg content. Because the element Mg also has hexagonal crystal structure[57], it is possible to promote the formation of hexagonal Al_7Fe_2Si particles. As found in the present study, there are no visible FTZs revealed in AA5657 DC cast ingot, which maybe has some relationship with the α-AlFeSi phase distribution. The phenomenon that increase of α-AlFeSi phase can make the FTZs invisible was also found by S.J. Maggs et al[13] in the alloy with Fe/Si of 2.

By using the methods that has developed in the present research, the Fe intermetallic phases present in the industry DC cast AA5657 alloy ingot were characterized. The methods that have been used in this study solved the problem of quantitafication limit of the Fe phases, which can be quite useful in the future study of this field.

4.2 Phase characterization in an AA1050 DC cast ingot across the FTZs

A lot of research has been carried out to study the FTZs formation in 1xxx-series alloy ingots, and it is more or less clear that the formation of Al_mFe is the main factor of FTZ. However, all the results were given based on qualitative or semi-quantitative analysis. It is still not clear about the transition of Fe intermetallic phases across the FTZ. Thus, in order to better understand the Fe intermetallic phases in the ingot with visible FTZs, a slice of an industry DC cast AA1050 ingot from Rio Tinto Alcan was studied based on EBSD technique and EDS. Its chemical composition was analyzed and shown in Table 4.1:

Table 4.1 Chemical composition of an AA1050 DC cast ingot (wt.%).

Alloy	Elements									
	Fe	Si	V	Ni	Mg	Cu	Mn	Gr	Zn	Al
AA1050	0.26	0.04	0.015	0.034	0.001	0.003	0.003	0.002	0.002	BAL

For this DC cast AA1050 ingot, the FTZs were clearly revealed by using caustic soda (NaOH) etching method, as shown in Figure 4.9:

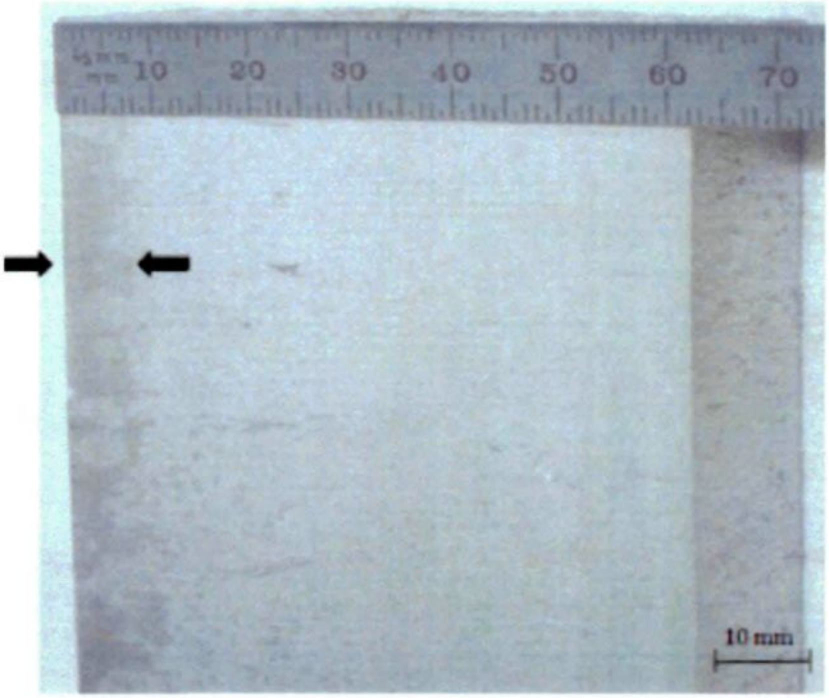

Figure 4.9: FTZ revealed in AA1050 alloy ingot. FTZ is shown between the 2 arrows. The thickness of FTZ is about 6~8mm. Etched in 15% NaOH heated at 60~70°C for 5 minutes.

In the present study, six positions are chosen across the FTZs, which are 3mm, 6mm, 9mm, 12mm, 18mm, and 24mm away from the ingot casting surface. Similarly with the phase characterization in AA5657 cast ingot, the Fe intermetallic phases appearing in the fields were identified by the combination of EBSD and EDS.

4.2.1 Ingot microstructure

Under the Optical Microscope, the microstructure appears obviously difference in and out of the FTZs (Figure 4.10). This difference is caused by the difference in Fe intermetallic phases content. Different type of Fe intermetallic phases have different response to a given etchant, which appear in macro observation as color difference between areas on the ingot surface.

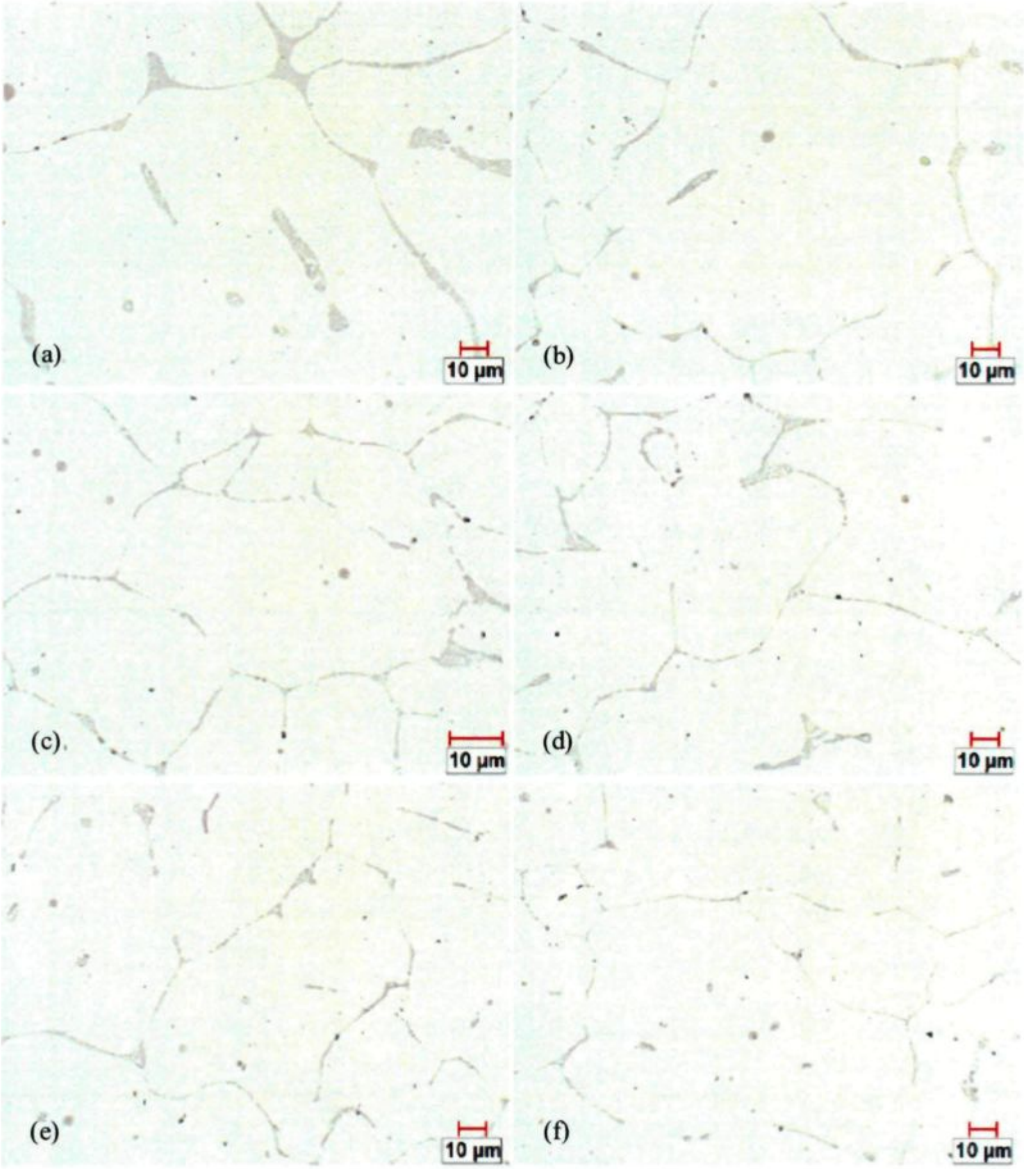

Figure 4.10: Microstructure of AA1050 ingot across the FTZs. (a) 3 mm, (b) 6 mm, (c) 9 mm, (d) 12 mm, (e) 18mm, (f) 24 mm.

4.2.2 EDS and Deep-etching morphology

In the AA1050 ingot, the EDS results (Figure 4.11) of Al_mFe, Al_6Fe, α-AlFeSi and Al_3Fe phases appear similar with those in AA5657 alloy: α-AlFeSi contains some Si and both α-AlFeSi and Al_3Fe always has some Ni content.

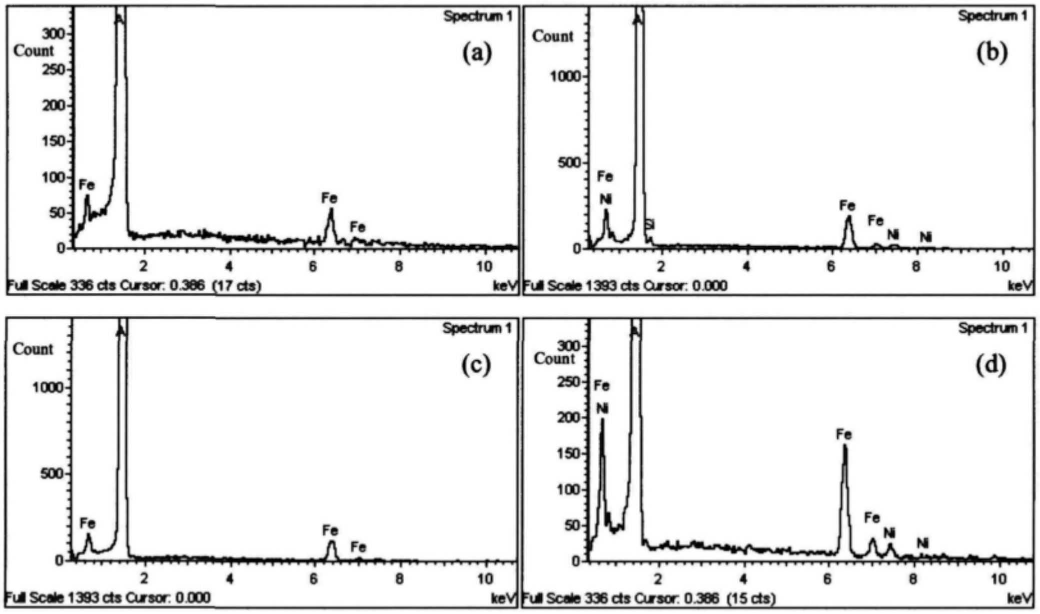

Figure 4.11: EDS results of Fe intermetallic phases in AA1050 ingot. (a) Al_mFe, (b) Al_7Fe_2Si, (c) Al_6Fe, (d)Al_3Fe.

Their morphologies of four types of Fe intermetallic phases after deep-etching are shown in Figure 4.12.

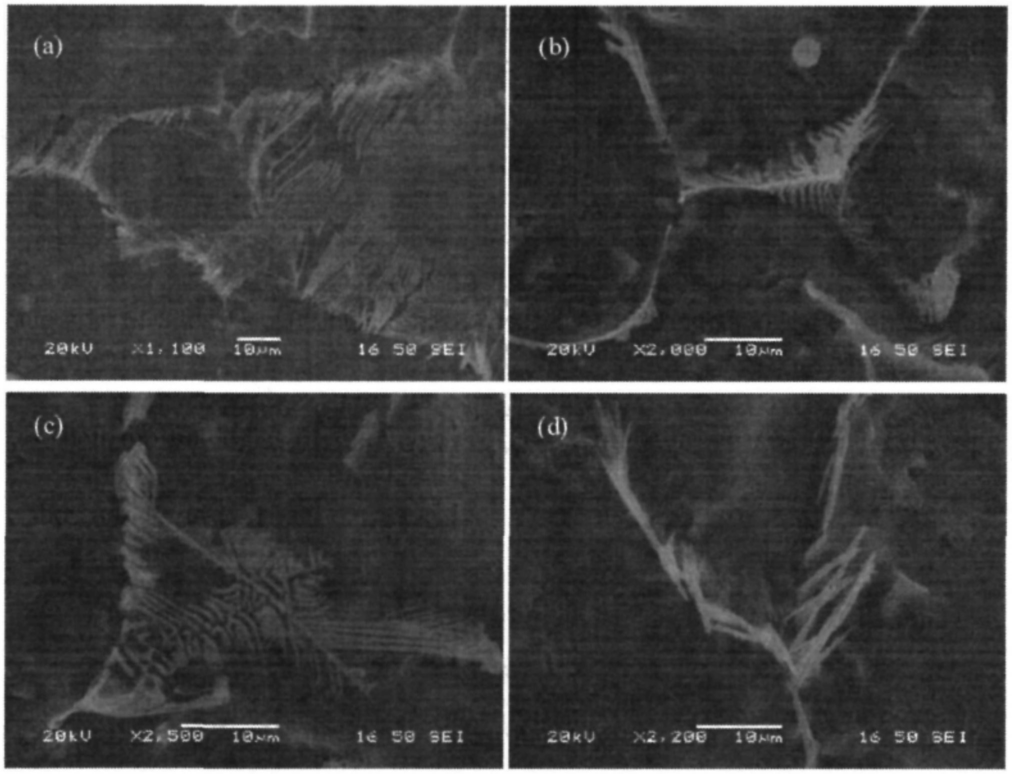

Figure 4.12: Morphologies of Fe intermetallic phases (Deep-etched). (a) Al_mFe, (b) Al_6Fe, (c) Al_7Fe_2Si, (d) Al_3Fe.

From Figure 4.12, we can find that the typical morphologies of Fe intermetallic phases in AA1050 alloy ingot appear quite similar with those in AA5657 alloy ingot: Al_mFe has fine feathery like morphology, Al_6Fe grow into curved plate with swings, α-AlFeSi has chinese-script morphology and Al_3Fe appears needle like morphology.

In addition to the four Fe intermetallic phases mentioned above, another Fe phase that containing high levels of Ni was also observed in this ingot. The morphology of this phase is quite unique (Figure 4.13).

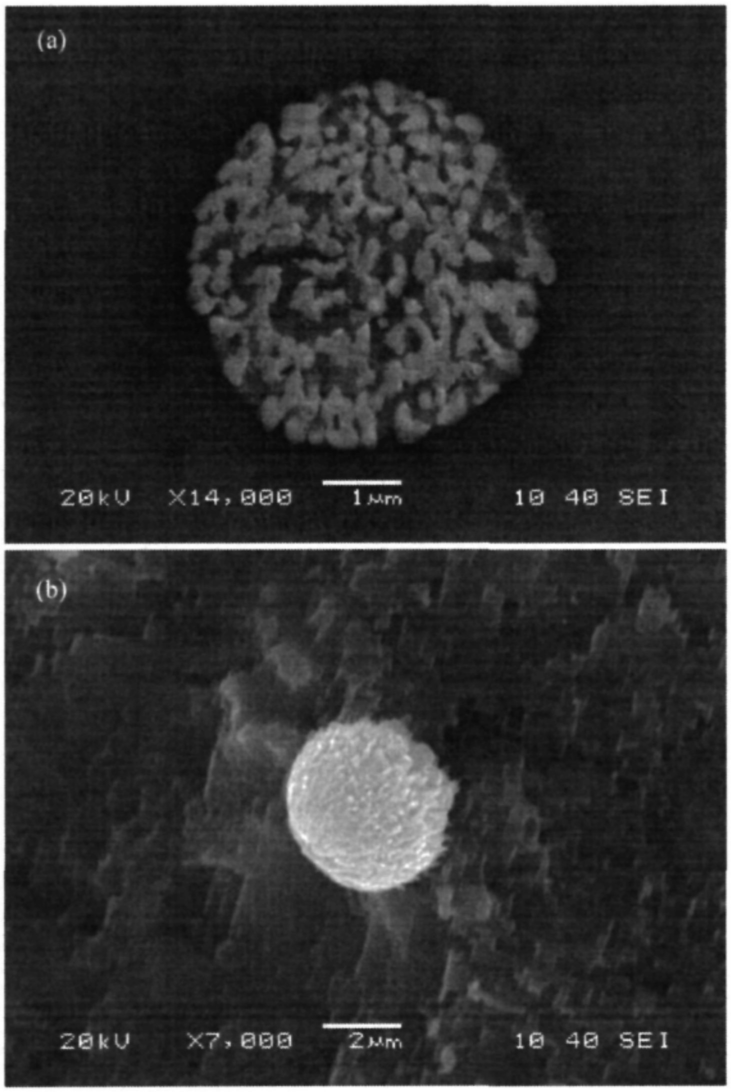

Figure 4.13: Morphology of Ni containing intermetallic phase under SEM in SEI mode. a) Before deep-etching, b) After deep-etching.

The Ni containing phase morphology often appears round particle with a diameter of about 2 ~ 3μm. The typical EDS spectra is shown in Figure 4.14, from statistic calculation we can get that the Fe/Ni ratio of this particle is about 7 (Table 4.2), while the Ni/Fe ratio of other types of Fe intermetallic particles α-AlFeSi and Al_3Fe can be as low as 0.1%, which indicates that the Ni containing phase contains higher level of Ni.

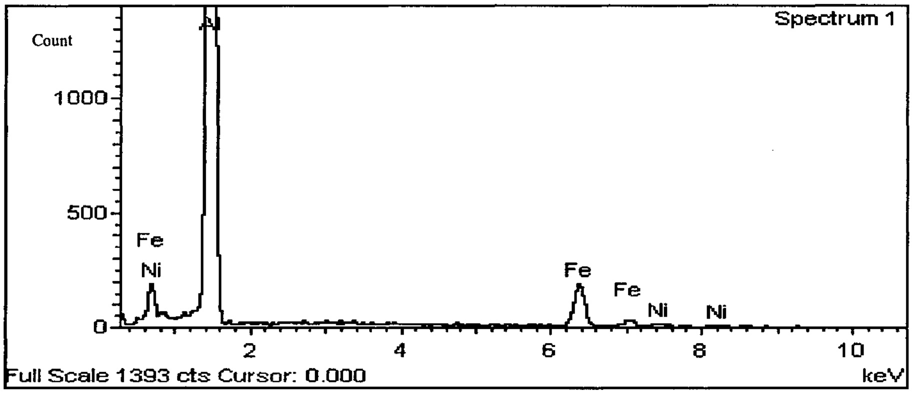

Figure 4.14: EDS results of a Ni containing particle.

Table 4.2: Chemical composition of Ni containing particles in 1xxx-series alloy ingot, atoms%

		Fe	Ni	Atoms ratio Fe/Ni	Average Fe/Ni
Particles	No. 1	5.43	0.78	6.96	6.87
	No. 2	3.43	0.52	6.59	
	No. 3	5.64	0.91	6.19	
	No. 4	5.34	0.82	6.51	
	No. 5	6.02	0.82	7.34	
	No. 6	6.05	0.84	7.20	
	No. 7	5.17	0.71	7.28	

Since it cannot be matched with any known phase in ternary Al-Fe-Ni system, we denoted this Ni containing phase as AlFeNi. The formation of this intermetallic phase in this alloy ingot is caused by the high content of Ni (see Table 4.1). Similar with the Fe element, the solid solubility of nickel in aluminum is quite low, which is less than 0.04%, above this amount, it will present as an insoluble intermetallic phases, usually in combination with iron.

4.2.3 Fe Phase characterization using EBSD technique

For the new Ni containing phase, it is very difficult to get good diffraction patterns, which was characterized based on its morphology and EDS results. The diffraction patterns and their corresponding solutions of four types of Fe intermetallic phases are shown in Figure 4.15:

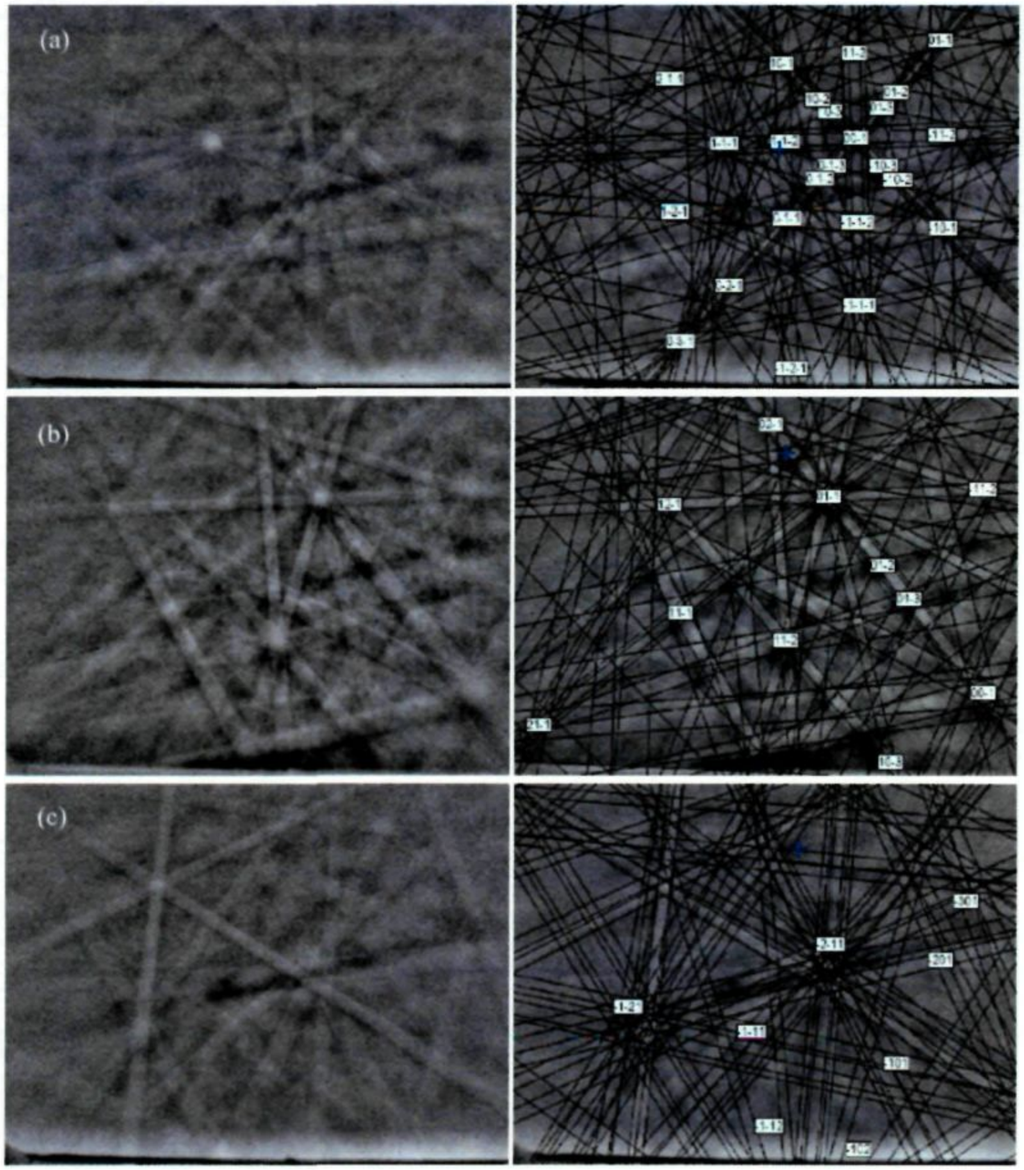

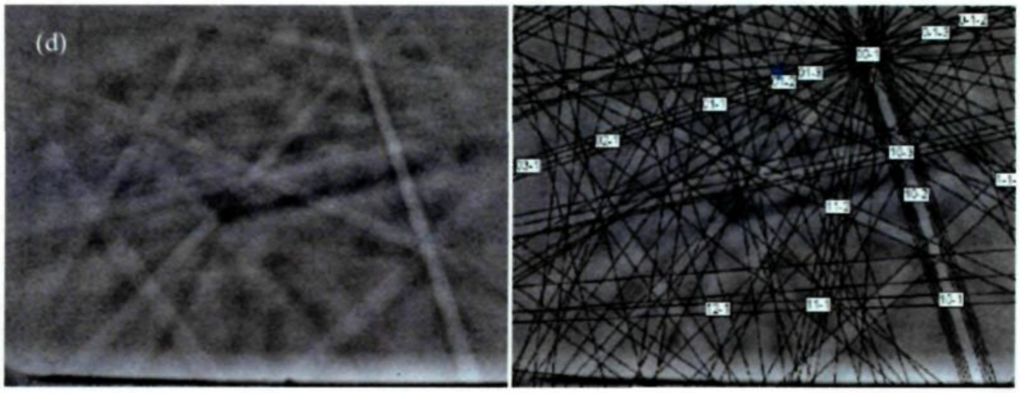

Figure 4.15: EBSD diffraction patterns and corresponding solutions of different type of Fe intermetallic phases in AA1050 alloy ingot, a) Al_mFe, b) Al_6Fe, c) Al_7Fe_2Si, d) Al_3Fe.

4.2.4 Phase quantitafication

The volume fraction of each phase was measured by using Image Analysis (Figure 4.16).

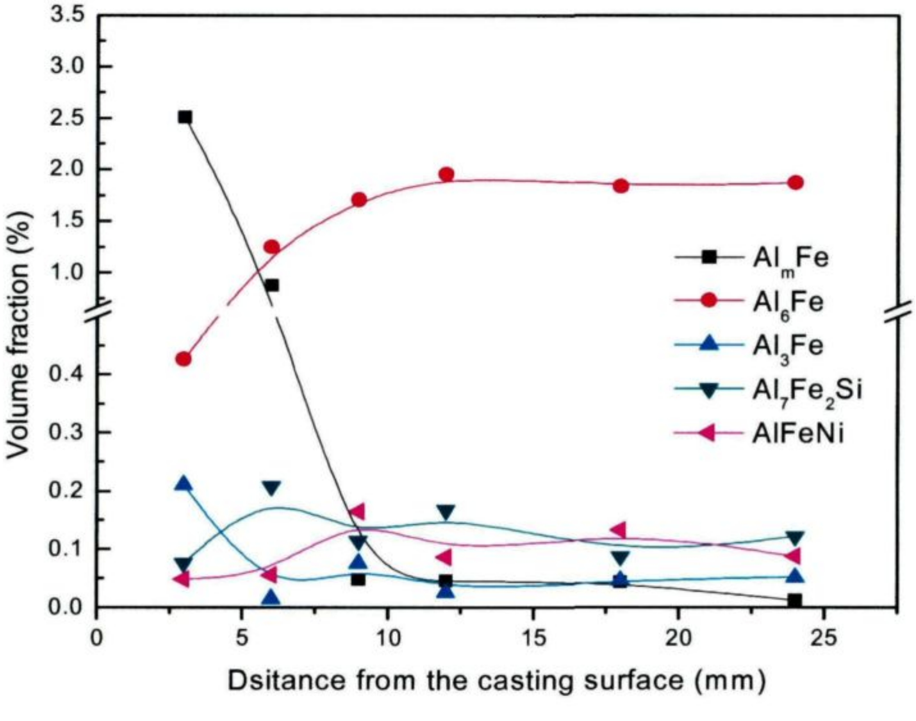

Figure 4.16: Fe intermetallic phase distribution across the FTZs in AA1050 alloy ingot.

From Figure 4.16, we can find that at the position 3 mm from the casting surface, the dominate phase is Al_mFe, at the position 6 mm the dominate phases are Al_mFe and

Al_6Fe, while Al_6Fe become the predominant phase after 9 mm. Because Al_mFe and Al_6Fe have different responses to a given etchant, the FTZs become visible after etching. Till now, it is quite clear that the transition from Al_mFe to Al_6Fe is the main reason that causes the FTZ visible.

In addition to the transition of Al_mFe and Al_6Fe, there also exist transitions of Al_3Fe, Al_7Fe_2Si and AlFeNi phase. The amount of Al_3Fe was found decrease from the position 3 mm to 24 mm. The formation of Al_3Fe in 3 mm from the casting surface is caused by the air gap during DC casting process, due to the relative low cooling rates. The heat extraction in air gap region is slow and leads to the shell zone of the ingot reheating, or even re-melting partially from inside. Thus, the local cooling rates in air gap region can be slow enough due to form the equilibrium phase Al_3Fe. This 1xxx alloy ingot has very low Si containing (0.04 wt %), so the ternary phase Al_7Fe_2Si only appears in the trace level and most of it was found at the position 6mm and 9 mm. For the AlFeNi phase, it was found the most at the position 9 mm, it is great possible that the formation of AlFeNi is affect by the local cooling rates.

In general, the transition of Fe intermetallic phases across the FTZs was made quite clear in the present study, there is no doubt that the formation of FTZs is caused mainly by the phase transition between Al_mFe and Al_6Fe.

4.3 DC simulator and Fe intermetallic phases in DC simulator cast AA5657 ingots

4.3.1 DC simulator

Using the DC cast simulator apparatus, AA5657 alloy ingots with different Ni and V levels were cast, the cast ingots are shown in Figure 4.17:

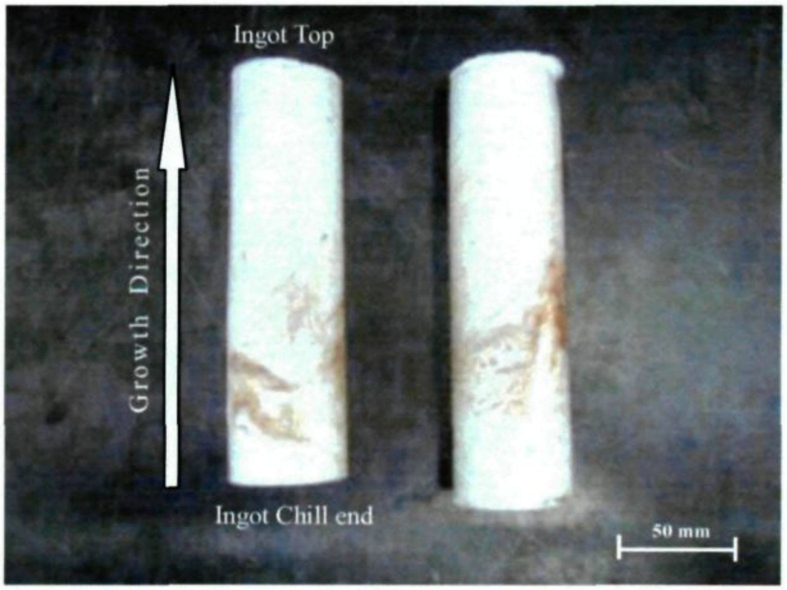

Figure 4.17: DC simulator casting ingots in the lab.

The dimension of the DC cast simulator Al ingots is about 38 mm in diameter and 150 mm in length. In the solidification process, cooling curves (Figure 4.18) were obtained from the thermocouples T1 ~ T5, which were located in the center of the DC cast mould. The position of the thermocouples from T1 to T5 were 20 mm, 45 mm, 70 mm, 95 mm and 120 mm away from the chill end.

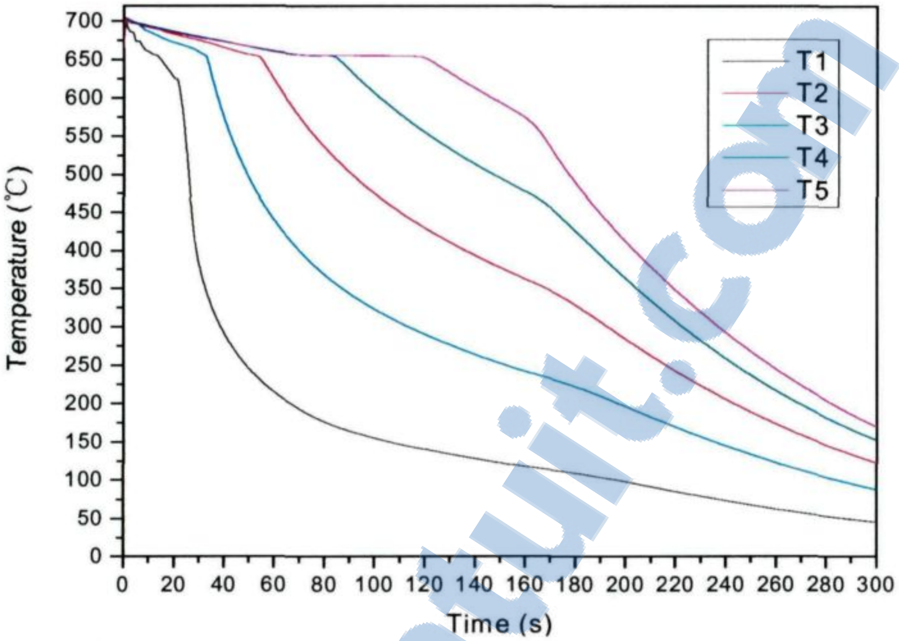

Figure 4.18: Cooling curves got from DC simulator casting AA5657 alloy.

From the cooling datas, the average cooling rates VS Distance were calculated and shown in Figure 4.19:

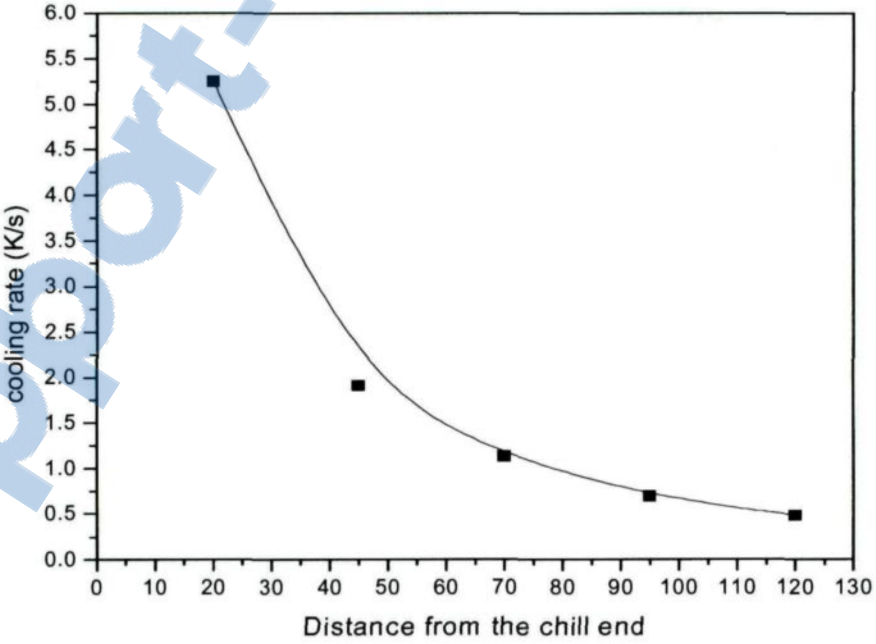

Figure 4.19: The average cooling rates in different position of the ingot from 700℃ to 650℃.

From Figure 4.19 we can see that at the position of 20 mm from the chill end, the cooling rate is about 5.6℃/s, while at the position of 120 mm, the cooling rate is as low as 0.5℃/s. The average cooling rates suggest that the cooling rate decrease greatly from the position near the chill end to the top of the DC simulator cast ingots, which provide different solidification conditions for the formation of Fe intermetallic phases to form.

A thermal analysis was carried out to study the solidification behavior of AA5657 alloy (see chapter 3.2). During the solidification process, the eutectic reaction of different Fe intermetallic phases cause heat release and cause local temperature gradient change, which may be reflected as peaks on the first derivation curve. Figure 4.20 shows a cooling curve and first derivation obtained by a thermocouple from the base AA5657 alloy cooled at 1.28 °C/s. The peaks on the first derivation is great possible to be caused by the reaction of α-Al, Al_3Fe, Al_6Fe, Al_mFe and α-AlFeSi according to their eutectic temperature (650℃~610℃)[5, 59].

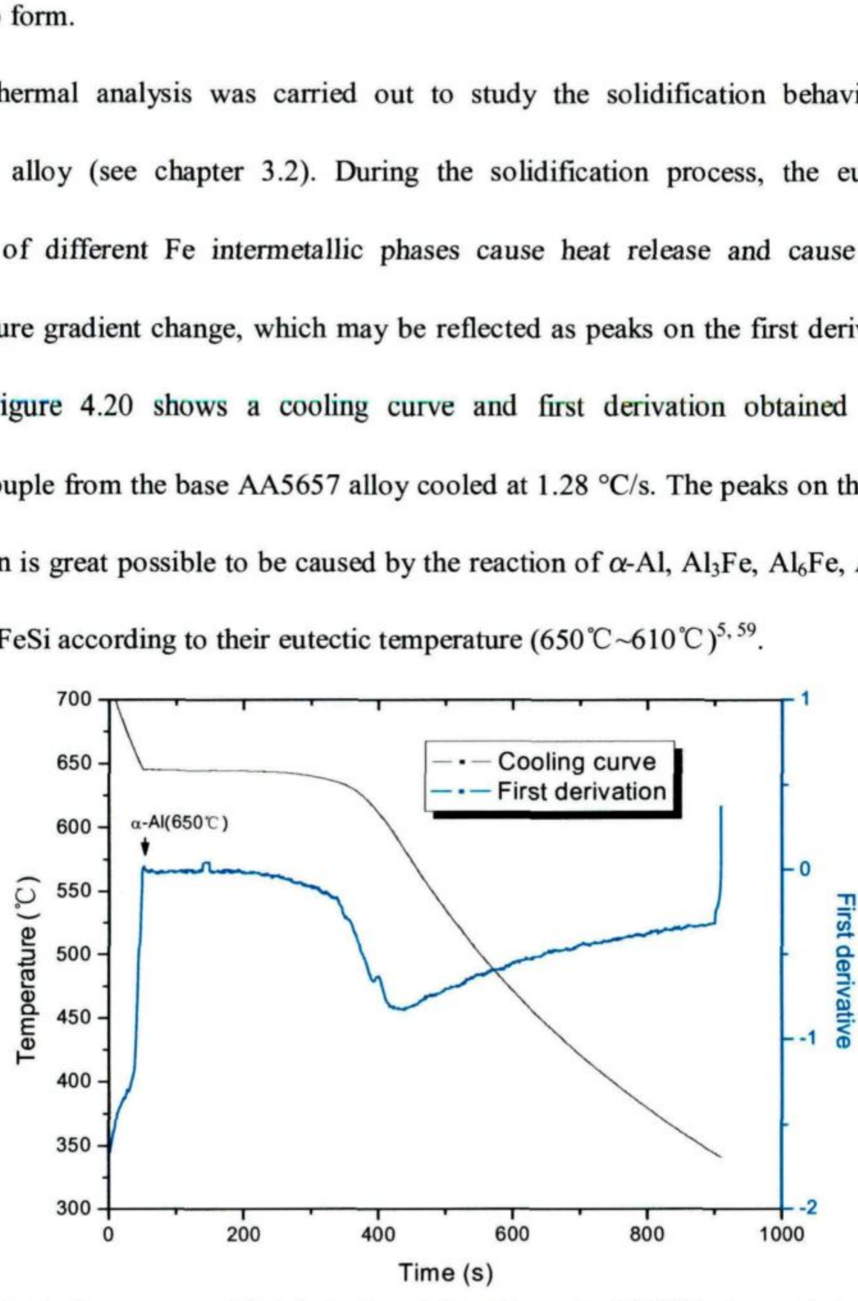

Figure 4.20: Cooling curve and first derivation obtained from the AA5657 alloy cooled at 1.28 °C/s.

4.3.2 Fe intermetallic phases in the base material of DC simulator cast AA5657 ingots (A01 alloy in Table 3.2)

In order to characterize the Fe intermetallic phases content in A01 alloy, four samples with a distance of 20 mm, 40 mm, 60 mm and 100 mm from the chill end were taken from ingot A01.

4.3.2.1 Ingot microstructure

The ingot microstructures of different positions are shown in Figure 4.21:

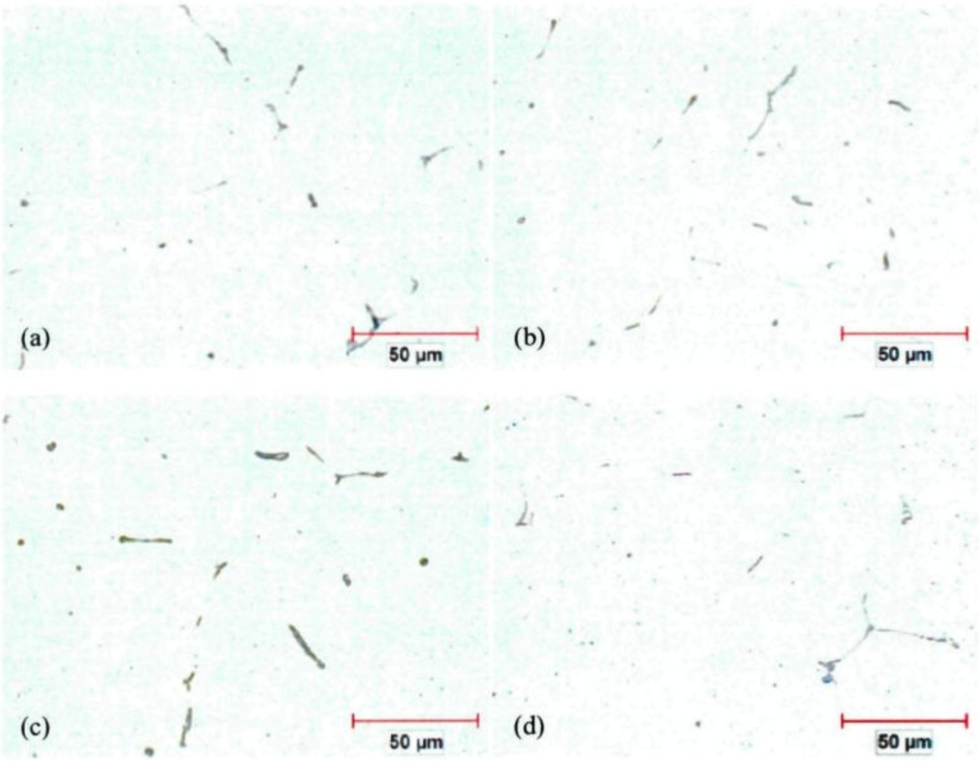

Figure 4.21: Microstructure of DC simulator casting AA5657 alloy taken from (a) 20 mm, (b) 40 mm, (c) 60 mm, (d) 100 mm from the chill end.

We can see from Figure 4.21 that the microstructure of DC simulator cast AA5657 alloy in different position has no major difference. As the Fe intermetallic phases characteristics are similar to those in industry ingots, The Fe particles were firstly characterized by using Optical Microscope, Deep-etching method, and EDS technique. Four types of Fe intermetallic phases were found in A01 alloy ingot, the typical morphology and their corresponding EDS spectra are shown in Figures 4.22 - 4.24:

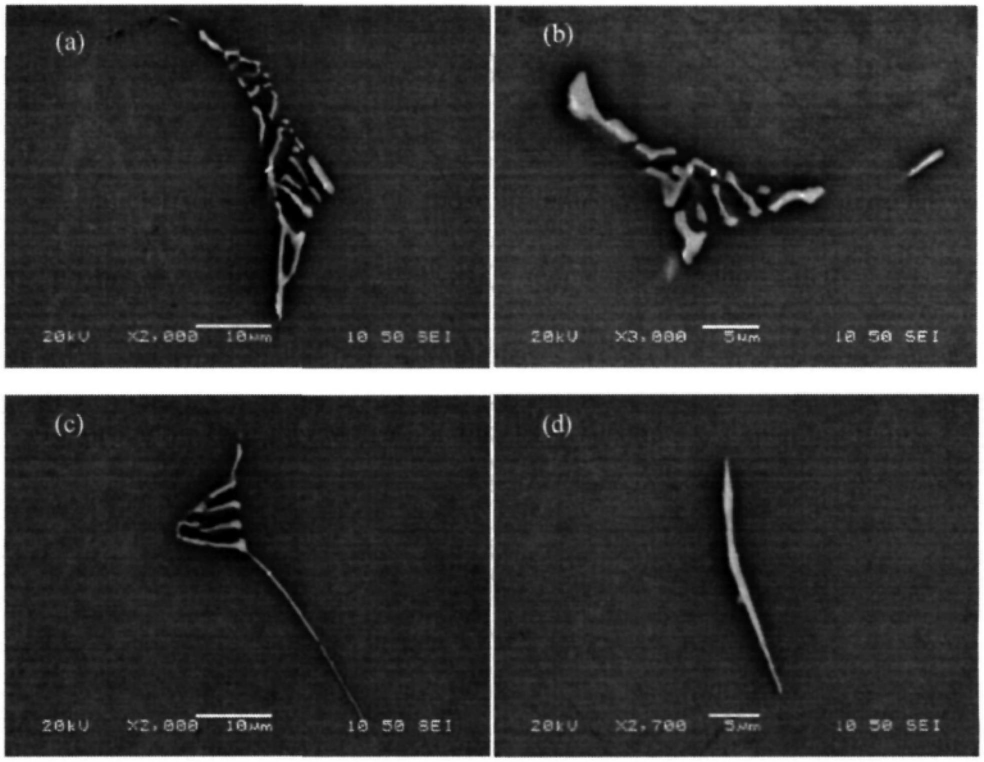

Figure 4.22: Fe intermetallic phases morphology under SEM. (a) fine feathery like, (b) Chinese script, (c) curved plates with wings, (d) needle like.

As mentioned before, the 2-D morphology of Al_mFe, α-AlFeSi and Al_6Fe mostly has the shape of interdendritic channels, and it is difficult to distinguish them from each other (Figure 4.22). The 3-D morphology revealed by using deep-etching method is more helpful for the four types of Fe intermetallic phases identification (Figure 4.23).

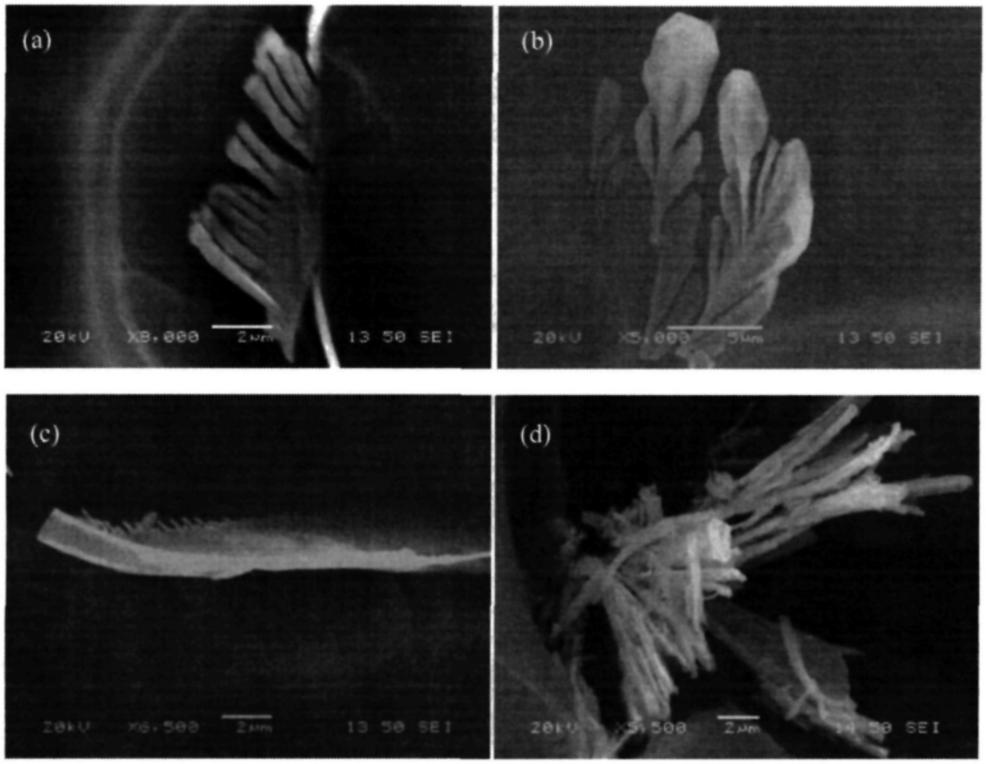

Figure 4.23: Fe intermetallic phases morphology under SEM (Deep-etching). (a) fine feathery like, (b) Chinese script, (c) curved plates, (d) needle like.

The EDS results of different phases are shown in Figure 4.24:

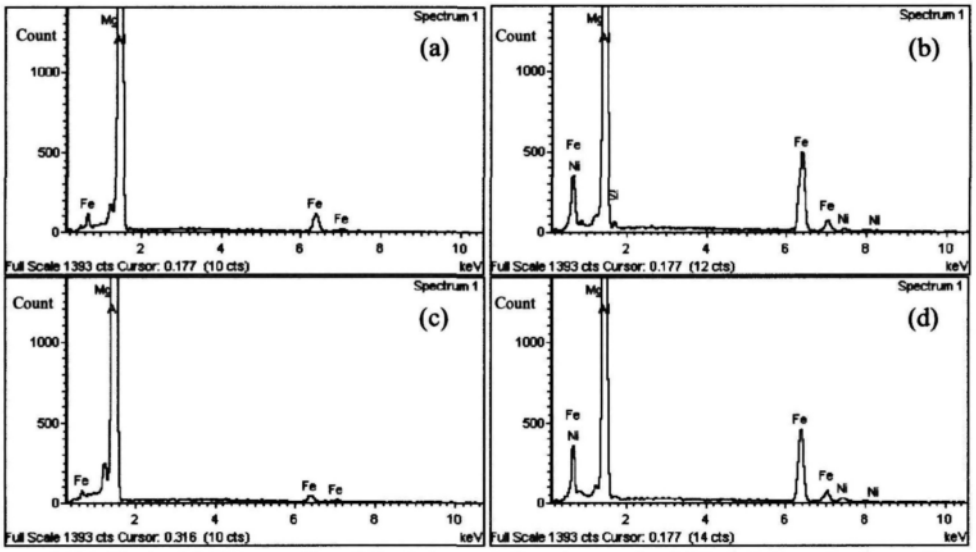

Figure 4.24: Typical EDS results of Fe intermetallic phases in A01. (a) Fine feathery like, (b) Chinese script, (c) curved plates, (d) needle like.

The EDS results of the Fe intermetallic particles with Chinese script and needle like morphology show some amount of Ni content, which is similar with those in industry DC cast AA5657 alloy ingot (see chapter 4.1).

4.3.2.2 EBSD diffraction patterns

Using EBSD technique, we found the similar results as those in industry DC cast AA5657 ingot: the four types of Fe intermetallic phases appearing in A01 ingot were identified as Al_mFe, Al_7Fe_2Si, Al_6Fe and Al_3Fe. The following images show the diffraction patterns and their corresponding solutions of different intermetallic obtained by EBSD.

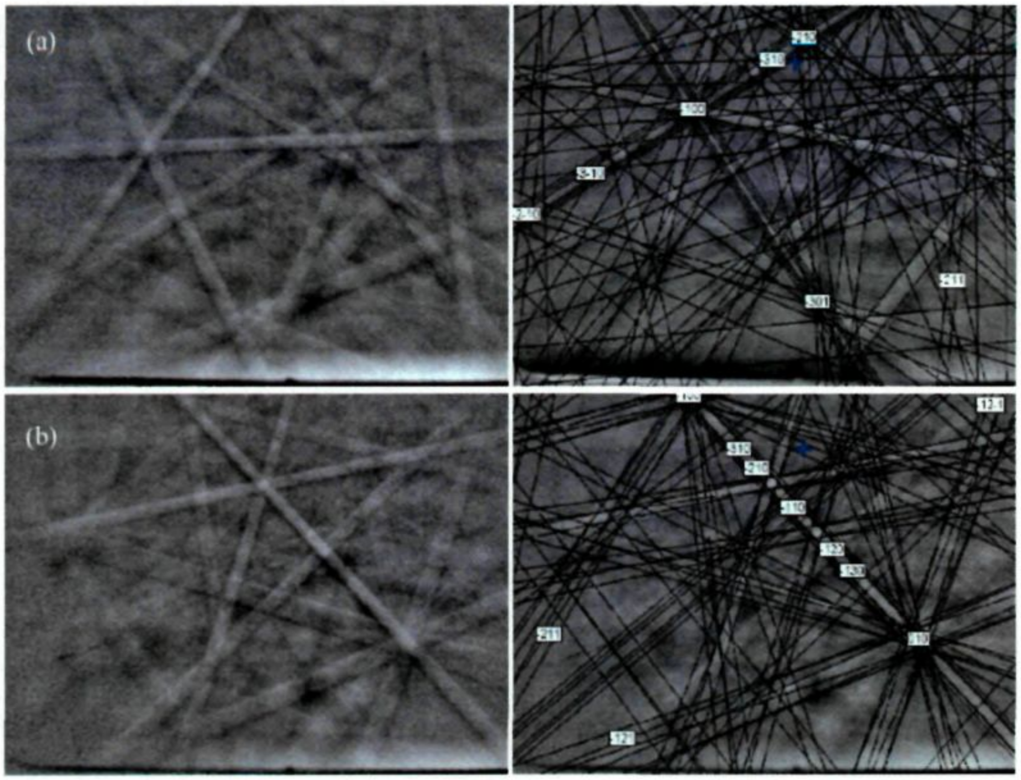

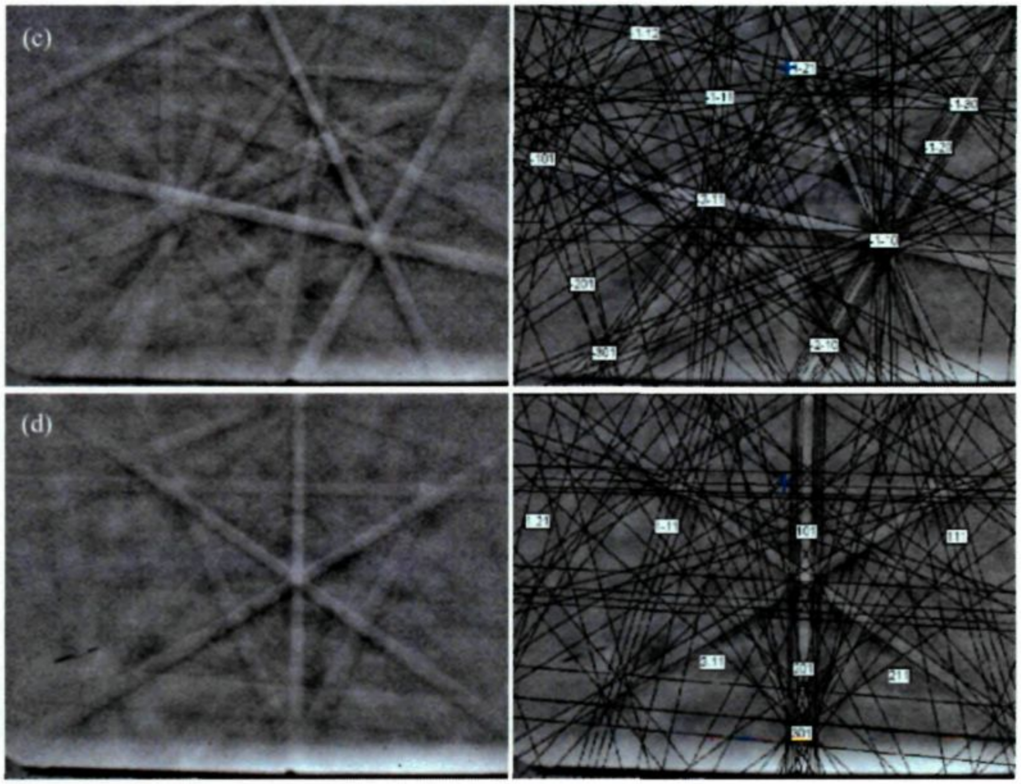

Figure 4.25:EBSD diffraction patterns and corresponding solutions of different type of Fe intermetallic phases in A01 alloy ingot, a) Al_mFe, b) Al_6Fe, c) Al_7Fe_2Si, d) Al_3Fe.

4.3.2.3 Image analysis results

By using the Clemex Image analysis software, the Area Percentage (Volume fraction) and other parameters (perimeter, count, density) of Fe intermetallic phases were measured and analyzed.

The distribution of Fe phases in A01 alloy is used to make comparation with all Ni and V added alloys, it is very important for the accuracy of the results. Thus, we made a verification of the results by characterizing other 10 fields in the position of 20 mm, 30 mm, 40 mm, 50 mm, 60mm, 80 mm, and 100 mm in A01 alloy. The combined distribution results of the Fe intermetallic phases are shown in Figure 4.26:

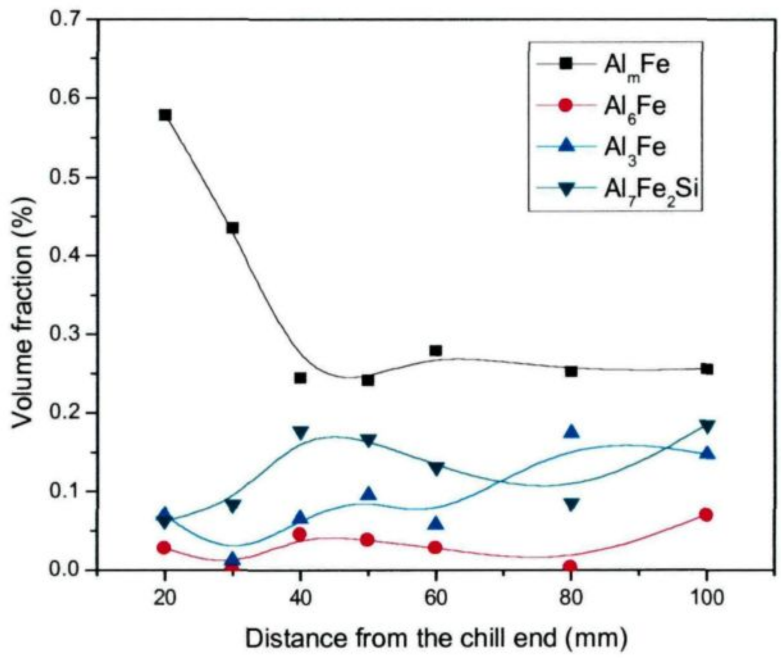

Figure 4.26: Fe intermetallic phase distribution in ingot A01.

As shown above, the volume fraction of Al_mFe decrease as the distances increase from the chill end; The Al_7Fe_2Si phase increase a little from position 20 mm to 40 mm, but from 40 mm to 80 mm, it decrease as the distance from the chill end increase, and it increase after 60 mm. For Al_3Fe, its volume fraction has a tendency to increase as the distance increase from the chill end. While for Al_6Fe, it was found only in trace level in the ingot. When compared the results with industry DC cast AA5657 ingot (See Figure 4.8), we can find that the biggest difference is that the relative amount of Al_7Fe_2Si, Al_3Fe and Al_6Fe phases are lower than the industry ingot. Although difference is exist, we can still found that the Fe intermetallic phase distribution in DC simulator cast ingot is similar with that within 100 mm from the casting surface in the commercial DC casting ingot. Thus, the lab DC simulator cast ingot can reproduce the solidification conditions of the industry DC casting ingot in the sub-surface region.

The distribution of total phases is shown in Figure 4.27:

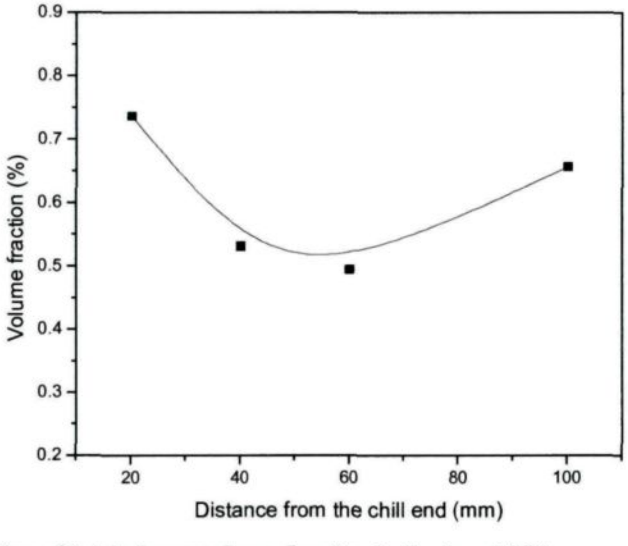

Figure 4.27: Distribution of total phase volume fraction in the ingot A01.

From Figure 4.27 we can find that the total volume fraction of Fe intermetallic phase in the position 20 mm from the chill end is a little higher than that in the other three positions, which is caused by the segregation during solidification process. The reason why the total volume fraction is high in the poaition of 100 mm is not clear.

The particle number in per unit area is defined as particle density of each Fe intermetallic phases, and it is shown in Figure 4.28:

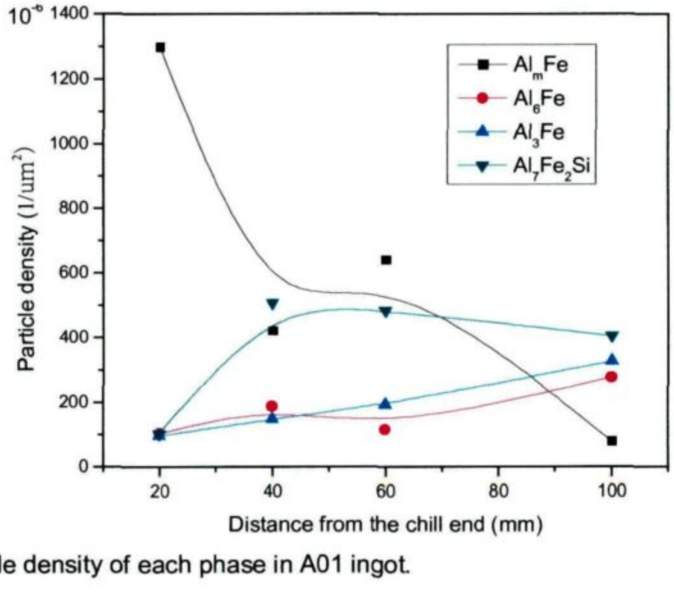

Figure 4.28: Particle density of each phase in A01 ingot.

The surface area of each particle has a liner relationship with perimeter, and has the following equation[58]:

$$S_v = 4L_A/\pi$$

Where S_v is surface area of the total particles per unit volume and L_A is popular average value of the total perimeter of particle per unit area. The surface area of each Fe intermetallic phases is shown in Figure 4.29:

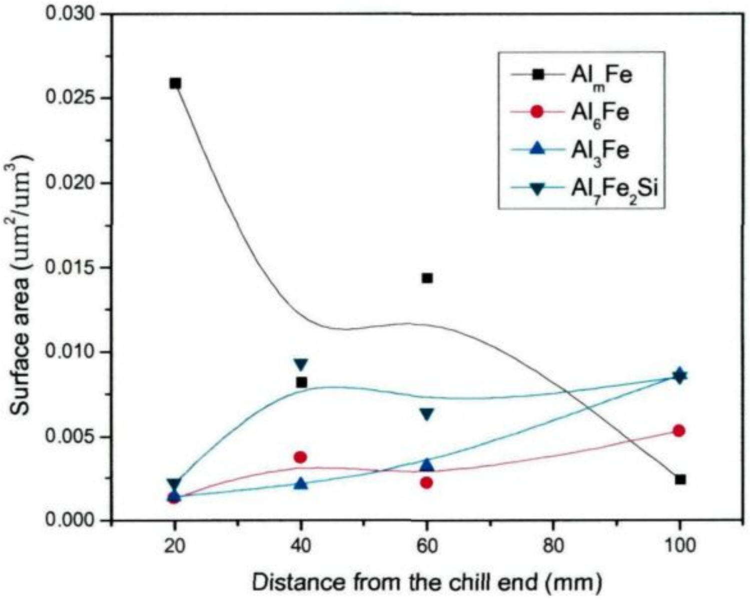

Figure 4.29: Surface area of each phase in A01 ingot.

When we compare Figure 4.28 and Figure 4.29 with Figure 4.27, we can find that the particle density and surface area of Fe phases have similar distribution tendency with the volume fraction, which means the particle number and surface area of Fe intermetallic phases have direct proportion to the volume fraction.

4.4 Effect of Ni on Fe intermetallic phases in DC simulator cast AA5657 ingots

For AA5657 alloy, which is an aluminium-magnesium based alloy, Ni is present as an impurity. It can not only cause accelerated corrosion, but also it has some effect on Fe intermetallic phases selection and give unwanted variation in anodizing response. In the recent years, the level of Ni content in the raw material and final products of Al is increasing. The continue trend of rising Ni may cause Al products not meet the specification. The present study is focused on the effect of Ni on Fe intermetallic phases selection in AA5657 alloy ingots produced by Lab DC simulator. Experimental alloys A05~A08 (Table 3.2), with different level of Ni content were casted and studied.

4.4.1 Ingots Microstructure

In the samples of ingots after Ni addition, high concentration of Ni was found in the interdendritic region of the ingots after Ni addition (Figure 4.30), which indicates that the addition of Ni was ejected to the rest liquid during the last stage of solidification.

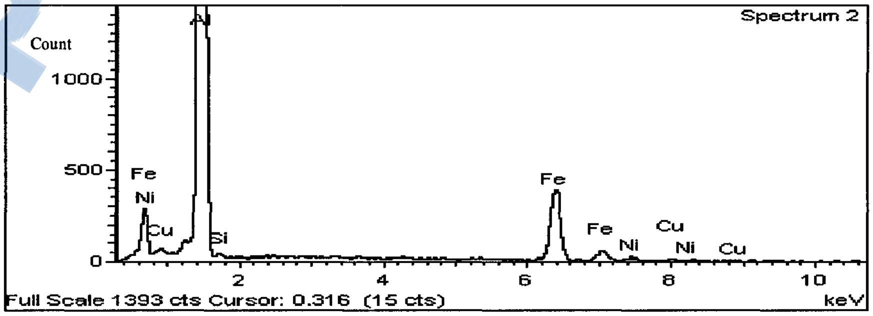

Figure 4.30: EDS shows the high content of Ni in the grain boundary after the addition of Ni in A10 ingot.

The enrichment of Ni in the interdendritic region may change the profile of the remaining liquid, which affect the nucleation and growth behavior of Fe intermetallic particles.

Figure 4.31 shows the Ingot microstructure of A05 (150 ppm Ni) to A08 (570 ppm Ni) with a same distance from the chill end.

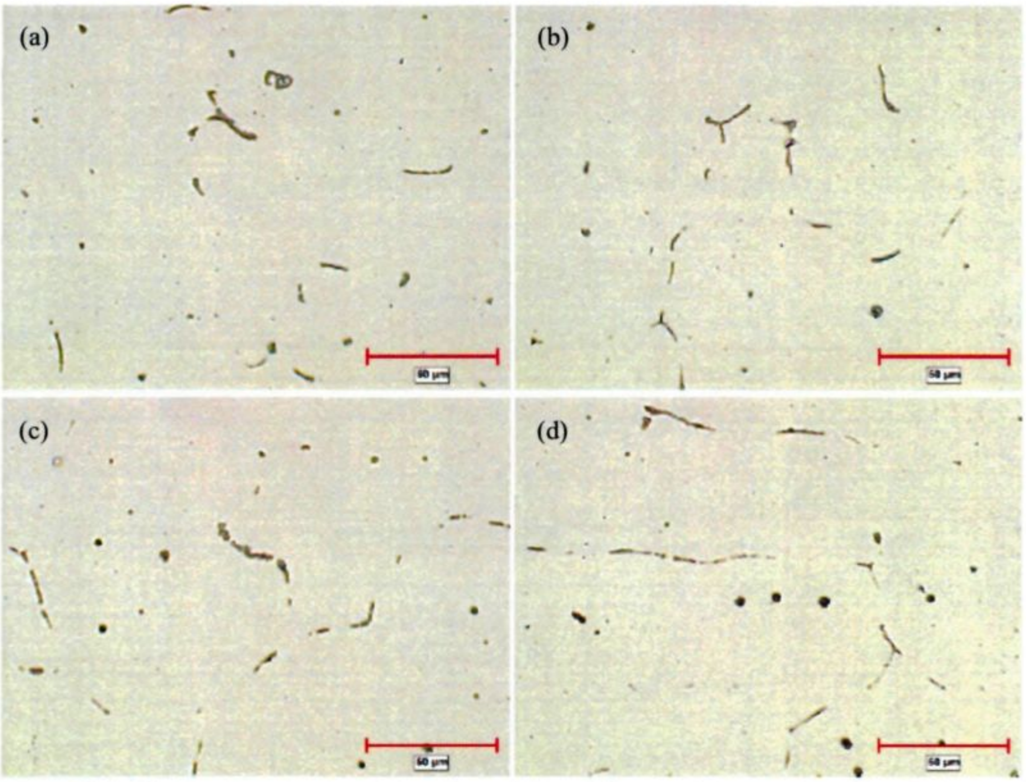

Figure 4.31: Photo microstructure taken from different Ni containing ingots with a distance of 40 mm from the chill ends. a) 150 ppm Ni, b) 240 ppm Ni, c) 390 ppm Ni, d) 570 ppm Ni.

It was found that low levels of Ni has no major effect on the ingots microstructure (Figure 4.31 (a) and (b)), while in the ingot with high Ni level over 390 ppm, some round particles seem appear and makes the microstructure different from others (Figure 4.31 (c) and (d).

The Fe intermetallic phases under SEM in A08 alloy and their corresponding EDS spectra are shown in Figure 4.32 and Figure 4.33:

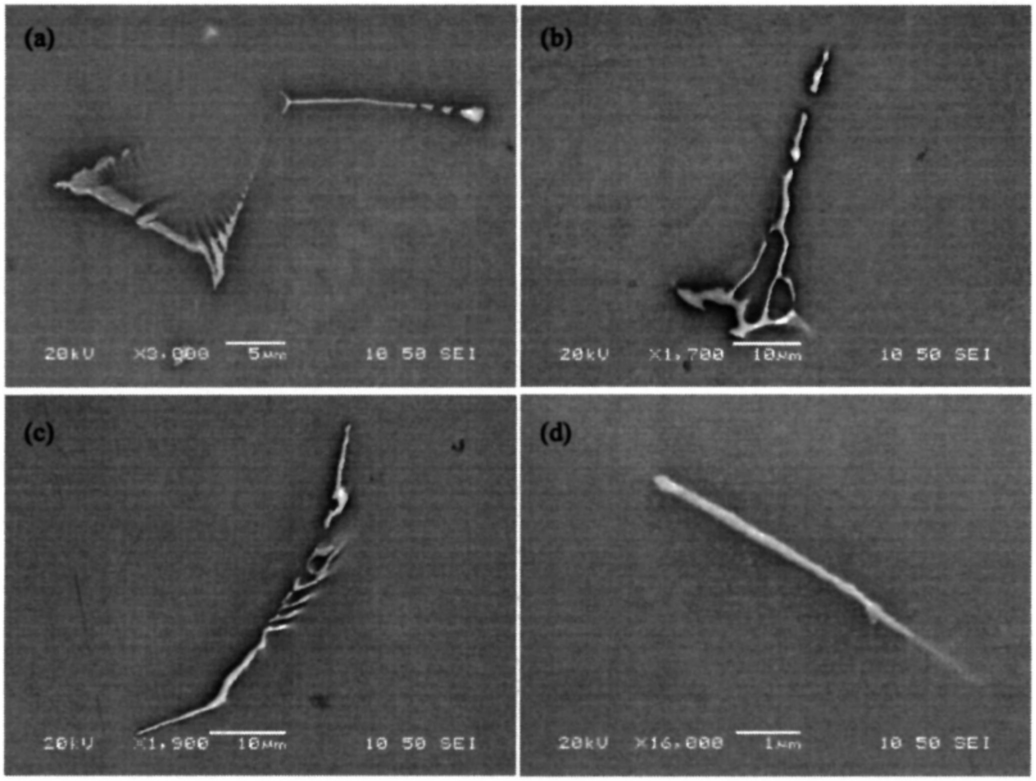

Figure 4.32: Fe intermetallic phases morphology under SEM in A08 alloy. (a) fine feathery like, (b) Chinese script, (c) curved plates with wings, (d) needle like.

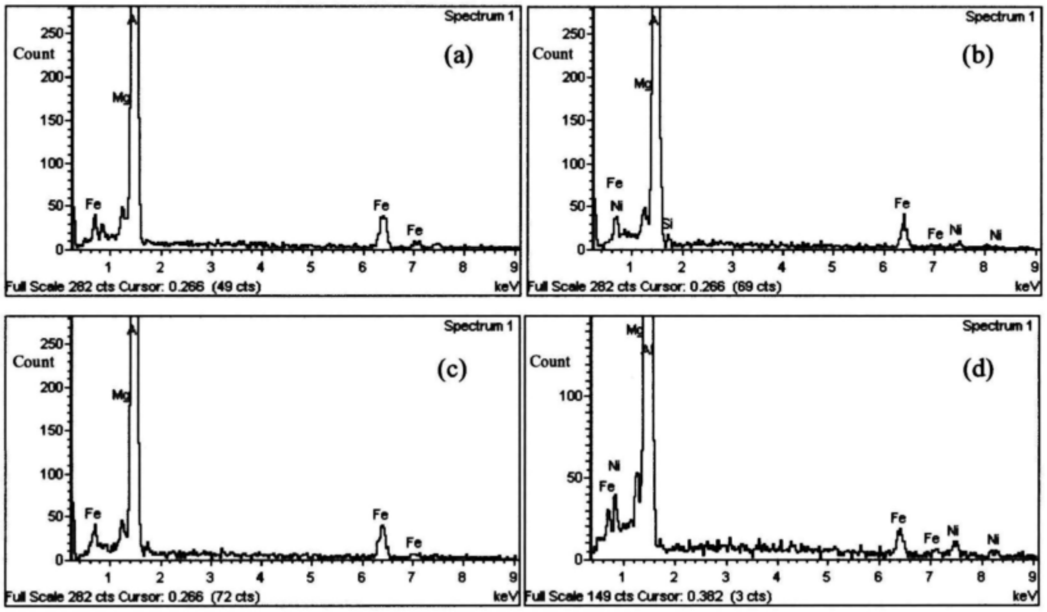

Figure 4.33: EDS spectra of Fe intermetallic particles in A08 alloy. (a) fine feathery like, (b) Chinese script, (c) curved plates with wings, (d) needle like.

In the ingot A07 and A08, some AlFeNi particles were observed frequently.

Figure 4.34 and Figure 4.35 shows the typical morphology and the EDS spectra of AlFeNi phase observed in an ingot with 570 ppm Ni content.

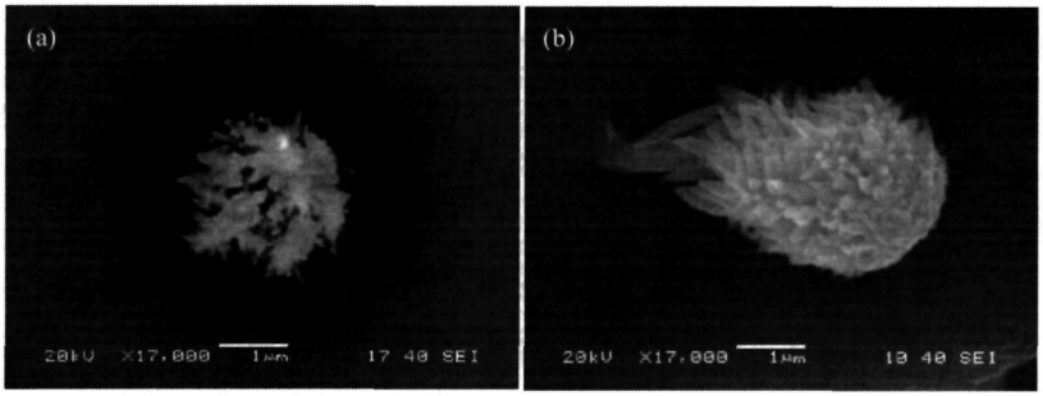

Figure 4.34: Typical morphology of AlFeNi in a DC simulator casting ingot under SEM. (a) Before Deep-etching, (b) After deep-etching.

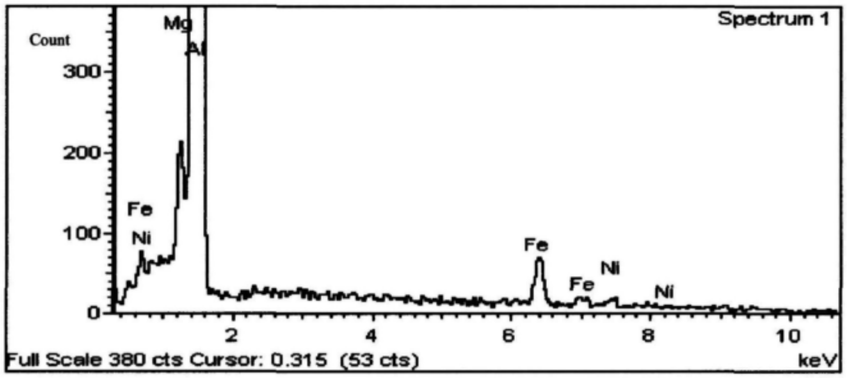

Figure 4.35: EDS spectra of AlFeNi in a DC simulator casting A08 ingot.

When refer to the findings of the AlFeNi particles in industry AA1050 alloy ingot, we can find that the AlFeNi particles in the lab DC simulator casting alloy ingots have similar characteristic with those observed in the AA1050 alloy ingot. Moreover, in some particles of Ni containing phases, white spots were frequently observed (Figure 4.36). The EDS results show that the ratio of Ni/Fe on the spots is about 3:2, which are much higher than other area of the particle (Figure 4.35). This phenomenon indicates that the high content of Ni is possible to be the cause of the white spots formation, which in turn promotes the formation of Ni containing phases.

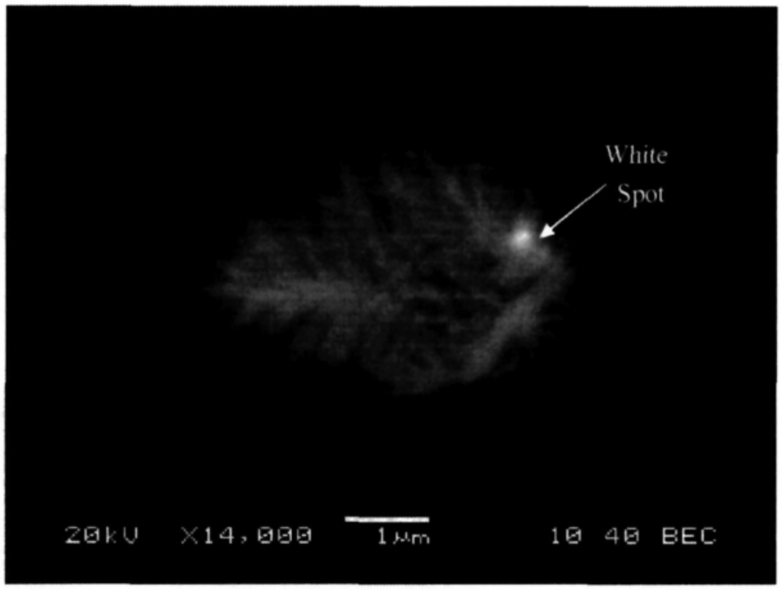

Figure 4.36: An AlFeNi particle under the SEM BEC mode, a white spot is clearly observed.

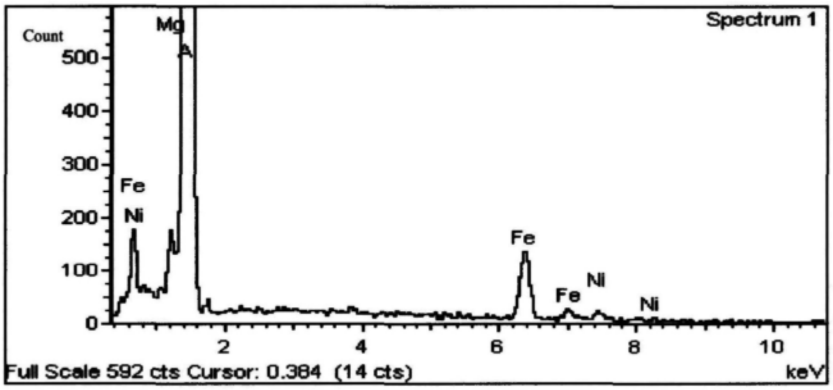

Figure 4.37: EDS shows high Ni content in the white spot of a AlFeNi particle.

The distribution of AlFeNi indicates the AlFeNi phase formation is affected by the cooling rates (Figure 4.38).

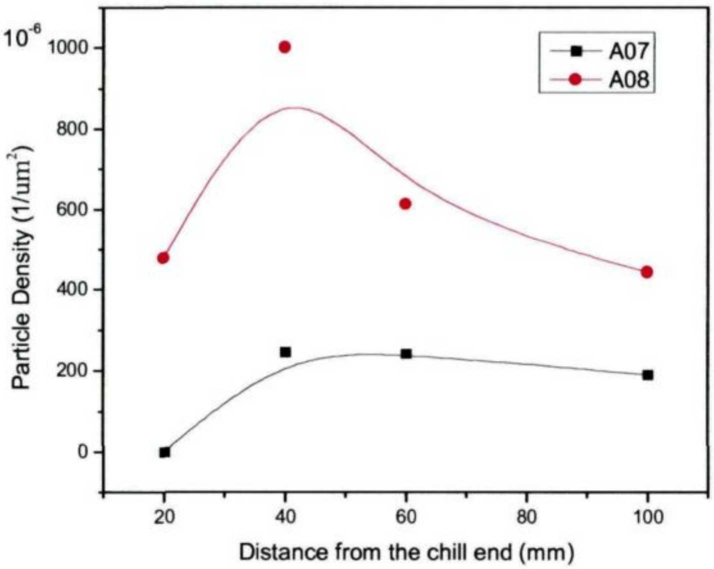

Figure 4.38: Distribution of AlFeNi particle density in A07, A08 alloy ingots.

As we can find, at the position 40 mm and 60 mm from the chill ends, the AlFeNi particle density appears the most. When refer to the average cooling rates in Figure 4.19, we can see the AlFeNi phase forms the most at the position with medium cooling rates.

4.4.2 EBSD patterns

Because of the smaller size of AlFeNi particles, it is impossible to get diffraction patterns based on the methods used in present study. Thus, the new Ni-containing phase was identified according their morphology and the EDS results. EBSD diffraction patterns of the four conventional phases were found similar with those in commercial AA5657 cast ingot, which were identified as Al_mFe, Al_7Fe_2Si, Al_6Fe and Al_3Fe. The following images show the diffraction patterns and their corresponding solutions of different intermetallic in A08 alloy got by EBSD. It was found that the feathery like morphology particles are mostly Al_mFe, chinese script particles are mostly Al_7Fe_2Si, curved plate particles are mostly Al_6Fe while needle like particles are mostly Al_3Fe.

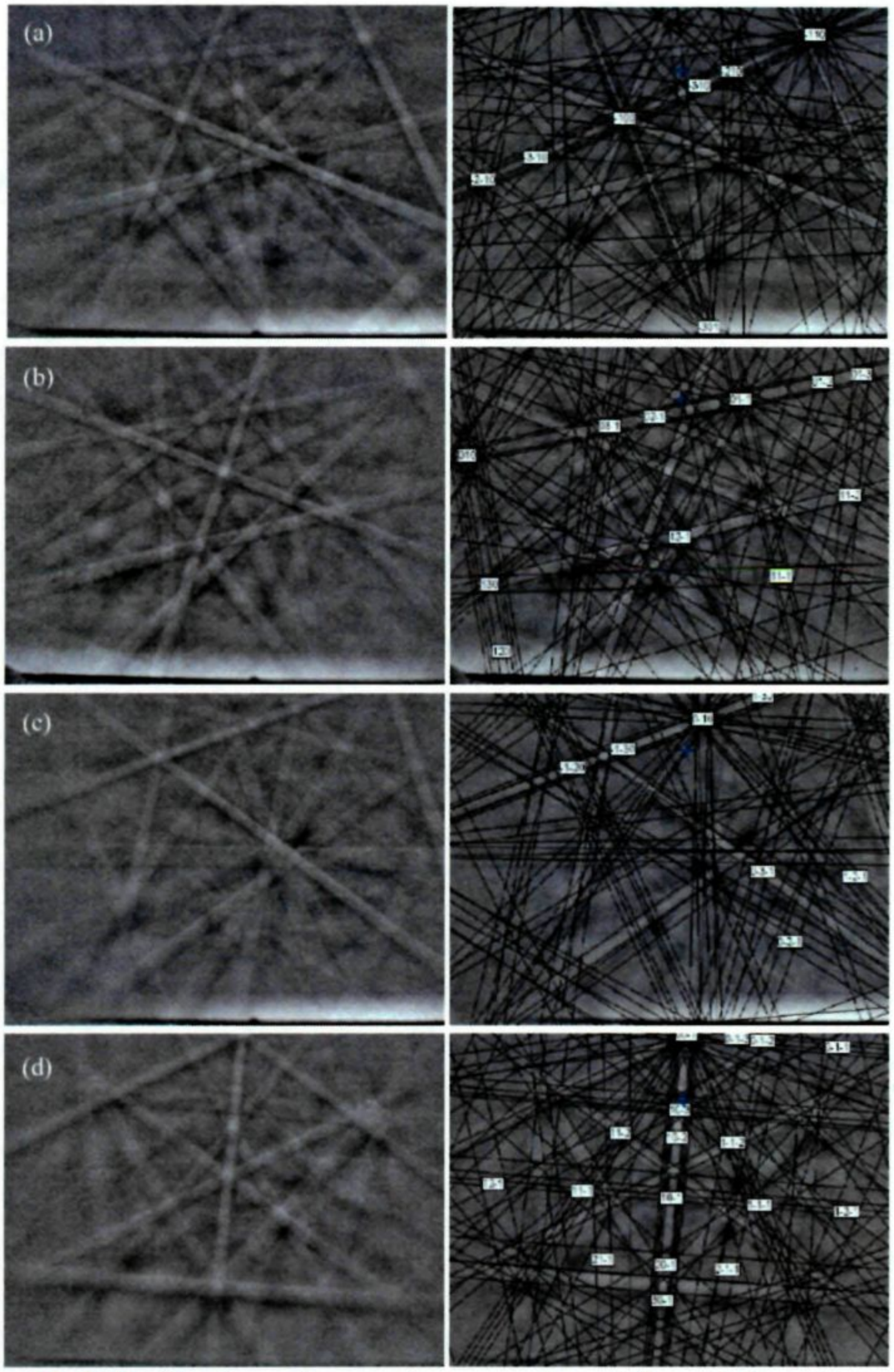

Figure 4.39:EBSD diffraction patterns and corresponding solutions of different type of Fe intermetallic phases in A08 alloy a) Al_mFe, b) Al_6Fe, c) Al_7Fe_2Si, d) Al_3Fe.

4.4.3 Image analysis results

The distribution of each Fe intermetallic phase in the ingots A01, A05~A08 is plotted in Figure 4.40:

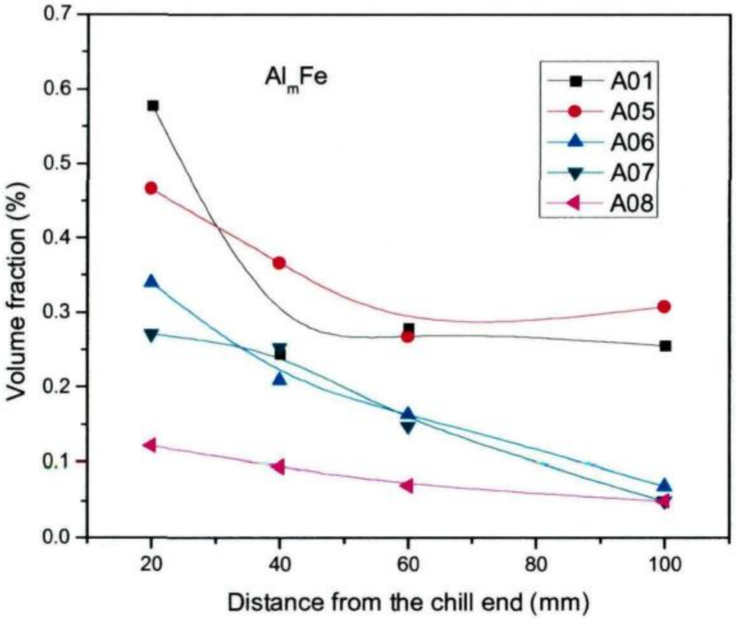

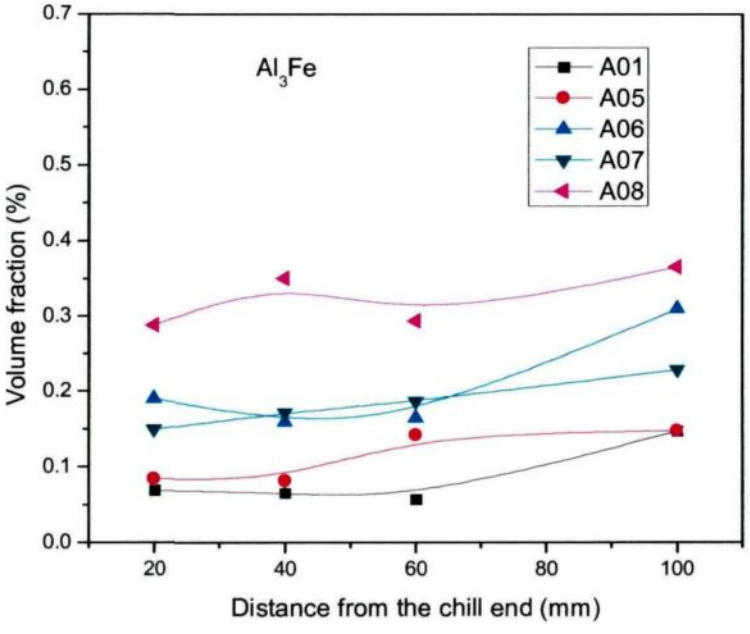

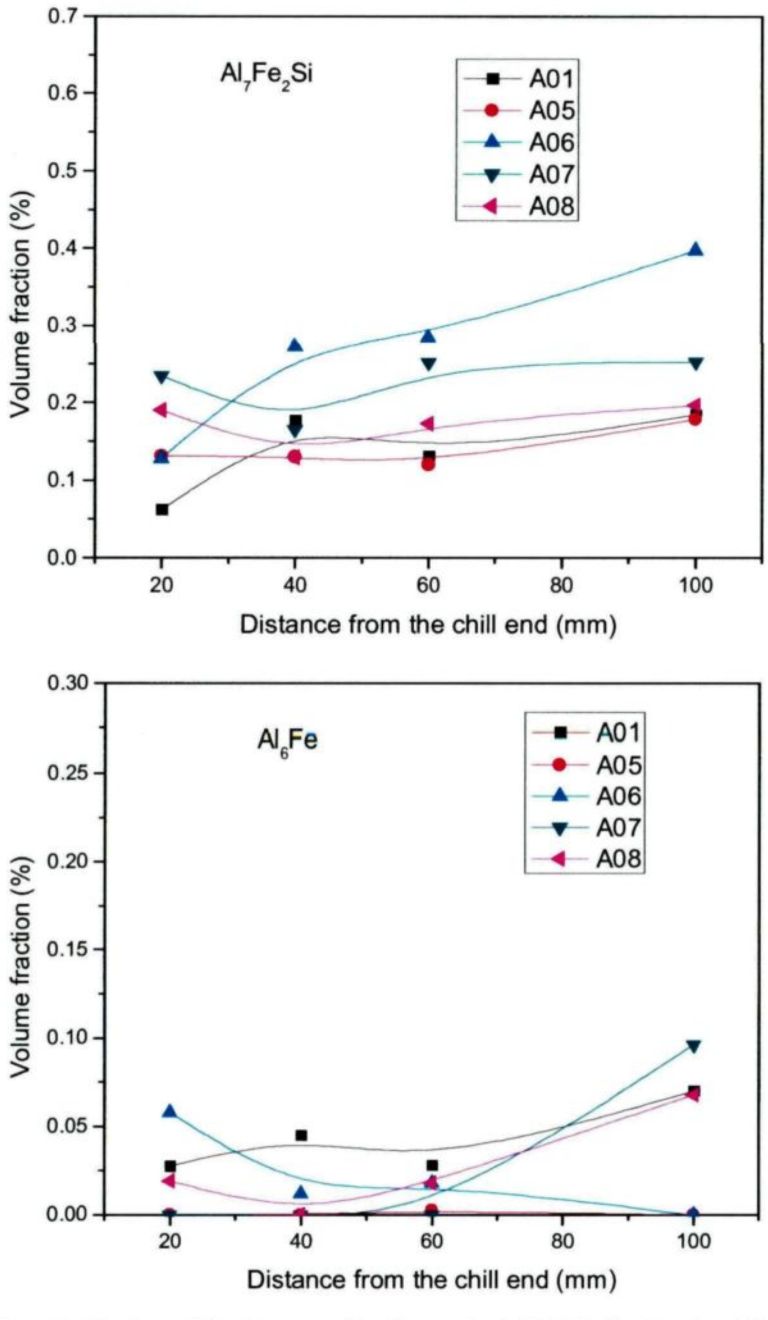

Figure 4.40: The distribution of Fe intermetallic phases in AA5657 alloy ingots with different Ni content. (a) Al_mFe, (b) Al_3Fe, c) Al_7Fe_2Si, d) Al_6Fe.

In Figure 4.40, we can find that the volume fraction of Al_mFe has a tendency to decrease with the Ni content in the ingot. On the contrary, Al_3Fe increase as the Ni level increase in the ingot. Al_7Fe_2Si has no major difference in these ingots. For Al_6Fe, it decreases obviously with the level of Ni content rising. In the low Ni content alloy

A01, Al_mFe is the predominant phase in the fast solidification region, while Al_3Fe and Al_6Fe are dominant in the low solidification region. The main effect of Ni addition is the promotion of Al_3Fe and makes Al_3Fe a dominant phase from the fast solidification region to low solidification region.

The addition of Ni can not only has impact on the quantity of each type of Fe intermetallic phases, but also has impact on total Fe intermetallic phases volume fraction. Figure 4.41 shows the total volume fraction of Fe intermetallic phases in A01 and A05~A08 ingots.

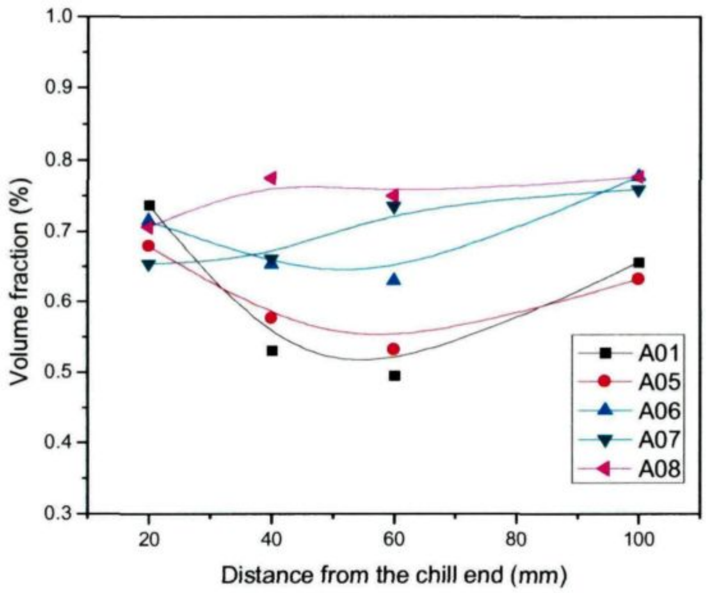

Figure 4.41: Total Fe phases volume fraction in the Ni containing ingots.

As we can see, the total Fe phases volume fraction has a tendency to increase with the Ni content increase, which indicates that the Ni addition may probably decrease the solid solubility of Fe, makes it segregate to the grain boundary and form secondary Fe intermetallic phases during DC casting process.

During solidification process, most of the Ni content was pushed towards the rest of the liquid where the Fe intermetallic phases nucleate and grow[12]. The fact that raising the level of Ni in AA5657 cast alloys promotes Al_3Fe over Al_6Fe and Al_mFe can be explained by the effect of Ni addition on competitive nucleation and competitive growth of phases.

(1) The impact on competitive nucleation

In previous researches, people have found that the impurities present in the alloy or grain refiner additions made during casting process may provide nucleation sites for phases. For example, Al_mFe was found by X.-G. Chen nucleates directly on TiB_2 and TiC particles in the sample with both AlTiB and AlTiC addition[12]. The findings by Hsu et al show that Ca promotes α-AlFeSi in 6xxx-series Al alloys through the formation of $CaAl_2Si_2$ during solidification[59]. The present study carried out in AA5657 cast alloy by using EDS shows that Al_3Fe particles usually contain some amount of Ni (See Figure 4.33), which indicates that the enriched Ni in the interdendritic regions may act as nucleation sites for Al_3Fe. In addition, for the faced eutectic Al_3Fe, it has the lowest branching ability among the four types of Fe intermetallic phases, and prefers a repeat nucleation rather than grow in a continuous way. The addition of Ni as potential nuclei for Al_3Fe makes the formation of Al_3Fe much easier than that of Al_mFe, Al_6Fe. Thus, it is much easier for Al_3Fe to form and growth even in the fast solidification region. The particle density of Al_3Fe was found increase with the level of Ni content increase in the ingots (Figure 4.42), which provides an efficient support for this proposal.

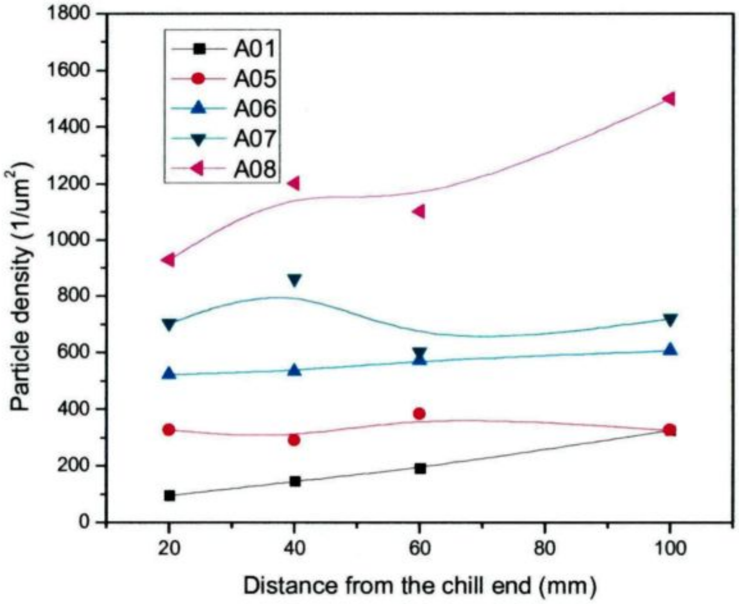

Figure 4.42: Effect of Ni on Al_3Fe particle density.

(2) The impact on competitive growth

For the unite cell of Al_3Fe, it has frequently been reported probably has tendency to twinning[60,61]. In C.M. Allen et al's work[59], they proposed that impurities may promote twinning, by providing a high density of edges and corners to which atoms can attach more easily, which in turn promote the growth of faceted eutectic Al_3Fe. This theory has good agreement with the present findings.

In conclusion, the increase of Ni in AA5657 alloy ingot promotes Al_3Fe and suppresses Al_mFe and Al_6Fe. Ni content over the amount of 390 ppm forms new Ni containing intermetallic phase.

4.5 Effect of V on Fe intermetallic phases in DC simulator cast AA5657 ingots

V is present in the primary aluminium metal as an impurity, at present, its typical concentration in commercial Al alloys ranges between 10 – 200 ppm[62]. In the recent years, the levels of element V is increasing quite fast in aluminium alloys and may exceed some plant specifications, because of the rising levels in the raw materials (Figure 4.43). Unlike the low solubility of Ni, at a concentration below 1000 ppm, the V-containing intermetallic phases are difficult to form due to the high solubility of V in aluminium[63]. While according to X. G. Chen's findings, an insoluble particles $(Ti,V)B_2$ form directly in the melt in the case of AlTiB grain refiner addition[12].

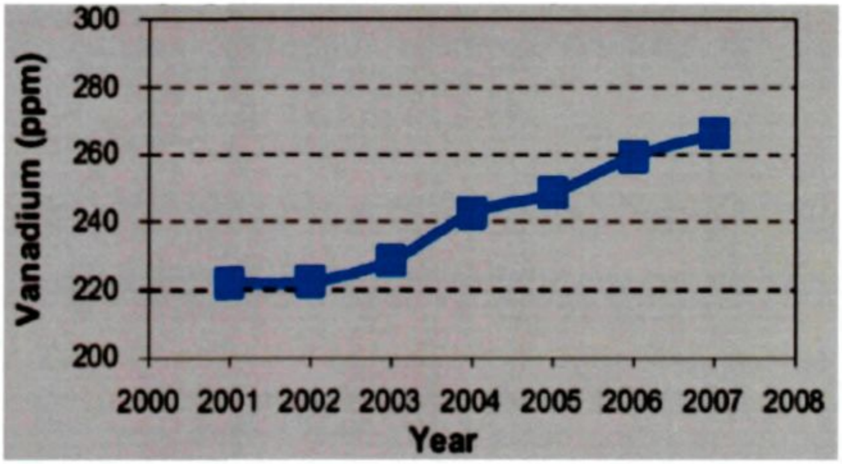

Figure 4.43: Increase in the vanadium content of coke over time[64].

V is known to raise the recrystallisation temperature and has some grain refining effect and to promote the formation of cubic α-AlFeSi in AlMgSi alloy as with Mn[62]. In addition, V was found to affect the Fe intermetallic phases selection and cause unwanted color variation on the anodized sheet[62]. In the present study, the goal is to make clear the effect of increasing V on Fe intermetallic selection in DC simulator

AA5657 cast ingots.

Three levels of V content ingots A02~A04 were cast (See Table 3.2), in which the V levels range from 240 ppm via 330 ppm to 480 ppm. Unlike the Ni addition ingots, V was not found concentrate on the interdendritic region due to its high solubility in Al matrix.

4.4.1 Ingots structure

Figure 4.44 shows the DC ingot structure taken from different V containing ingots with a distance of 40 mm from the chill ends.

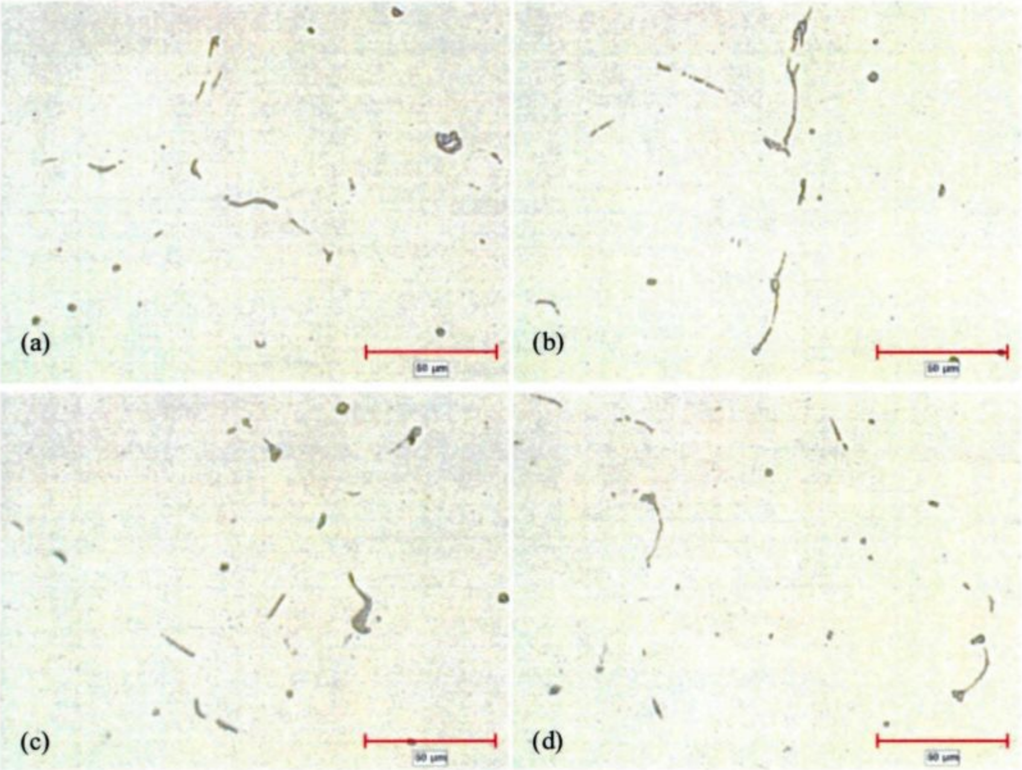

Figure 4.44: Photomicrograph taken from different V containing DC cast ingots with a distance of 40 mm from the chill ends. (a) 175 ppm V (A01), (b) 240 ppm V (A02), (c) 330 ppm V (A03), (d) 480 ppm V (A04).

From Figure 4.44, we can find most of intermetallic phase morphology in 2-D takes an interdendritic shape, which makes it difficult to be identified based on their morphology. The characteristics of each type of Fe intermetallic phases obtained by using SEM and EDS are shown in Figure 4.45 and Figure 4.46.

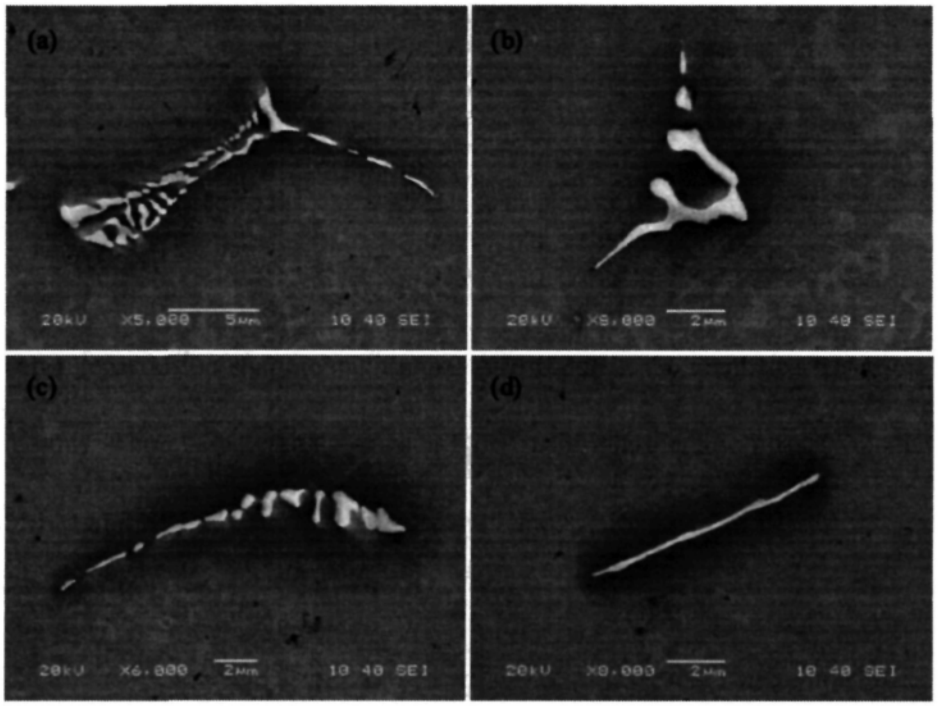

Figure 4.45: Fe intermetallic phases morphology under SEM in A04 alloy. (a) fine feathery like, (b) Chinese script, (c) curved plates with wings, (d) needle like.

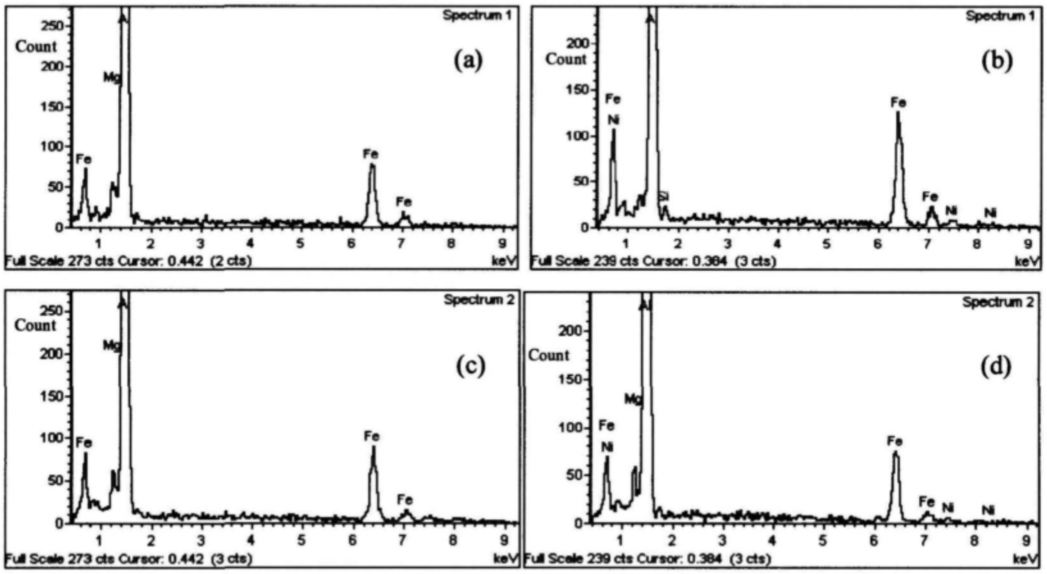

Figure 4.46: EDS spectra of Fe intermetallic particles in A04 alloy. (a) fine feathery like, (b) Chinese script, (c) curved plates with wings, (d) needle like.

From the results above, we can find that the typical morphologies, EDS results of the Al_mFe, Al_6Fe, Al_3Fe and Al_7Fe_2Si were similar with those in industry AA5657 cast ingot (see chapter 4.1).

4.5.2 EBSD patterns

EBSD diffraction patterns of the four conventional phases were found similar with those in commercial AA5657 cast ingot, which were identified as Al_mFe, Al_7Fe_2Si, Al_6Fe and Al_3Fe. The following images show the diffraction patterns and their corresponding solutions of different intermetallic got by EBSD. It was found that the feathery like morphology particles are mostly Al_mFe, chinese script particles are mostly Al_7Fe_2Si, curved plate particles are mostly Al_6Fe while needle like particles are mostly Al_3Fe.

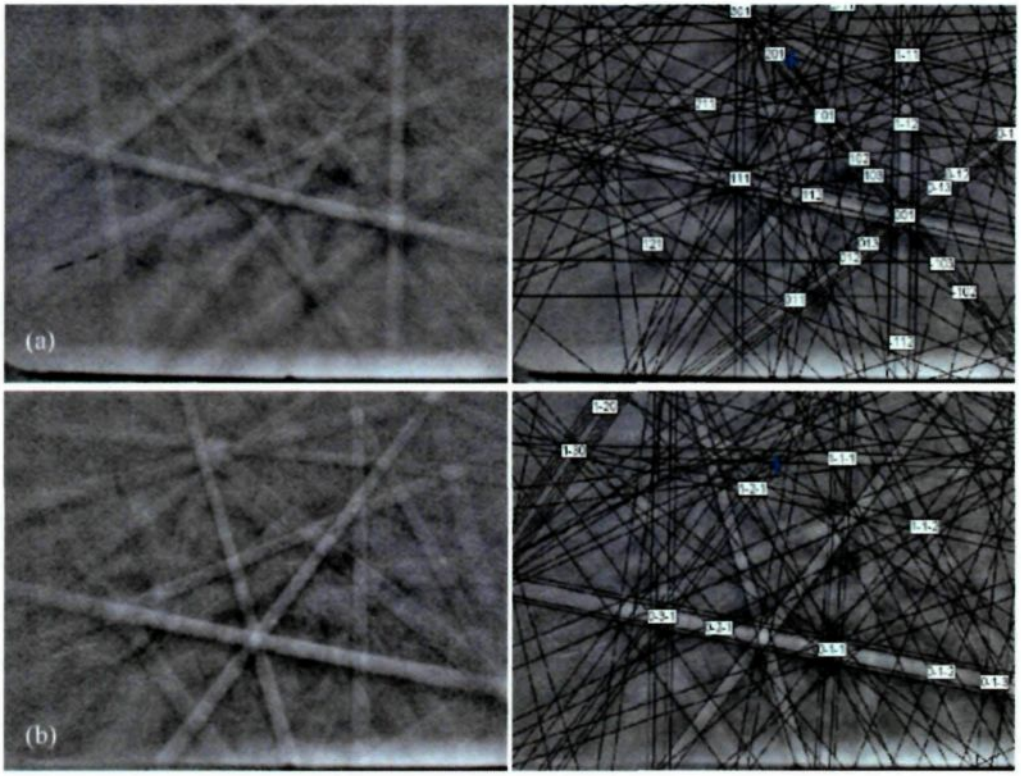

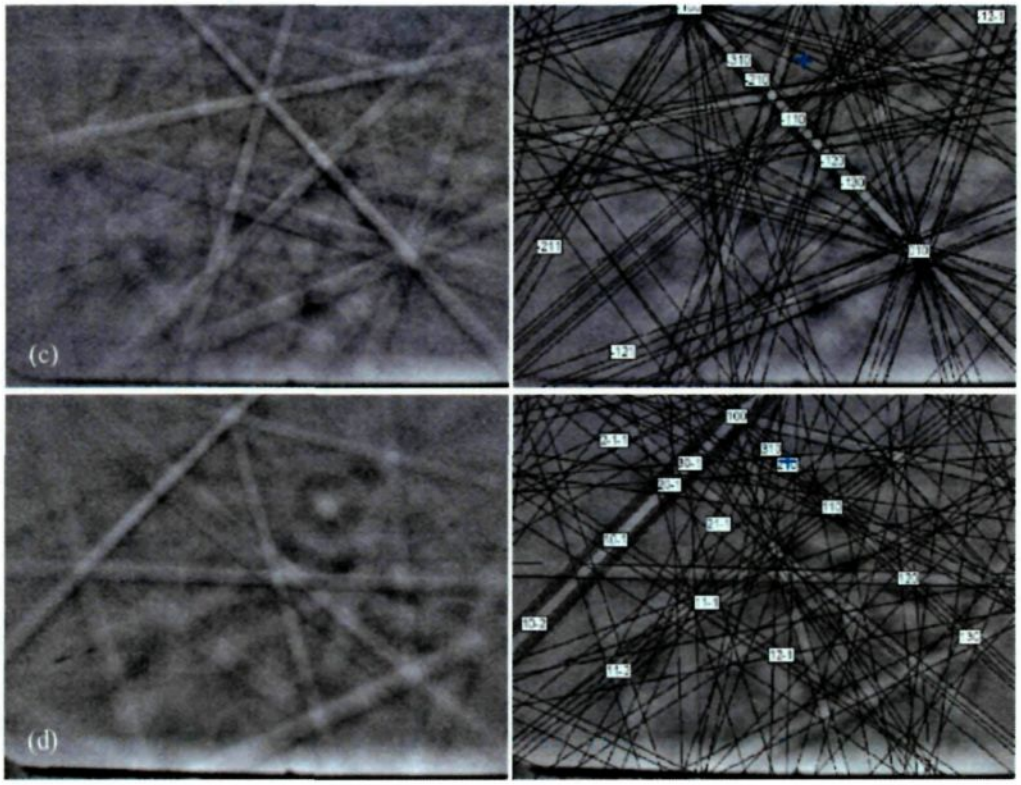

Figure 4.47: EBSD diffraction patterns and corresponding solutions of different type of Fe intermetallic phases in A04 alloy, a) Al_mFe, b) Al_6Fe, c) Al_7Fe_2Si, d) Al_3Fe.

4.5.3 Image analysis results

The distribution of each phase in the ingots A01 ~ A04 is listing in Figure 4.48:

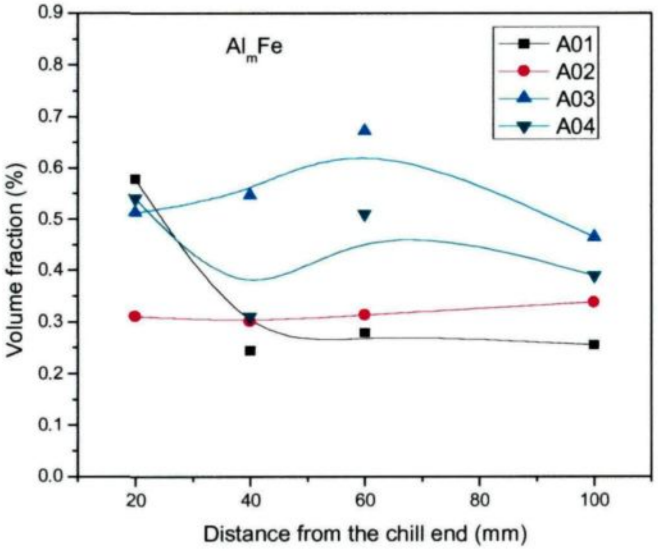

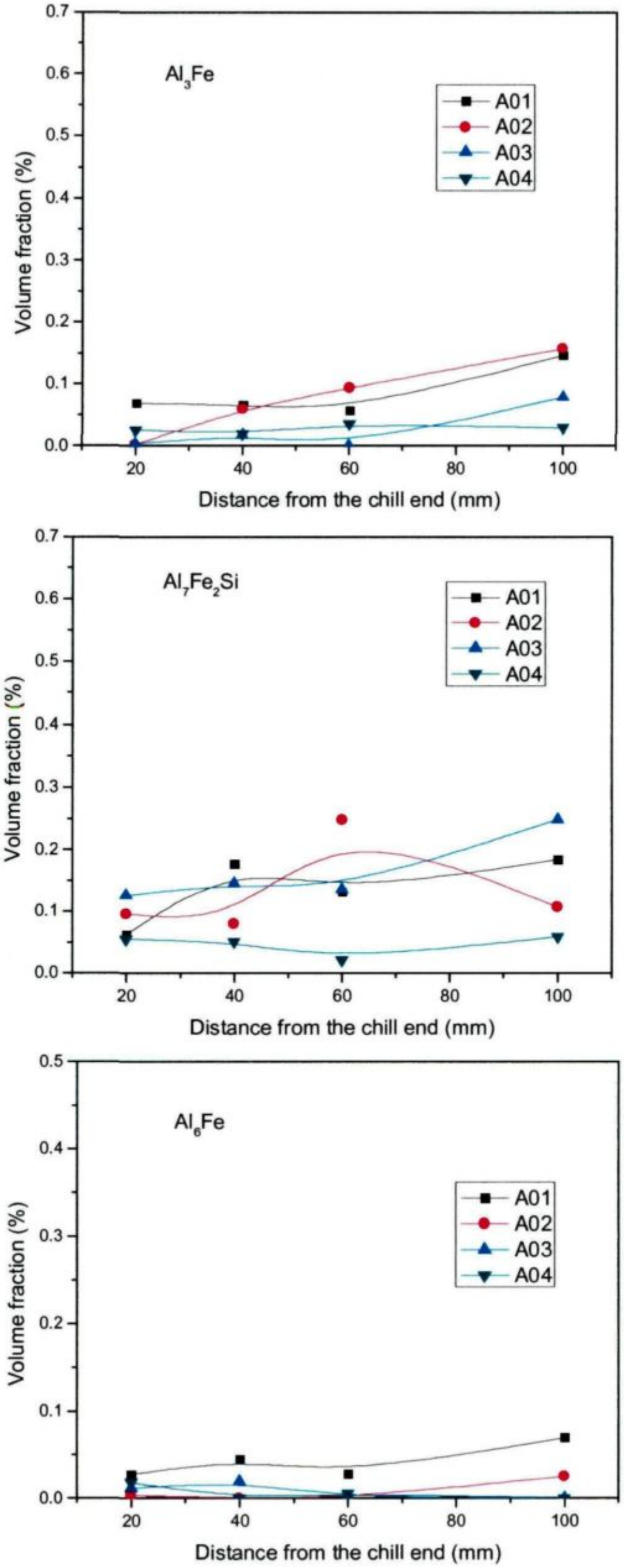

Figure 4.48: The distribution of Fe intermetallic phases in AA5657 alloy ingots with different levels of V content: (a) Al_mFe, (b) Al_3Fe, (c) Al_7Fe_2Si, (d) Al_6Fe.

In the figures above, we can clearly find that as the levels of V content in the AA5657 alloy ingot increase, Al_mFe has a tendency to increase in the location of the ingots with low cooling rates (Figure 4.48 (a)). On the contrary, the amount of Al_3Fe, Al_6Fe and Al_7Fe_2Si has a tendency to decrease with the increasing levels of V in these ingots (Figure 4.48 (b-d)). These findings suggest that V can promote the formation of Al_mFe and makes it grow easier in the low cooling rate region, while it suppress the formation of Al_3Fe, Al_6Fe and Al_7Fe_2Si.

The total volume fraction of Fe intermetallic phases in the V containing ingots is shown in Figure 4.49:

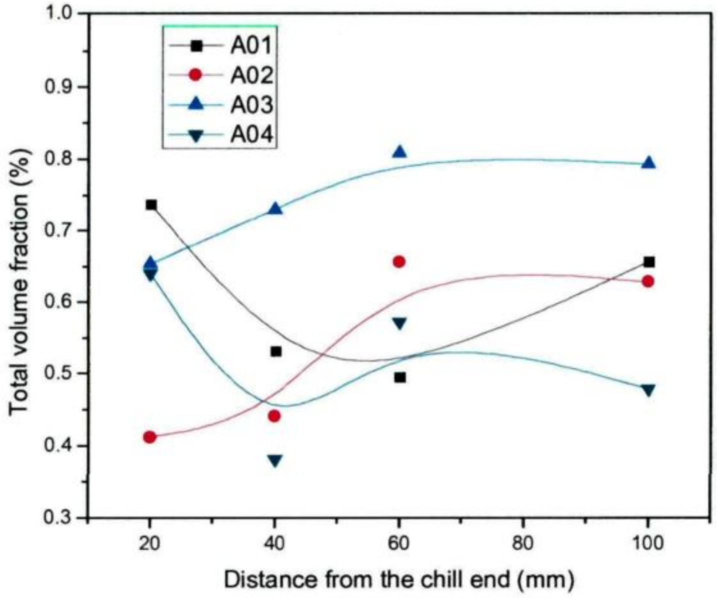

Figure 4.49: Total Fe phases volume fraction in the V containing ingots.

As we can see, unlike the effect of Ni on total Fe intermetallic phases volume fraction, the change of total Fe phases volume fraction after V addition is not uniform.

In order to understand the effect of trace element V on the phase selection in AA5657 alloy, it is necessary to consider both nucleation and growth aspects. It was proposed in the previous research that under the condition of Al-Ti-B grain refinement addition, the addition of trace element V probably forms an insoluble particles $(Ti,V)B_2$ directly in the melt during solidification process[12]. As the solidification proceeds, these insoluble particles are pushed towards the rest of the interdendritic liquid, where the Fe intermetallic phases nucleate and grow. The enrichment of V particles may leads to the local solidification behavior change. Two possible mechanisms can be employed to explain the promotion of Al_mFe over other intermetallic phases:

(1) Nucleation of insoluble V containing particles. In the AA5657 alloy used in present study, AlTiB or AlTiC was added during the industry DC casting process as grain refiner, some amount of Ti was found present in the AA5657 alloy (See Table 3.1). The Al_mFe was found nucleate directly on TiB_2 and TiC particles in X.-G Chen's research[12]. The addition of V in the DC simulator cast ingots forms an insoluble particles $(Ti,V)B_2$ which may act as efficient nuclei for Al_mFe. The Al_mFe particles form at higher cooling rates than the other phases, because it has the lowest eutectic temperature than Al_6Fe, Al_3Fe and α-AlFeSi. The exits of insoluble particles may lower the critical cooling rate and raise the nucleation temperature for Al_mFe. The element V can change the nucleation temperature of Fe intermetallic phases in Al alloy has been proved in CM. Allen et al's research (Figure 4.50)[65].

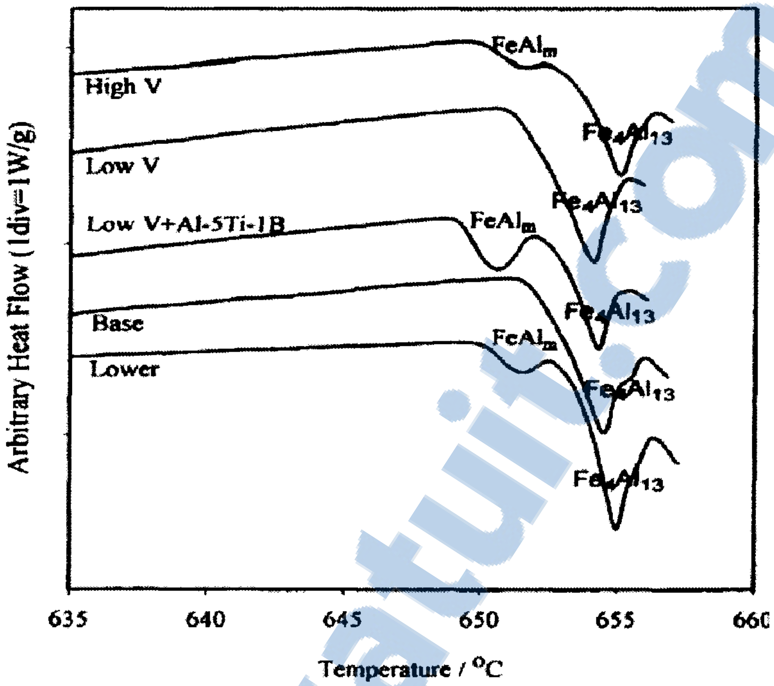

Figure 4.50: Entrained droplet melting differential scanning calorimeter traces from Ixxx series aluminium alloys with a high purity base, a low purity base, high purity base plus high and low levels of vanadium, and high purity base with a combination of low vanadium and grain refiner addition[65].

In Figure 4.50, the peaks represent the melting of aluminium-intermetallic eutectics. In a low purity material, two peaks are observed, representing the melting of the equilibrium Al-Fe_4Al_{13} eutectic and the metastable Al-$FeAl_m$ eutectic. The high purity base material only contains the equilibrium Al-Fe_4Al_{13} eutectic. Additions to this base material of a combination of low levels of vanadium with Al-Ti-B grain refiner, lead to the formation of the metastable Al-$FeAl_m$ eutectic, while the addition of high levels of vanadium, lead to the increase of Al-$FeAl_m$ eutectic melting temperature (nucleation temperature) increase. In the present study, the AA5657 alloy was grain refined by Al-5Ti-B refiner, the addition of V may have similar effect on the Al_mFe eutectic melting temperature.

Let us take Al_mFe/Al_3Fe for example to explain how the raising level of V promotes Al_mFe formation over other Fe intermetallic phases. As indicated in Figure 4.51, the nucleation temperature for Al_mFe T_2 and Al_3Fe T_1, $T_2 < T_1$, the cooling rate $Tc_2 < Tc_1$, the addition of V raising the nucleation temperature of Al_mFe (the dotted line in the figure) while keep the nucleation temperature of Al_3Fe the same, this effect obviously lower the critical cooling rates from Tc_1 to Tc_2, which makes it easier for Al_mFe to form at lower cooling conditions.

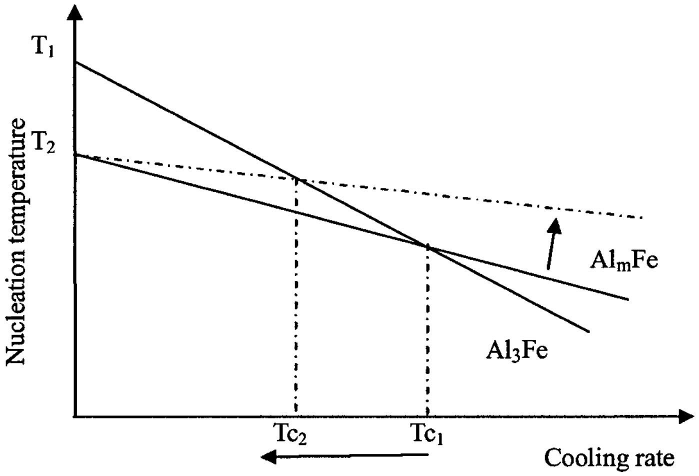

Figure 4.51: Schematic illustration of the formation of V containing particles act as preferential nucleation sites of AlmFe, raising the nucleation temperature and lower the critical cooling rate Tc for Al_mFe formation.

(2) Impact on the growth behavior. S.J.Maggs[13] proposed in his study that the elements segregated into the remaining liquid in the solidification process tend to have big effect on the intermetallic phases even at very low trace level. For the intermetallic phase that grows in a faceted mode by step-wise growth rather than in a non-faceted continuous manner, the trace element could poison the site where the intermetallic particles attach the liquid, which can cause significant decrease in the growth temperature, and caused it lose out to another phase. Thus, faceted phase

Al_3Fe lose out to the non-faceted phase Al_mFe in AA5657 alloy ingot after the V addition.

Recently, some researchers have found that the solidification velocity other than cooling rate is the more fundamental parameter that effects the Fe intermetallic phases selection[59], it was found that Al_mFe forms in the growth condition with the fastest growth velocity, then are the phases α-AlFeSi and Al_6Fe. Al_3Fe forms at the lowest growth velocity condition. According to Dong, Liang and Howard, Jones[66], the growth temperature, T_g, with the solidification velocity, U, fit the form:

$$T_g = T_{EU} - BU^{1/2}$$

Where T_{EU} is the equilibrium solidification temperature (i.e. $T_{EU} = T_g$ at $U = 0$) and B is a constant varies from eutectic to eutectic. In the last stage of solidification, the intermetallic has to grow in an intergranular liquid, which has less space and complex shape. Thus, frequent branching ability is needed for a certain phase growth. Among the four intermetallic phases observed in AA5657 alloy ingot, Al_mFe mostly adopt a fine feathery morphology and has the branching ability than others[4]. So the Al_mFe has the most favorable condition to growth in this alloy ingot. Similarly, we will take Al_mFe/Al_3Fe for example to explain the promotion of V on Al_mFe over other phases. As shown in Figure 4.52, the growth temperature of Al_3Fe T_1 and Al_mFe T_2, $T_1 > T_2$, the solidification velocity $V_1 > V_2$. The main function of the grain refiner addition is change the primary aluminium structure from columnar to equiaxed. Moreover, the effect of grain refiner can be enhanced in the combination of some alloying and trace elements. The addition of V in the DC cast alloy makes the aluminium further refined, which makes the growth condition for Al_3Fe more unfavorable due to its step-wise growth manner. This, in turn, leads to the growth temperature of Al_3Fe decrease (the dotted line in the figure), Thus, the range of growth velocity for Al_mFe is extend from V_1 to V_2, and make the Al_mFe to grow in the low growth velocity region.

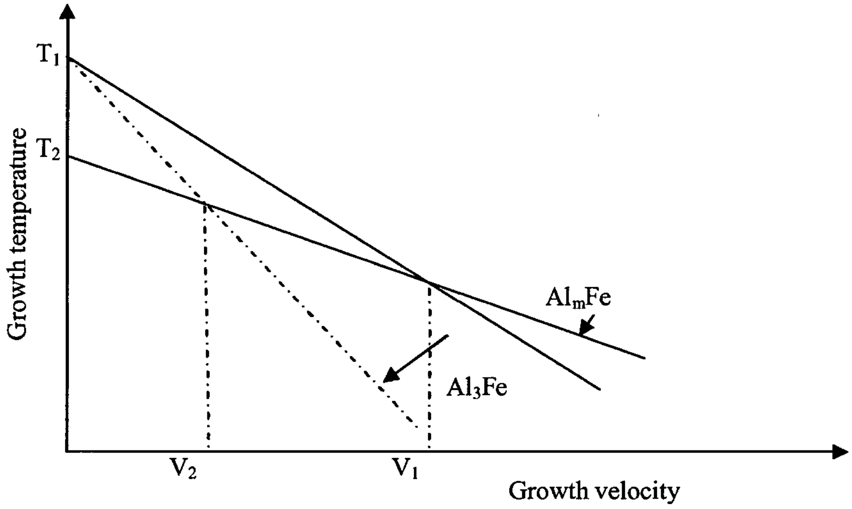

Figure 4.52: Schematic illustration of the V addition decrease the growth temperature of Al_3Fe, lower the critical growth velocity for Al_mFe.

In conclusion, the effect of rising levels of V in AA5657 alloy ingot can heavily promote Al_mFe and suppress Al_3Fe, Al_6Fe, and Al_7Fe_2Si.

4.6 Effect of The combined addition of V and Ni on Fe intermetallic phases in DC simulator cast AA5657 ingots

In chapter 4.4 and 4.5, the effect of Ni or V is investigated in the lab. However, the levels of Ni and V could rise simultaneously in industry practice. Thus, it is quite necessary to understand the combined effect of Ni and V on Fe intermetallic phases. In the present research, two ingots A09, A10 were casted using the DC simulator with different amount of Ni and V addition simultaneously (See Table 3.2).

4.6.1 Ingots Microstructure

Figure 4.53 shows the DC ingot structure taken from different A01, A09 (260 ppm V and 240 ppm Ni) and A10 (380 ppm V and 250 ppm Ni) ingots.

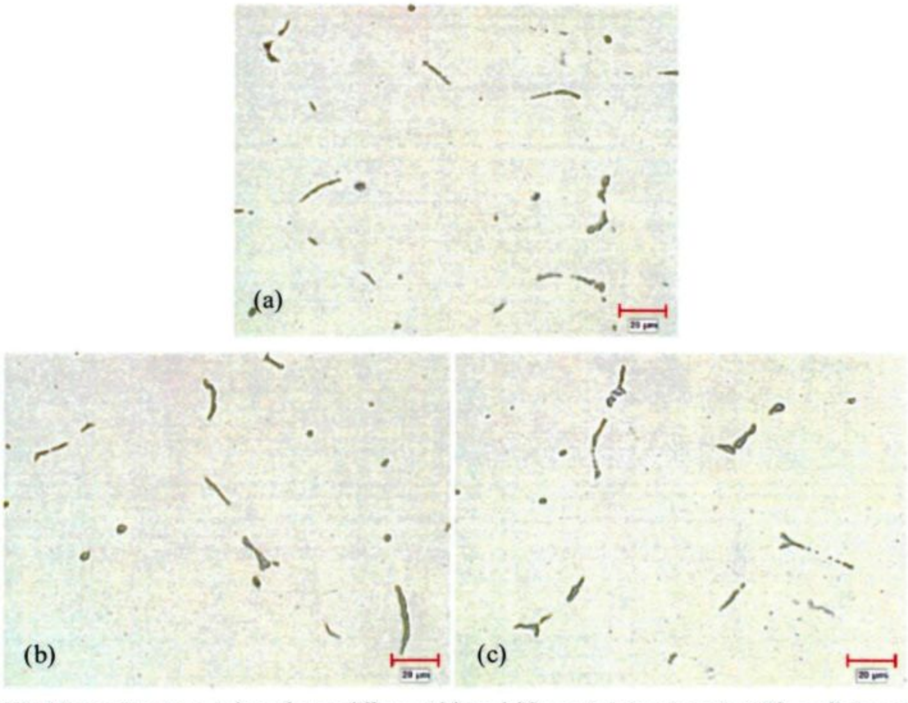

Figure 4.53: Microstructure taken from different V and Ni containing ingots with a distance of 40 mm from the chill ends. a) A01, b) A09, c) A10.

From the figures above, we can find that the 2-D morphology of intermetallic phases always appear interdendritic shape, there is no obvious change in the ingots microstructure with the V and Ni addition simultaneously. Further study of these intermetallic phases using SEM and EDS was carried out. The results are shown in Figure 4.54 and Figure 4.55.

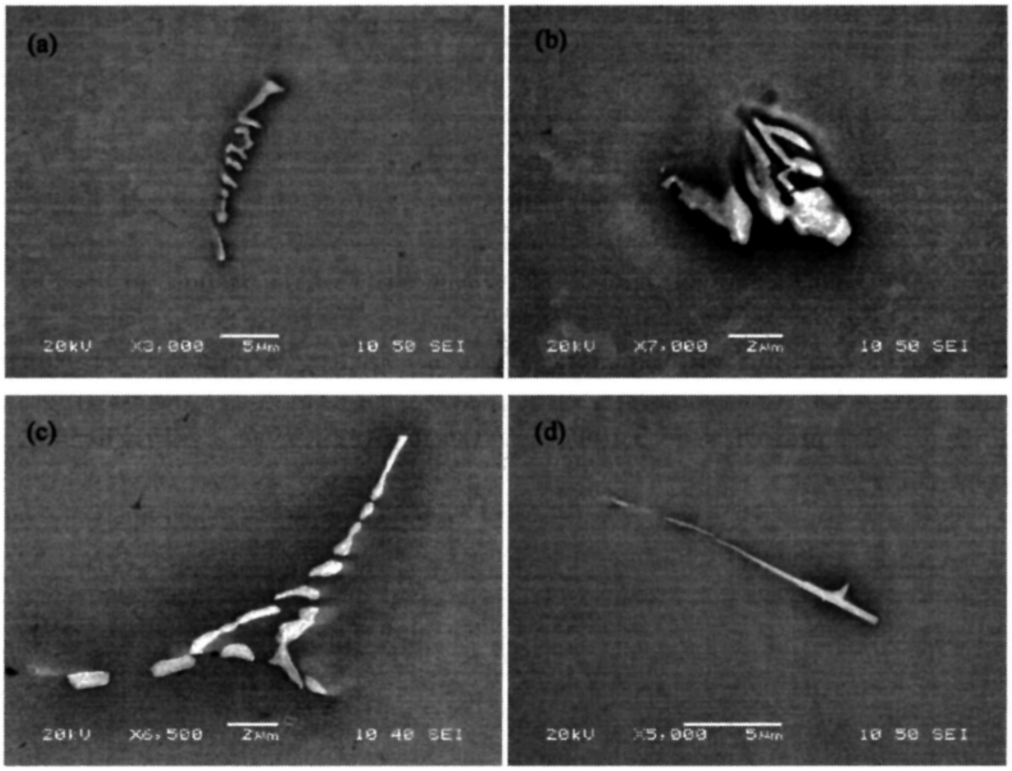

Figure 4.54: Fe intermetallic phases morphology under SEM in A10 alloy. (a) fine feathery like, (b) Chinese script, (c) curved plates with wings, (d) needle like.

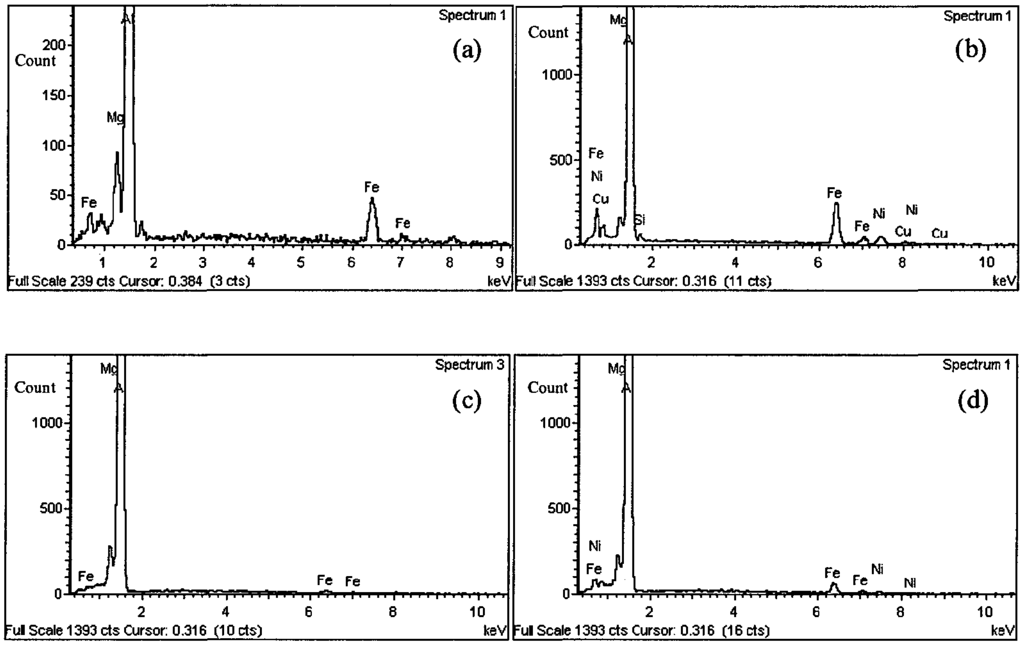

Figure 4.55: EDS spectra of Fe intermetallic phases in A10 alloy. (a) fine feathery like Al$_m$Fe, (b) Chinese script Al$_7$Fe$_2$Si, (c) curved plates with wings Al$_6$Fe, (d) needle like Al$_3$Fe.

Form the results above, we can find that the typical morphologies, EDS results of the Al$_m$Fe, Al$_6$Fe, Al$_3$Fe and Al$_7$Fe$_2$Si were similar with those in industry AA5657 cast ingot (see chapter 4.1).

4.2.2 EBSD patterns

The following images show the diffraction patterns and their corresponding solutions of different intermetallic got by EBSD. EBSD diffraction patterns of the four conventional phases in the V and Ni containing ingots were found similar with those in commercial AA5657 cast ingot, which were identified as Al$_m$Fe, Al$_7$Fe$_2$Si, Al$_6$Fe and Al$_3$Fe.

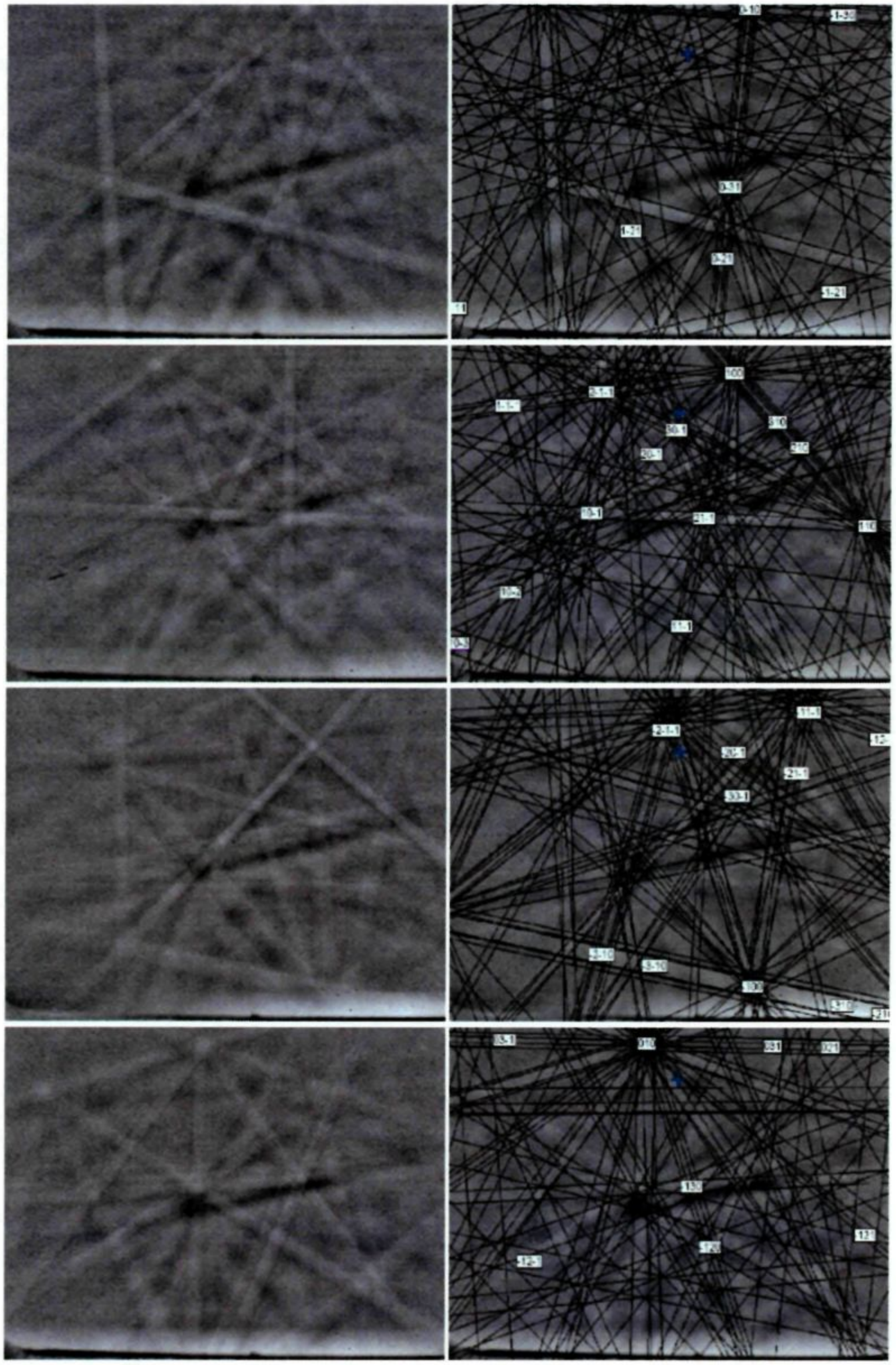

Figure 4.56: EBSD diffraction patterns and corresponding solutions of different type of Fe intermetallic phases in V containing ingots, a) Al_mFe, b) Al_6Fe, c) Al_7Fe_2Si, d) Al_3Fe.

4.6.3 Image analysis results

The distribution of each phase in A09 and A10 compared with that in A01 is shown in Figure 4.57:

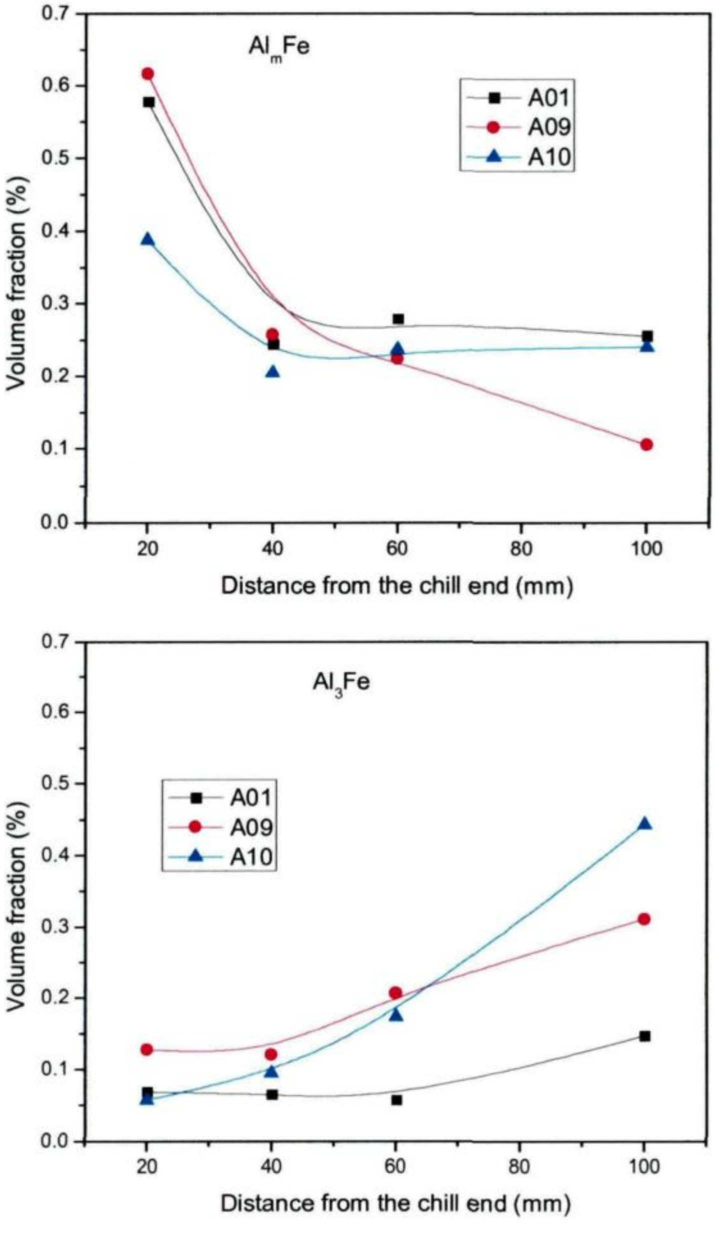

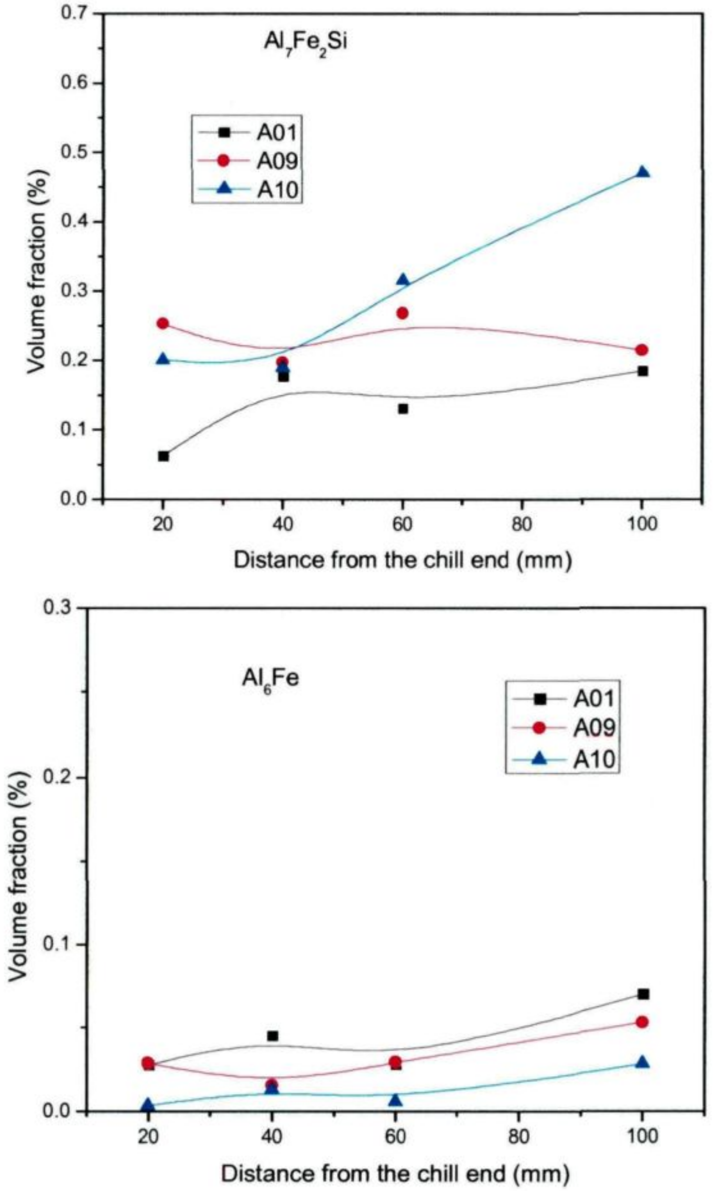

Figure 4.57: The distribution of Fe intermetallic phases in AA5657 alloy ingots with different levels of V and Ni content. a) Al_mFe, b) Al_3Fe, c) Al_7Fe_2Si, d) Al_6Fe.

From Figure 4.57, we can found that after the addition of V and Ni, the volume fraction of Al_7Fe_2Si and Al_3Fe increase, while the volume fraction of Al_6Fe decreases. There is no major effect of V and Ni addition on Al_mFe.

The total Fe intermetallic phases volume fraction in the ingots A01, A09 and A10 is shown in Figure 4.58:

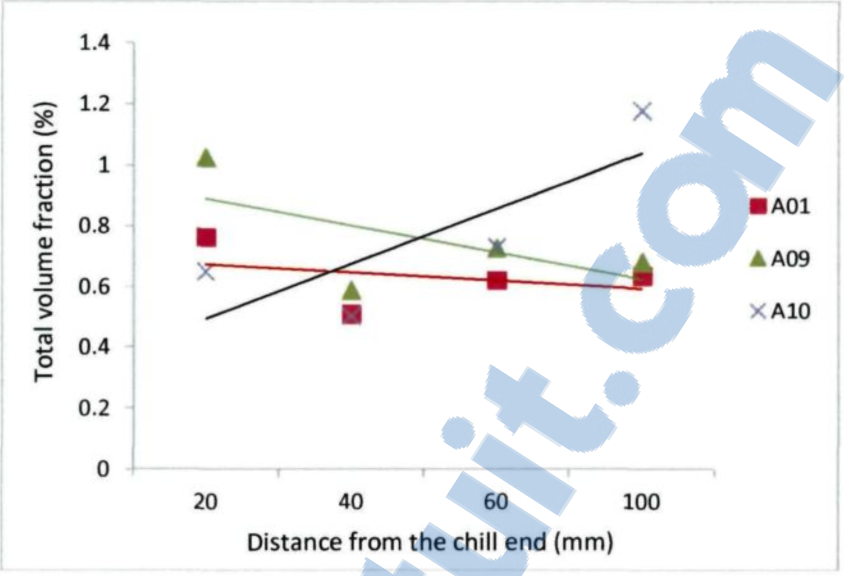

Figure 4.58: Effect of V and Ni on total Fe intermetallic phases volume fraction.

As we can see in Figure 4.58, there is no uniform tendency of total Fe intermetallic phases volume fraction when V an Ni are added simultaneously.

Although it is quite complicated to understand the combined effect of V and Ni on Fe intermetallic phases, we can try to explain some of the phenomenon by using the theory used in previous study. When refer to the previous findings, in which we find V can promote Al_mFe and Ni can promote Al_3Fe, when the level of V and Ni increase simultaneously in the DC casting ingot, the reverse effect of V and Ni on Al_mFe counteract their effect on Al_mFe, so it appears no big changes on the volume fraction of Al_mFe. The promotion of V and Ni addition on Al_3Fe reflect the effect of Ni on the Fe intermetallic phases, which indicates that Ni has advantage over V to show the effect on the Fe intermetallic phases in the ingots A09 and A10 used in this study. The mechanism of the effect that raising the level of V and Ni simultaneously promotes Al_7Fe_2Si over Al_6Fe is still not clear.

Chapter 5 Conclusions and Suggestions for further work

5.1 Conclusions

1. Using a DC simulator, the solidification conditions in the sub-surface region of commercial DC cast ingots were successfully reproduced at the lab scale.

2. The transition of Al_mFe, Al_6Fe, Al_3Fe and Al_7Fe_2Si intermetallic phases were observed in both commercial and lab DC simulator casting AA5657 alloy ingots, but no visible FTZs were revealed as opposed to AA1050 alloy. The typical deep-etching morphology of Al_mFe, Al_6Fe, Al_3Fe and Al_7Fe_2Si were revealed by using deep-etching method.

3. Al_mFe, Al_6Fe, Al_7Fe_2Si and Al_3Fe intermetallic phases in DC cast Al ingots were successfully identified by using SEM, EDS and EBSD technique in combination.

4. A slice of AA1050 alloy ingot with a visible FTZ was studied. It was found Al_mFe, Al_6Fe, Al_3Fe, Al_7Fe_2Si and a Ni containing intermetallic phases distribute across the FTZs. The quantitative analysis results of the Fe intermetallic phases show that the transition between Al_mFe and Al_6Fe is the main reason that causes the FTZs visible.

5. Raising the level of the trace element Ni promotes Al_3Fe in the whole ingot, suppress Al_mFe and Al_6Fe. High levels of Ni content more than 390 ppm promote the formation of a new Ni-containing intermetallic phase;

6. Increasing the level of the trace element V in AA5657 alloy heavily promotes Al_mFe and suppresses Al_3Fe, Al_6Fe, Al_7Fe_2Si.

7. Increasing the level of the trace elements V and Ni simultaneously suppress Al_6Fe and promote α-AlFeSi and Al_3Fe;

8. The mechanism of the effect of trace elements V or/and Ni on Fe intermetallic phases selection is relate to the fact that the trace element impurities can affect the nucleation and growth behavior of certain phases.

5.2 Suggestions for further work

This study concentrated on the Fe intermetallic phases characterization and the effect of trace element V or/and Ni on the Fe intermetallic phases in AA5657 alloys. A slice of AA1050 alloy ingot was also studied to better understand the transition of Fe intermetallic phases across the FTZs. Based on the results obtained in this research, it would be useful to investigate the following concepts further:

1. The detailed information of the Ni-containing intermetallic phase appears in the high Ni content ingots and the factors that affect its formation.

2. Evaluate reflectivity of AA5657 alloy products and correlation with the Fe intermetallic phases content.

3. Further the study of the combined effect of V and Ni on Fe intermetallic phases.

APPENDICES

Appendices A: Table of phase crystals input the Database used in EBSD identification [28,32]

Phase	State	Bravais Lattice & Space Group	Lattice Parameter
Al		Cubic Fm -3 m(225)	a = 0.4049nm
Al_mFe	Metastable	Body centered tetragonal	a = 0.884 nm b = 0.2.16 nm
$Al_6Fe(Mn)$	Metastable	C-centered orthorombic Cmcm (63)	a = 0.7437 nm b = 0.6492 nm c = 0.8788 nm
Al_3Fe	Stable	C centered monoclinic C2/m (12)	a = 1.549 nm b = 0.808 nm c = 1.2476 nm β = 107.72°
Al_7Fe_2Si	Stable	Hexagonal $P6_3$/mmc (194)	a = 1.23 nm c = 2.62 nm
Al_4Fe_2Si		Hexagonal $P6_3$/mmc (194)	a = 0.7509 nm c = 0.7594 nm
Al_2FeSi		Cmmm (67)	a = 0.7995 nm b = 1.5162 nm c = 1.5221 nm
$AlFe_2Ti$		Fm -3 m (225)	a = 0.5879 nm
$Al_8FeMg_3Si_6$		Sp -6 2m (189)	a = 0.662 nm c = 0.792 nm γ = 120°
$AlFe_2Ni$		Fm -3 m (225)	a = 0.5758 nm
Al_2FeNi		(221)	a = 0.2883 nm

Appendices A (Continued)

Phase	State	Bravais Lattice & Space Group	Lattice Parameter
$AlFe_2V$		Fm -3 m (225)	a = 0.5761 nm
Al_2Fe		P1 (1)	a = 0.4878 nm b = .6461 nm c = 0.8800 nm α =91.75 β =73.27 γ =96.89
AlFe		Pm -3 m(221)	a = 0.2908 nm
$Al_7Fe_3Ni_{30}$		(221)	a = 0.3596 nm
$AlFe_2$		Fd -3 m(227)	a = 0.7355 nm
$AlFe_3$		Fm -3 m(225)	a = 0.58 nm
$AlFe_4$		(229)	a = 0.2932 nm

Appendices B: Routine for quantitative analysis of Fe intermetallic particles

```
001 Grab
002 Load Image '#' with Bitplanes
      File: #.tif
      Path: C:\Documents and Settings\Duygu Kocaefe\My Documents
\gaofeng\quantification\Dc simulator 5657\570 Ni cold mount\p4
003 Clear => All
004 Color Threshold -> BPL1
      Hue: start = 251? delta = 359?
      Saturation: 0%..99%
      Intensity: 98..196
      Pause On Run
005 Pause Edit Draw BPL1
      complete phases line
006 Pause Edit Lasso BPL1
      complete phases lasso
007
008 ' choose AlmFe
009 Hide => All
010 Pause Edit Lasso BPL2
      Choose AlmFe
011 (BPL1 AND BPL2) -> BPL2
012 (BPL1 DIFF BPL2) -> BPL1
013
014 ' choose Al6Fe
015 Hide => All
016 Show => BPL2
017 Pause Edit Lasso BPL3
      Choose Al6Fe
018 (BPL1 AND BPL3) -> BPL3
019 (BPL1 DIFF BPL3) -> BPL1
020
021 ' choose Al3Fe
022 Hide => All
023 Show => BPL2, BPL3
024 Pause Edit Lasso BPL4
      Choose Al3Fe
025 (BPL1 AND BPL4) -> BPL4
026 (BPL1 DIFF BPL4) -> BPL1
027
028 ' choose Al8Fe2Si
029 Hide => All
030 Show => BPL2, BPL3, BPL4
031 Pause Edit Lasso BPL5
```

```
     Choose Al7Fe2Si
032 (BPL1 AND BPL5) -> BPL5
033 (BPL1 DIFF BPL5) -> BPL1
034
035 ' choose AlFeNi
036 Hide => All
037 Show => BPL2, BPL3, BPL4, BPL5
038 Pause Edit Lasso BPL6
     Choose AlFeNi
039 (BPL1 AND BPL6) -> BPL6
040 (BPL1 DIFF BPL6) -> BPL1
041 Field Measures (BPL2)    -> FLDM1
     Perimeter
     Area Percent
     Count
     Density
042 Field Measures (BPL3)    -> FLDM2
     Perimeter
     Area Percent
     Count
     Density
043 Field Measures (BPL4)    -> FLDM3
     Perimeter
     Area Percent
     Count
     Density
044 Field Measures (BPL5)    -> FLDM4
     Perimeter
     Area Percent
     Count
     Density
045 Field Measures (BPL6)    -> FLDM5
     Perimeter
     Area Percent
     Count
     Density
046
047 Square Grid 1x1 -> BPL12
     Overall Grid Dimensions
     760 x 572 pixels
     1986 x 1497
048 Transfer (BPL2 SEL BPL12) -> None
049 Transfer (BPL3 SEL BPL12) -> None
050 Transfer (BPL4 SEL BPL12) -> None
```

051 Transfer (BPL5 SEL BPL12) -> None
052 Transfer (BPL6 SEL BPL12) -> None
053 Object Measures (BPL2, 3, 4, 5, 6) -> OBJM6
    Area
    Perimeter
    Length
    Feret Average
    Aspect Ratio
End of fields

References

---

1. “Metals Handbook”, 10th ed., Vol. 2, ASM, 1990, p. 62.

2. E.F. Emley, Int. Met. Rev., June 1976, 206, p.75.

3 ASM Handbook Volume 9: Metallography and Microstructures(2004).

4 . X.-G. Chen, “Growth Mechanisms Of Intermetallic Phases In DC Cast AA1XXX Alloys”, Light Metals, 1998, 1071-1076.

5. Celil A. Aliravci, John E. Gruzleski and M. ö. Pekgülleryüz, “Calculation of Phase Diagrams and Verification of the Eutectic Temperature for the Solidfication of Metastable Al-Fe Phases in DC-cast Aluminium Alloys”, In: Proceedings of the 4th Decennial international conferrnce on solidification processing, Sheffield, July 1997.

6 . P. Skjerpe, “Solidification structure and primary Al-Fe-Si particles on direct-chilled-cast aluminium alloys”, Ultramicroscopic 22 (1987) 239-250.

7 . Katgerman et al, “Modeling of DC Casting of Aluminium Alloys,” in production, Refining , Fabrication and recycling of Light metals, Proc. 29th Annual Conf. of Metallurgists of CIM, Hamilton, Ont., Pergamon, pp 96-110(26-30 Aug., 1990).

8 Westengen, H., ”strusture inhomogeneities in direct chill cast sheet ingots of commerical purity aluminium”, Aluminium, Jahrg (1982-7), 398-401.

9 Emley, E.F., “Continuous Casting, ” Int.Met.Rev., #206, pp 75-115 (June 1976).

10 Ceil A. Aliravic et all, “A thermodynamic study of metastable Al-Fe phase formation in direct chill (DC)-cast aluminium alloy ingots”, Light Metals (1998), 1381-1389.

11 Trond Furu and Hans Erik Vatne, “Effect of as-cast microstructure and subsequent

processing on banding in rolled Al-sheets", Light Metals, (1999), 749-754.

12 X.-G. Chen, "Effect of grain refiners on intermetallic phases in AA1XXX simulated DC casting", Light Metals, 1999, 803-809.

13 S.J. Maggs et al, "The effect of trace elements on intermetallic phase selection in simulated DC castings", Light Metals, 1995, 1039-1047.

14 M. W. Meredith et al, "The effect of grain refining additions on intermetallic selection in dilute aluminium alloys", Light Metals, 1998, 977-982.

15 John Granfied et Johun A. Taylor, "The impact of raising Ni and V impurity levels in smelter grade aluminium and potential control strategies", Aluminium Cast House Technology, 2009, 129-136.

16 S. Brusethaug, D. Porter and O. Vorren, "The effect of Process Parameters on the fir-tree strucrure in DC-cast rolling ingots", proceedings of the 8th International Leichtmetalltagung, Leoben-Wien, (1987), 472-476.

17 Belov, N.A. et all, Iron in Aluminium Alloys: Impurity and Alloying Element 2002: Tayor and Francis.

18 Westengen, H., "strusture inhomogeneities in direct chill cast sheet ingots of commerical purity aluminium", Aluminium, Jahrg (1982-7), 398-401.

19 Langsrud, Y., "The use of phase diagrams for calculating Solidification Paths," in user aspects of phase diagrams, ed. Hayes, F.H., the institute of metals, London, pp. 99-100 (1991).

20 Rhines, F.N., Phase diagrams in metallurgy: Their development and application, McGraw-Hill Book, Co., N.Y. (1956).

21 Mondolfo, L.F., Aluminium Alloys: Structure and Properties, Buttterworths (1976)

22 Dix EH, Heath AC. Trans AIME 1928; 76:164.

23 Philips HWL, Varley PC. J Inst Met 1943; 69:317.

24 Griger, A., stefaniay, V., Lendvai, A., and Turmezey, T., "Possible modification of cast Structure by continues casting technology in AlFeSi alloys – parts III: Intermetallic phases," Aluminium, vol. 65, no. 10, pp. 1049-1056 (1989).

25 Y. J. Li and L. Arnberg, "Solidification structures and phase selection of iron-bearing eutectic particles in a DC-cast AA5182 alloy", Acta Materialia, Volume 52, Issue 9, 17 May 2004, Pages 2673-2681

26 M. V. Kral, H. R. McIntyre and M. J. Smillie, "Identification of intermetallic phases in a eutectic Al–Si casting alloy using electron backscatter diffraction pattern analysis", Scripta Materialia, Volume 51, Issue 3, August 2004, P215-219.

27 Langsrud, Y., "silicon in commercial Aluminium Alloys – what becomes of it during DC-Casting?" in Effect of Iron and Silicon in Aluminium and its Alloys, Key Eng. Mat., vols. 44 & 45, pp 95-116 (1990)

28 Villars, P. and Calvert, L.D., Pearson's Handbook of Crystallographic Data for Intermetallic phases, ASM, Metals Park Ohio (1991)

29 Skjerpe. P, "AN ELECTRON-MICROSCOPY STUDY OF THE PHASE AL3FE" BLACKWELL SCIENCE LTD 1987 JOURNAL OF MICROSCOPY-OXFORD 148: 33-50.

30 P. Skjerpe, "Intermetallic Phases Formed during DC-Casting of an Al-0.25 Wt Pct

---

Fe-0.13 Wt Pct Si Alloy", Met. Trans. A,18A (1987), 189-200.

31 Turmezey, T et al, "AlFeSi phases in Aluminium," in Effect of Iron and Silicon in Aluminium and its Alloys, Key Eng. Mat., vols. 44 & 45, pp 57-68 (1990)

32 P. Skjerpe, "Structure of AlmFe", Acta Cryst., vol. B44, pp 480-486 (1988).

33 H. Wenstengen, "Formation of Intermetallic Compounds During DC Casting of a Commerical Al-Fe-Si alloy", Z. Metallkde. 73 (1982), 360-368.

34 P. Skjerpe, "Intermetallic Phases Formed during DC-Casting of an AI-0.25 Wt Pct Fe-0.13 Wt Pct Si Alloy", Met. Trans. A,18A (1987), 189-200.

35 Turmezey T, Stefaniay V, Griger A, In: internation workshop on the effect of iron and silicon aluminium and its alloy, May 1989 Balatonfured, Hungary, 57. Zurich, Switzerland: Trans Tech Publ.; 1990.

36 T. Turmezey et al., "Effect of Iron and Silicon in Aluminium and its Alloys", Key Engineering Materials, 44-45, 57 (1991)

37 B. Dutta, M. Rettenmayr, "Effect of cooling rate on the solidification behaviour of Al–Fe–Si alloys," Materials Science and Engineering A, Volume 283, Issues 1-2, 15 May 2000, Pages 218-224.

38 D. Panahi et all, "Influence of cooling rate and composition on formation of intermetallic phases in solidifying Al–Fe–Si melts," Canadian Metallurgical Quarterly Volume 50, Issue 2, April 2011, Pages 173-180.

39 P. Skjerpe, "Intermetallic Phases Formed during DC-Casting of an AI-0.25 Wt Pct Fe-0.13 Wt Pct Si Alloy", Met. Trans. A,18A (1987), 189-200.

40 S. Asami T. Tanaka, and A. Hideno, "Fir-Tree Structure in DC Cast fagots of Al-

Mg-Fe-Si Alloy", Journal of Japan Institute of Light Metals, 1978, vol. 28, pp. 321-27.

41 H. Kosuge and I. Mizukami, "Behavior of Fir-Tree Structure in Al-Fe-Si Alloy Ingots Soaking at Elevated Temperatures", Journal of Japan Institute of Light Metals, 1972, vol. 22, pp. 437-44.

42 R. M. Young and T. Clyne, "An Al-Fe Intermetallic Phase Formed During Controlled Solidification", Scripta Metailurgica, 1981, vol. 15,.pp. 1211-16

43 I. Miki, H. Kosuge, and K. Nagahama, "Supersaturation and Decomposition of Al-Fe Alloys During Solidification", Journal of Japan Institute of Light Metals, 1975, vol. 25, pp. 1-9.

44 L.Backreud, “Kinetic aspects of the solidification of binary and tenary alloy systems,” Jernkontorets Annaler, vol. 152, pp. 109-138 (1968).

45 Langsrud, Y., “silicon in commercial Aluminium Alloys – what becomes of it during DC-Casting?” in Effect of Iron and Silicon in Aluminium and its Alloys, Key Eng. Mat., vols. 44 & 45, pp 95-116 (1990)

46 B. Cantor, K. O’Reilly, “Solidification and Casting”, Mater. Sci. and Eng: (UK, IOP Publishing Ltd, 2003), P 7-9.

47 D.A. Granger: Microstructure control in ingots of aluminum alloys with an emphasis on grain refienment, in Light Metals, edited by B.J. Welch (TMS, Warrendale, PA, 1998), pp. 941–952.

48 CM. Allen, K.A.Q. O'Reilly, P.V. Evans, and B. Cantor, "The Effect of Vanadium and Grain Refiner Additions on the Nucleation of Secondary Phases in 1XXX Al

Alloys", Acta Materialia, 1999, vol. 47, pp. 4387-403.

49 Klimek. L, "Phases identification by means of EBSD method – New possibilities of materials researches", Archives of metallurgy and materials Vol. 53(2008), num. 1, pg:151-155.

50 S. Kikuchi (1928). "Diffraction of Cathode Rays by Mica". Japanese Journal of Physics 5: 83–96

51 M. V. Kral, H. R. McIntyre and M. J. Smillie, "Identification of intermetallic phases in a eutectic Al–Si casting alloy using electron backscatter diffraction pattern analysis", Scripta Materialia, Volume 51, Issue 3, August 2004, P215-219

52 C. MAURICE & R. FORTUNIER, "A 3D Hough transform for indexing EBSD and Kossel patterns", Journal of Microscopy, Vol. 230, Pt 3 2008, pp. 520–529.

53 Kral, M.V. , McIntyre, H.R., Smillie, M.J., "Identification of intermetallic phases in a eutectic Al-Si casting alloy using electron backscatter diffraction pattern analysis", Scripta Materialia Volume 51, Issue 3, August 2004, Pages 215-219 .

54 Kral, M.V, "A crystallographic identification of intermetallic phases in Al-Si alloys", Materials Letters Volume 59, Issue 18, August 2005, Pages 2271-2276 .

55 Y.J. Li, L. Arnberg, "Solidification structures and phase selection of iron-bearing eutectic particles in a DC-cast AA5182 alloy", Acta Materialia Volume 52, Issue 9, 17 May 2004, Pages 2673-2681.

56 Y.J. Li, L. Arnberg,"A eutectoid phase transformation for the primary intermetallic particle from Alm(Fe,Mn) to Al3(Fe,Mn) in AA5182 alloy", Acta Materialia Volume 52, Issue 10, 7 June 2004, Pages 2945-2952 .

---

57 C. B. Walker and M. Marezio, Acta Met., 1959, 7, 769.

58 Gokhale AM (1990) in: Voort G (ed) ASM handbook, vol. 9, the materials information society OH, p 431.

59 C.M. Allen, K.A.Q'Reilly, B. Cantor, P.V. Evans, “Intermetallic phase selection in 1xxx Al-alloys”, Progress in Materials Science 43 (1998), 89-170.

60 Mondolfo, L.F., Aluminium Alloys: Structure and Properties, Buttterworths (1976).

61 Black, P.J., “The structure of Al3Fe - Ⅰ ,” Acta Cryst., Vol. 8, pp.43-48 (1955).

62 John Granfied et Johun A. Taylor, “The impact of raising Ni and V impurity levels in smelter grade aluminium and potential control strategies”, Aluminium Cast House Technology, 2009, 129-136.

63 Mannweiler, U., et al., High vanadium Venezuelan petroleum coke, a raw material for the aluminium industry?, Light Metals: Proceedings of Sessions, AIME Annual Meeting (Warrendale, Pennsylvania), 1989, Metallurgical Soc of AIME, 449-454

64 Vogt, F., et al., A preview of anode coke quality in 2007, TMS Light Metals, 2004, 489-493. CM. Allen, K.A.Q. O'Reilly, P.V. Evans, and B. Cantor, "The Effect of Vanadium and Grain Refiner Additions on the Nucleation of Secondary Phases in 1XXX Al Alloys", Acta Materialia, 1999, vol. 47, pp. 4387-403.

65 CM. Allen, K.A.Q. O'Reilly, P.V. Evans, and B. Cantor, "The Effect of Vanadium and Grain Refiner Additions on the Nucleation of Secondary Phases in 1XXX Al Alloys", Acta Materialia, 1999, vol. 47, pp. 4387-403.

66 Dong, Liang and Howard, Jones, “Effect of growth velocity on growth

temperature of the Al-Al3Fe and Al-Al6Fe eutectics", Z. Metallkd. Volume 83, Issue 4, April 1992, Pages 224-226.